Phenomenology of Topological Solitons

by

Ayush Saurabh

A Dissertation Presented in Partial Fulfillment
of the Requirements for the Degree
Doctor of Philosophy

Approved April 2020 by the
Graduate Supervisory Committee:

Tanmay Vachaspati, Chair
Richard F Lebed
Cynthia Keeler
Matthew Baumgart

ARIZONA STATE UNIVERSITY

May 2020

ABSTRACT

In this dissertation, I present the results from my recent investigations into the interactions involving topological defects, such as magnetic monopoles and strings, that may have been produced in the early universe. I performed numerical studies on the interactions of twisted monopole-antimonopole pairs in the 't Hooft-Polyakov model for a range of values of the scalar to vector mass ratio. Sphaleron solution predicted by Taubes was recovered, and I mapped out its energy and size as functions of parameters. I also looked into the production, and decay modes of $U(1)$ gauge and global strings. I demonstrated that strings can be produced upon evolution of gauge wavepackets defined within a certain region of parameter space. The numerical exploration of the decay modes of cosmic string loops led to the conclusions that string loops emit particle radiation primarily due to kink collisions, and that their decay time due to these losses is proportional to L^p, where L is the loop length and $p \approx 2$. In contrast, the decay time due to gravitational radiation scales in proportion to L, and I concluded that particle emission is the primary energy loss mechanism for loops smaller than a critical length scale, while gravitational losses dominate for larger loops. In addition, I analyzed the decay of cosmic global string loops due to radiation of Goldstone bosons and massive scalar (χ) particles. The length of loops I studied ranges from 200-1000 times the width of the string core. I found that the lifetime of a loop is approximately $1.4L$. The energy spectrum of Goldstone boson radiation has a k^{-1} fall off, where k is the wavenumber, and a sharp peak at $k \approx m_\chi/2$, where m_χ is the mass of χ. The latter is a new feature and implies a peak at high energies (MeV-GeV) in the cosmological distribution of QCD axions.

DEDICATION

To every family member I gained since my birth.

ACKNOWLEDGMENTS

First, I would like to thank an amazing teacher and fun collaborator I gained during my PhD, my advisor Professor Tanmay Vachaspati. His constant enthusiasm for physics has been very inspiring and a learning experience. I would also like to thank Professor Matthew Baumgart, with whom I gained insight into various aspects of quantum field theory. I am indebted to Professor Levon Pogosian for our collaboration that led to two very interesting papers. I am very thankful for my classmates Lucas, David, and Jiawei, with whom I had lunch discussions almost every day during my five years at ASU. Our office couldn't have been more comical and productive without the presence of Logan (and Sophia), Nikhil (and Anusha), Jesse, Charlie, Tucker, Panos, Mainak, Brandon, Andy, George, Victoria, Hank, Jeff, Zidu, Jayden, Francis, Ozan, and Carlos. My PhD experience would be incomplete without the curiosity of cats Ghost, Eli, and Neutrino. I am very grateful for my friends Kristin (and her sons Jayden & Brendan) and Nimesh for their constant support. Finally, I would like to thank my committee members, Professors Richard Lebed, Cynthia Keeler, and Matthew Baumgart for their useful comments and suggestions in preparing this thesis.

TABLE OF CONTENTS

CHAPTER Page

LIST OF TABLES

LIST OF FIGURES

Figure Page

Figure Page

Figure Page

Figure Page

Chapter 1

INTRODUCTION

Our universe is widely believed to have gone through multiple phase transition events right at its onset. As the universe expanded from the initial singularity, temperature went down through multiple critical values corresponding to each phase transition. From the point of view of symmetries governing the physics, this whole process can be schematically shown as

$$G \to H \to ... \to SU(3) \times SU(2) \times U(1) \to SU(3) \times U(1)\,,$$

where the symmetry of a grand unified theory G is broken to smaller symmetry groups, eventually settling into the Standard Model of the particle physics that governs most of the interactions that we detect today. The production of topological defects in the universe is intimately linked to these symmetry breaking phenomena. Whenever the temperature falls below the critical value very quickly, equilibrium is only achieved in a small volume initially and therefore it is reasonable to expect that the symmetry will break along different directions in each of these volumes before the whole system equilibrates. This can lead to a network of defects like vortices (strings), magnetic monopoles, domain walls, and textures being formed.

A breakthrough step was the realization by Kibble (1976) that all of these defects can be understood as the result of vacuum manifolds having non-trivial topologies, and that their production in a cosmological context is inevitable. In his paper, he considered a gauge theory with an N-component real scalar field ϕ transforming under the symmetry group $O(N)$ represented by the Lagrangian

$$\mathcal{L} = \frac{1}{2}(D^\mu\phi)^a(D_\mu\phi)^a - \frac{1}{4}W^{a\mu\nu}W^a_{\mu\nu} - \frac{\lambda}{4}(\phi^a\phi^a - \eta^2)^2\,, \tag{1.1}$$

where $a = 1, \ldots, N$, the covariant derivative is defined as

$$(D_\mu \phi)^a = \partial_\mu \phi^a + e\epsilon^{abc} W_\mu^b \phi^c \,, \tag{1.2}$$

and the gauge field strength is given as

$$W_{\mu\nu}^a = \partial_\mu W_\nu^a - \partial_\nu W_\mu^a + e\epsilon^{abc} W_\mu^b W_\nu^c \,. \tag{1.3}$$

As the temperature falls to zero, symmetry $O(N)$ breaks down to $O(N-1)$ and the scalar field settles into one of the states in the vacuum manifold S^{N-1}, that is,

$$\langle \phi \rangle^2 = \eta^2 \,. \tag{1.4}$$

At finite temperatures, the expectation value of the scalar field in thermal equilibrium would depend on the available vacuum states of the temperature dependent potential. Perturbative computations show that this potential would have the following temperature dependence,

$$V(\phi, T) = \frac{\lambda}{4}(\phi^a \phi^a - \eta^2)^2 + \frac{1}{48}\left[2\lambda(N+2) + 6e^2(N-1)\right] T^2 \phi \,. \tag{1.5}$$

This potential is minimized at the symmetry breaking critical temperature

$$T_c = \eta \left(\frac{N+2}{12} + \frac{N-1}{4} \frac{e^2}{\lambda} \right) \,, \tag{1.6}$$

above which $\langle \phi \rangle = 0$. The vacuum expectation value for the scalar field at this critical temperature is given as

$$\langle \phi \rangle^2 = \eta^2 \left[1 - \left(\frac{T}{T_c} \right)^2 \right] \,, \tag{1.7}$$

which plays the role of order parameter in the study of phase transitions.

Kibble considered the scenario in which the universe expands and cools down below the critical temperature T_c. Fluctuations in the scalar field lose energy and the field settles into one of the randomly chosen vacuum states in different regions

of space. There will obviously be chaotic fluctuations in $\langle\phi\rangle$ but only low frequency modes survive as they are energetically preferred and therefore determine the size of domains with the same expectation value throughout.

To find the size of these domains, he noted that below the critical temperature the free energy increases by

$$\Delta f = \frac{\lambda}{4} \langle\phi\rangle^4 \,, \tag{1.8}$$

reaching its peak value of $(\lambda/4)\eta^4$ at zero temperature. Since the scalar and vector excitations acquire mass upon symmetry breaking, these masses will set the scale of fluctuations. The fields are correlated up to these scales. Correlation length for the scalar field is given as

$$\xi_S = \frac{1}{m_S} = \frac{1}{\sqrt{2\lambda}\,\langle\phi\rangle} \,, \tag{1.9}$$

and for the vector field as

$$\xi_V = \frac{1}{m_V} = \frac{1}{e\,\langle\phi\rangle} \,. \tag{1.10}$$

Since the expectation value of the scalar field is zero at the critical temperature T_c, these correlation lengths diverge.

Going below the critical temperature, if the fluctuations corresponding to the scale ξ have higher free energy than the temperature T, the field will have high probability of reverting back to the unbroken symmetry phase. The free energy for the length scale ξ can be calculated from Eqs. (1.8) & (1.9) giving us

$$\Delta f \approx \frac{|\langle\phi\rangle|}{8\xi^3\sqrt{2\lambda}} \,. \tag{1.11}$$

This free energy becomes less than the temperature when

$$\frac{1}{T^2} = \frac{1}{T_c^2} + \frac{2\lambda}{\eta^2} \,. \tag{1.12}$$

The correlation length at this point is $\xi = (2\lambda T)^{-1}$. As the temperature goes down further, the scalar field loses any ability to interact with itself beyond this special

length scale. This sets the maximum distance over which the scalar field can have non-zero correlations defining the size of the domain. Also, the gradient term in the Lagrangian smoothens out any remaining fluctuations within the domain resulting in a uniform $\langle\phi\rangle$ over the domain. Kibble further discussed the topology of these domains in various theories providing estimates for defects like strings and domain walls. These seminal results are a direct consequence of limits set by causality.

Kibble's computation of domain size, however, turned out to be slightly incorrect as he only considered equilibrium configurations. Zurek (1985, 1996) extended the computations above to include non-equilibrium effects. He used results for vortices in superfluids to obtain insights into the formation of strings in cosmological models. In superfluids (Helium-4), the wavefunction ψ of the Bose-Einstein condensate is used as the order parameter to describe the phase transitions. Vortices may form if the phase of the wavefunction takes random values in different regions of sizes determined by the some correlation scale d.

The superfluid phase is achieved through a process of rapid pressure quench. Close to the critical temperature T_c, the potential takes the Landau-Ginzburg form at leading order in $(T - T_c)$ and is as follows,

$$V(\psi) = \alpha|\psi|^2 + \frac{1}{2}\beta|\psi|^4\,, \tag{1.13}$$

where $\alpha = \alpha'(T - T_c)$, and α' and β are constants.

The wavefunction for the Bose-Einstein condensate ψ satisfies the Gross-Pitaevskii (non-linear Schrödinger) equation, which gives us the equilibrium correlation length,

$$\xi = \frac{\hbar}{\sqrt{2m\alpha}}\,, \tag{1.14}$$

where m is the mass of Helium-4 atom. Equilibrium correlation times can also be estimated from the same equation as

$$\tau = \frac{\hbar}{\alpha}\,, \tag{1.15}$$

If the quench is performed instantaneously, the wavefunction does not get any time to increase the correlation length and therefore the domain size is given by the equilibrium correlation length before the phase transition occurred, that is, $d = \xi_i$. When the quench is performed very slowly, the correlation length increases to infinity near the critical temperature T_c. For quenching done at a finite speed, Zurek showed that the maximum correlation distance is reached at the freeze-out time $\tau_F = \sqrt{\tau_0 \tau_Q}$ and it is equal to

$$d(\tau_F) = \xi_0 \left(\frac{\tau_Q}{\tau_0} \right)^{\frac{\nu}{2}} , \tag{1.16}$$

where ξ_0 is the equilibrium correlation length at zero temperature, τ_0 is a characteristic time scale at zero temperature, τ_Q is the quench time which tells us the rate at which temperature is lowered, and $\nu = 1/2$ in Landau-Ginzburg theory while in renormalization group models $\nu = 2/3$. Basically, as the phase transition proceeds, correlation length of the order parameter tries to approach its equilibrium value of infinity at the critical temperature but falls short because of the limited time provided by the quenching process.

The Kibble-Zurek mechanism as described above works well for understanding production of topological defects in models where a global symmetry is broken. However, when a local symmetry is broken, the order parameter is not gauge invariant and so Zurek's arguments do not describe the complete picture. Indeed, Hindmarsh and Rajantie (2000a) showed that, in the Abelian Higgs model, symmetry breaking leads to thermal fluctuations of the magnetic flux getting frozen as the field configuration does not get enough time to adjust itself to minimize the magnetic flux. This process leads to formation of vortices in addition to the vortices formed by the Kibble-Zurek mechanism.

The importance of the topological defects lies in various tests that they provide for testing models of grand unification. These models predict many different types of

topological defects produced over a large range of energy scales. Observations of such defects would therefore help us constrain or rule out a lot of these models. Since the discovery of the first defect solutions in the simplest renormalizable gauges theories, that is vortices by Nielsen and Olesen (1973), and magnetic monopoles by 't Hooft (1974) and Polyakov (1974), enormous progress has been made in the understanding of the interactions involving such objects.

Strings exist in various field theories that describe particles as well as condensed matter systems like superfluids and superconductors (Tinkham (2004)). Cosmic strings play an important role in building theories of the early universe (Vilenkin and Shellard (2000)) and provide a rare observational probe of String Theory (Copeland *et al.* (2011)). Cosmic strings were actually being considered as the origin of structures in the universe (Vilenkin and Everett (1982); Zeldovich (1980)). However, recent studies based on cosmic microwave background data have shown that topological defects did not seed the formation of structures in the universe (Bevis *et al.* (2007)). Cosmic strings could still produce other observable signatures in the form of particle and gravitational radiation.

For strings produced at grand unification energy scales of around 10^{16} GeV, the linear mass density would be extremely high ($\sim 10^{22}$ g cm^{-1}), which shows their significant power to influence phenomena at cosmological scales. It is expected that the decay of these cosmic strings would create observable signals in the form of cosmic microwave background (CMB) fluctuations, gravitational waves, cosmic and gamma rays. Current CMB data limits the cosmic string contribution to 1% of the temperature power spectrum. Many theoretical studies have been performed by now that compute the contribution of cosmic strings to CMB in the simplest Abelian gauge theory (Hindmarsh *et al.* (2019); Lopez-Eiguren *et al.* (2017); Lizarraga *et al.* (2016); Hindmarsh *et al.* (2009a)).

The search for observable signatures of cosmic strings has mostly focused on their gravitational effects, and they are among the main science goals of LIGO (Abbott *et al.* (2018)). In a cosmic string network, gravitational radiation would be emitted by cusps and also in the form of stochastic background emanating from the string network. The tightest bound on the string tension μ, coming from millisecond pulsar timing measurements (Lasky *et al.* (2016)), is based on the gravitational wave (GW) background produced by decaying cosmic string loops. This bound, $G\mu \lesssim 10^{-10}$ (Blanco-Pillado *et al.* (2018a); Abbott *et al.* (2018)), where G is Newton's gravitational constant, assumes that string loops decay primarily into GW with the quantitative predictions obtained from simulations using the Nambu-Goto (NG) approximation that ignores the field composition of the strings (Albrecht and Turok (1985); Bennett and Bouchet (1990); Allen and Shellard (1990a); Blanco-Pillado *et al.* (2011); Lorenz *et al.* (2010)). While it is widely accepted that the Nambu-Goto description works well for loops much larger than the string width, the exact loop size above which the particle composition of the string cores can be ignored is not firmly established. The few existing field theory simulations of string networks suggest that loops primarily decay into particle radiation (Hindmarsh *et al.* (2017)), with cosmological size loops not surviving beyond one oscillation, potentially leading to a new paradigm for cosmic string evolution in which the GW bounds do not apply. Thus it is critical to examine particle emission by cosmic string loops and to determine their primary decay mode.

If high energy particle physics contains a global $U(1)$ symmetry that spontaneously breaks at lower energies, the universe would be left with a network of global strings (Davis (1985, 1986); Vilenkin and Shellard (2000)). Loops of such cosmic global strings would oscillate and decay by the emission of massless and massive radiation that could form part of the dark matter density today (Vilenkin and Vachaspati

(1987)). This scenario is relevant to models in which axions are proposed as a means to solve the strong CP problem and is frequently studied in this context (Vilenkin and Vachaspati (1987); Davis (1986); Harari and Sikivie (1987); Davis and Shellard (1989); Hagmann and Sikivie (1991); Battye and Shellard (1994b,a); Yamaguchi *et al.* (1999); Hagmann *et al.* (2001); Hiramatsu *et al.* (2011); Klaer and Moore (2017, 2019); Gorghetto *et al.* (2018)). Axions are basically pseudoscalar Goldstone bosons resulting from spontaneously broken global chiral symmetries and are parameterized by two constants, mass m_a and decay constant f_a. In case of QCD, the Lagrangian has a total derivative (topological) term as follows,

$$\mathcal{L}_{QCD} = \ldots + \frac{\theta_{QCD}}{32\pi^2} tr(G_{\mu\nu}\tilde{G}^{\mu\nu})\,. \tag{1.17}$$

A non-zero value of θ_{QCD} violates the CP symmetry. To resolve this issue, Peccei-Quinn introduced a global $U(1)$ field ϕ such that $\theta_{QCD} = \mathcal{C}\phi/f_a$, where $\mathcal{C}$ is the fine structure constant. The field ϕ helps dynamically set $\theta_{QCD} = 0$ through non-perturbative instanton effects.

Other than understanding the principal decay modes of the cosmic strings, it is also of interest to study the processes that could produce strings in a laboratory setting. While the topological defects like strings are classical solutions, particles in the Standard Model are quantum mechanical phenomena. In quantum theory, topological defects can be viewed as a bound state of a large number of quanta. The interpretation of solitons as particles is most explicitly known in the sine-Gordon model. In that case, the operators that create and destroy solitons (which are fermions), can be written in terms of particle quanta that are bosons. The question of interest is if it is possible to assemble particles to make strings? And if so, can we say something about the initial conditions necessary to produce strings?

Now, magnetic monopoles are novel solutions in a large class of non-Abelian gauge

theories ('t Hooft (1974); Polyakov (1974)). Although the predicted monopole density for magnetic monopoles in the universe turned out to be too high to be realistic (Preskill (1979)), they have been studied for their unconventional classical and quantum properties (Manton and Sutcliffe (2004)). Experiments are currently underway to find cosmological monopoles (Abbasi *et al.* (2013); Adrián-Martínez *et al.* (2012)) as well as monopoles in particle accelerators (Acharya et al. (2016)).

In spite of the long history of monopoles, there are certain questions that have not been fully resolved. Key among these is to discover particle physics processes that can create magnetic monopoles (Vachaspati (2016a)). Dynamics that involve both monopoles and antimonopoles have not received much attention (Vachaspati (2016c)). On the other hand, monopole-*monopole* dynamics has been beautifully resolved in the moduli approximation (Manton (1982a); Manton and Sutcliffe (2004)).

An important feature in the monopole-antimonopole system is that the monopole and antimonopole can have a relative twist (see Sec. 3.2). This additional degree of freedom has profound consequences for the interaction energy of a monopole and antimonopole. In particular it enables the existence of an unstable static bound state solution, now known as a "sphaleron", as first argued by Taubes (1982a). The sphaleron was rigorously shown to exist in the special case of vanishing scalar mass by Taubes (1982a,b) and for non-vanishing scalar mass by Groisser (1983). The Morse theory analysis used by Taubes in an $SU(2)$ model was used by Manton for the physically relevant electroweak theory (Manton (1983)). This resulted in the discovery of the "electroweak sphaleron" that interpolates between vacua of different Chern-Simons number and is critical to understanding the violation of baryon number in electroweak theory. Anomalous baryon and lepton currents are associated with tunneling between different vacua, leading to baryon and lepton number violating reactions.

The transition from particles to solitons is difficult to treat because particles are described by quantum field theory whereas solitons are described by classical field theory. However, from a practical standpoint, we often produce high occupation number states of quantum particles that behave quasi-classically. For example, by sending currents into a light bulb we produce light that can be described as classical radiation using Maxwell's equations. Thus it is relevant to consider the production of solitons in the scattering of classical waves or wavepackets.

Some of these questions were addressed in by Vachaspati (2016a) for an SO(3) field theory, where incoming wavepackets led to the production of magnetic monopoles. While the possible production of magnetic monopoles is exciting, it is in the realm of speculative physics because we don't know if Grand Unified Theories are correct. On the other hand, strings are closer to reality since we do have superconductors in which (gauge) strings exist (Tinkham (2004)).

In the following chapters, we go into details of how we have tried to answer these questions. In the following chapter, we review some of the well known defect solutions that are relevant to our analyses. In chapter 3, we take a detailed look at how we computed the interaction potential for an $SU(2)$ monopole-antimonopole pair and other interesting properties like the behavior of magnetic field. In chapter 4, we describe the production of strings upon scattering of gauge wavepackets, which is followed by our investigation of the decay modes of a cosmic string loops in the last two chapters.

Chapter 2

TOPOLOGICAL DEFECTS

2.1 A Simple Example: $\mathbb{Z}_2$ Kink

As mentioned in the previous chapter, topology of the vacuum manifold in a theory decides what type of defect will appear (or not) upon symmetry breaking. To demonstrate this, we look at the simplest example of a defect, that is, a kink in $1+1$ spacetime dimensions. It is a stable static solution in a scalar field theory with Z_2 symmetry, that is, invariance under $\phi \to -\phi$ transformation. The following Lagrangian is used in this theory,

$$\mathcal{L} = \frac{1}{2}(\partial_t \phi)^2 - \frac{1}{2}(\partial_x \phi)^2 - V(\phi)\,, \tag{2.1}$$

where (see Fig. 2.1)

$$V(\phi) = \frac{\lambda}{4}(\phi^2 - \eta^2)^2\,. \tag{2.2}$$

The symmetry is broken when the field settles into one of the two vacua, that is,

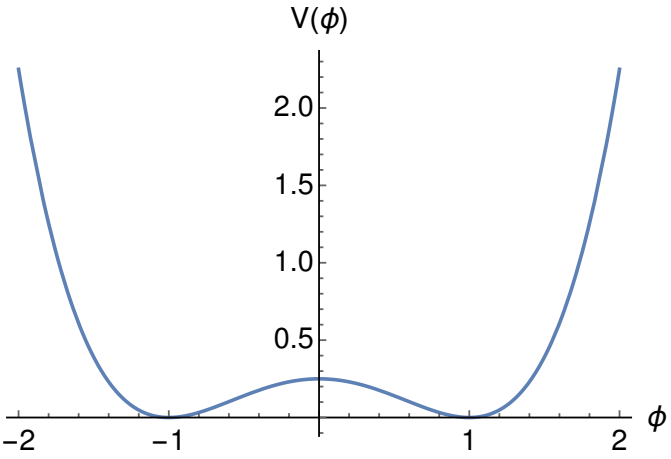

Figure 2.1: $V(\phi)$ with $\lambda = 1$ and $\eta = 1$.

$\phi = \pm\eta$. A Lagrangian for excitations about these vacuum states can be computed by setting $\phi = \eta + \chi$ into the Eq. (2.1). This results in a new Lagrangian as below,

$$\mathcal{L}_\chi = \frac{1}{2}(\partial_t\chi)^2 - \frac{1}{2}(\partial_x\chi)^2 - \frac{\lambda}{4}(\chi^2 + 2\chi\eta)^2\,, \tag{2.3}$$

which is clearly not invariant under the symmetry transformation, $\chi \to -\chi$. It should be noted that the excitation field χ has also acquired mass, $m_\chi = \sqrt{2\lambda}\eta$.

To get a finite energy static kink solution, appropriate boundary conditions must be chosen to minimize the associated energy functional

$$E = \int dx \left[\frac{1}{2}(\partial_x\phi)^2 + \frac{\lambda}{4}(\phi^2 - \eta^2)^2\right]\,. \tag{2.4}$$

This integral would only be finite if $\phi \to \pm\eta$ and $\partial_x\phi \to 0$ as $x \to \pm\infty$. The equations of motion can be solved analytically in this case with the solution (localized at x_0)

$$\phi(x) = \eta \tanh\left(\sqrt{\frac{\lambda}{2}}\eta(x - x_0)\right) = \frac{m_\chi}{\sqrt{2\lambda}} \tanh\left(\frac{m_\chi}{2}(x - x_0)\right)\,.$$

The total energy for this solution can be computed using the Eq. (2.4) and it is as follows,

$$E = \frac{2m_\chi\eta^2}{3} = M_{Kink}\,, \tag{2.5}$$

Note here that the size of the kink, the region containing most of the energy density, is of the order of Compton wavelength of the excitation χ, that is, m_χ^{-1}. Also, size of the kink is bigger than the Compton wavelength of a particle of mass M_{Kink}, which means that the kink behaves essentially like a classical particle.

The stability of this solution can be understood from the observation that, since the space is infinite, an infinite amount of energy will be needed to continuously deform it to a trivial solution like $\phi(x) = \eta$ or $\phi(x) = -\eta$. This would not be possible if the vacuum manifold didn't have disconnected components, where no energy will be required to lift the solution to a trivial one. We can quantify this stability by

defining a conserved topological charge

$$n = \frac{1}{\eta}\int_{-\infty}^{\infty}\frac{\partial\phi}{\partial x}dx = \frac{1}{\eta}\left[\phi(\infty) - \phi(-\infty)\right] . \tag{2.6}$$

For a kink, as described above, $n = 1$. An anti-kink can also be constructed in this theory with $\phi \to \mp\infty$ as $x \to \pm\infty$. This anti-kink has a topological charge, $n = -1$.

To summarize, topologically stable solutions can be constructed in field theories if field at spatial boundaries (infinity) is mapped to points in the degenerate vacuum manifold that is not simply connected. In the case of a kink, moving from $x = -\infty$ to $x = \infty$ leads to the scalar field changing values from $\phi = -\eta$ to $\phi = \eta$, with finite total energy. A string (or vortex) solution exists in theories where the vacuum manifold is a circle S^1_{vac} and the field on a circle at spatial infinity is mapped to this vacuum circle. Monopoles, on the other hand, require vacuum manifolds that have surfaces that cannot be shrunk to a point like a sphere S^2_{vac}. Hybrid defects can also be produced if there are multiple symmetry breaking events involved like in the electroweak theory where monopoles are connected antimonopoles by strings. As we observed before, various conserved topological quantities can be defined for such defects.

In the next few sections, we will discuss strings and monopoles in the simplest gauge theories. All the computations that we present in this report involve these topological defects.

2.2 $U(1)$ Strings

We consider the Abelian Higgs model given by the following Lagrangian with a Mexican hat potential and circular vacuum manifold (not simply connected),

$$\mathcal{L} = -\frac{1}{4}F_{\mu\nu}F^{\mu\nu} + \frac{1}{2}|D_\mu\phi|^2 - \frac{\lambda}{4}\left(|\phi|^2 - \eta^2\right)^2 , \tag{2.7}$$

where $\phi = \phi_1 + i\phi_2$ is a complex scalar field, $D_\mu = \partial_\mu + ieA_\mu$, A_μ is the gauge field with field strength tensor $F_{\mu\nu} = \partial_\mu A_\nu - \partial_\nu A_\mu$, and λ and e are coupling constants. The equations of motion for this model are

$$D_\mu D^\mu \phi = -\lambda(|\phi|^2 - \eta^2)\phi\,, \tag{2.8}$$

$$\partial_\mu F^{\mu\nu} = j^\nu = e\,\mathrm{Im}\left[\phi^*(\partial^\nu + ieA^\nu)\phi\right]\,. \tag{2.9}$$

For a static solution, the energy in the fields is

$$E = \int d^3x \left[\frac{1}{2}|D_i\phi|^2 + \frac{1}{2}(\mathbf{E}^2 + \mathbf{B}^2) + \frac{\lambda}{4}\left(|\phi|^2 - \eta^2\right)^2\right]\,, \tag{2.10}$$

where $E_i = F_{0i}$ is the electric field and $B_i = -\epsilon_{ijk}F_{jk}/2$ is the magnetic field. For a finite energy solution, the individual terms in the integral must vanish at spatial infinity, that is,

$$|\phi| \to \eta,\ |D_i\phi| \to 0, \mathbf{E} \to 0, \mathbf{B} \to 0\,. \tag{2.11}$$

Vanishing covariant derivative leads to the following form for the gauge field in planes orthogonal to the string,

$$A_\theta = \frac{1}{er}\frac{d\alpha}{d\theta} + \dots\,, \tag{2.12}$$

where α is the phase of the field ϕ. Topological string solutions satisfying these asymptotic conditions are well known in the Abelian Higgs model. The solution for a straight string along the $z-$axis is

$$\phi = \eta f(r)e^{i\theta},\quad A_i = v(r)\epsilon_{ij}\frac{x^j}{r^2}\quad (i,j=1,2)\,, \tag{2.13}$$

where we work in cylindrical coordinates $r = \sqrt{x^2+y^2}$, $\theta = \tan^{-1}(y/x)$, and $f(r)$ and $v(r)$ are profile functions that vanish at the origin and go to 1 asymptotically.

The energy per unit length (also the tension) of the string takes the form

$$\mu = \pi\eta^2 F(\beta)\,, \tag{2.14}$$

where $\beta \equiv 2\lambda/e^2 = m_S^2/m_V^2$. The function $F(\beta)$ is known numerically and is a smooth, slowly varying function. We also have $F(1) = 1$ in the so-called Bogomolny-Prasad-Sommerfield (BPS) limit when the scalar mass in the model, $m_S = \sqrt{2\lambda}\eta$ equals the vector mass, $m_V = e\eta$. For β not too large, the thickness of the string is determined by the symmetry breaking scale which is $\sim m_S^{-1}$ for scalar fields and $\sim m_V^{-1}$ for the vector fields. Physically, this can be interpreted as excitations of wavelengths greater than that of Compton wavelengths for the scalar and vector particles staying bound to the string core. This can be seen more rigorously by studying the behavior of the fields far away from the string. Let's define two functions $g(r) = 1 - f(r)$ and $w(r) = 1 - v(r)$, such that $g(r) \to 0$ and $w(r) \to 0$ as $r \to \infty$. By plugging these functions into the equations of motion, we get two ordinary differential equations

$$\frac{1}{r}\frac{d}{dr}\left(r\frac{dg}{dr}\right) - m_S^2 g = 0\,, \tag{2.15}$$

and

$$r\frac{d}{dr}\left(\frac{1}{r}\frac{dw}{dr}\right) - m_V^2 w = 0\,. \tag{2.16}$$

The solutions to these equations take the following form,

$$\begin{aligned} g(r) &\propto \frac{e^{-m_S r}}{\sqrt{r}}\,, \\ w(r) &\propto \sqrt{r}e^{-m_V r}\,. \end{aligned} \tag{2.17}$$

The exponential decay of the fields here demonstrates that the thickness of the string is controlled by the two mass scales, m_S and m_V.

The string is characterized by a topological winding number that is defined as follows,

$$n = \frac{-i}{2\pi\eta^2}\oint dx^i \phi^* \partial_i \phi = \frac{1}{2\pi}\oint \frac{d\alpha}{dl} dl\,. \tag{2.18}$$

Far away from the string, we can use the asymptotic form of the gauge field to get

$$n = \frac{e}{2\pi} \oint \mathbf{A}.\mathbf{dl} = \frac{e}{2\pi} \oint \mathbf{B}.\mathbf{dS} = \frac{e\Phi_{\mathbf{B}}}{2\pi}\,, \tag{2.19}$$

where α is the phase of the scalar field at a given point on the contour and l denotes the parameter along the integration curve. As can be seen in the Fig. 2.2, the phase of the complex field rotates by 2π as we go around a contour enclosing a surface, requiring that a string must pass through it.

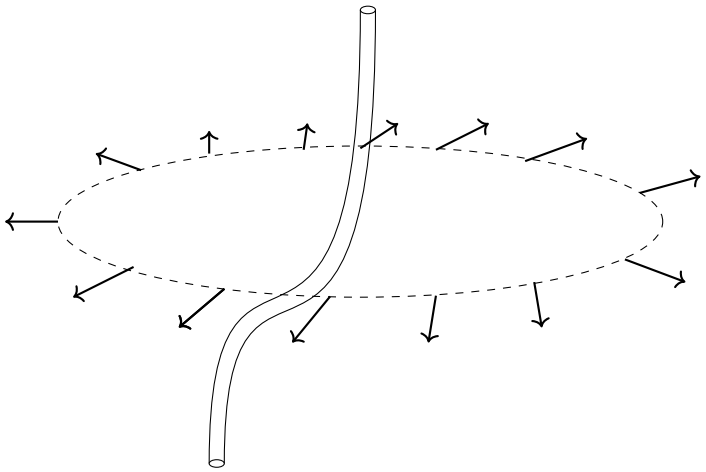

Figure 2.2: A string in the Abelian Higgs theory. Winding on a contour enclosing the string must be nonzero. The arrows on the contour represent the phase of the complex scalar field. As we go along the contour, the complex scalar field rotates by 2π, an essential requirement for the string to exist.

This winding number n can only take integer values and must be conserved overall, which means magnetic flux is quantized as $\Phi_{\mathbf{B}} = 2\pi n/e$.

At the critical value of the coupling $\beta = 1$, as demonstrated by Bogomolny (1976), the second order field equations simplify to a first order system of differential equations. To see this, we consider vortex solutions in a plane. Using integration by parts, the static energy can be shown to be

$$E = \int d^2x \left\{ \frac{1}{2} |[(\partial_x + ieA_x) \pm i(\partial_y + ieA_y)]|^2 + \frac{1}{2}[B_z \pm (\phi\phi^* - \eta^2)]^2 \right\} \pm \int d^2x B_z\,, \tag{2.20}$$

where $B_z = F_{12} = \partial_x A_y - \partial_y A_x$, and the upper signs are taken for vortices and lower signs for antivortices. The first integrand in the braces is positive definite and so using the definition of quantized magnetic flux, a lower bound on the energy can be given as

$$E \geq \frac{2\pi\eta}{e}|n|\,. \tag{2.21}$$

For the lowest energy configuration, the first integrand must vanish, which gives us our first order equations

$$[(\partial_x + ieA_x) \pm i(\partial_y + ieA_y)]\phi = 0\,, \text{and} \tag{2.22}$$

$$B_z = \mp(\phi\phi^* - \eta^2)\,. \tag{2.23}$$

The solutions to these equations represent static non-interacting multi-vortex configurations. Interactions of vortices have been studied in great detail at critical coupling due to these simplifications.

If we set $e = 0$, the gauge field decouples and the scalar field now only transforms under the global $U(1)$ symmetry. Since there is no Higgs screening, the massless Goldstone excitations carry a long range force and the energy per unit length of the string diverges. The equations of motion simplifies to

$$\partial_\mu\partial^\mu\phi = -\lambda(\phi\phi^* - \eta^2)\phi\,. \tag{2.24}$$

Using the cylindrically symmetric ansatz for scalar field as before, we find that the profile function satisfies the following condition as $r \to \infty$,

$$f(r) \approx 1 - \mathcal{O}(\frac{1}{r^2})\,. \tag{2.25}$$

2.2.1 String Interactions

In the Abelian Higgs model, the interactions between N vortices that are well separated can be effectively described by simply superposing the solutions for individual

strings (Abrikosov (1957); Vilenkin and Shellard (2000)) , that is,

$$\begin{aligned}\mathbf{\Phi}(\mathbf{x}) &= \prod_{k=1}^{N} \phi_s(\mathbf{x}-\mathbf{x}_k)\,, \text{and} \\ \mathbf{A}(\mathbf{x}) &= \sum_{k=1}^{N} \mathbf{A}_s(\mathbf{x}-\mathbf{x}_k)\,. \end{aligned} \tag{2.26}$$

To validate this choice of ansatz, we consider the exact solution to be ansatz plus some residual fields as follows,

$$\mathbf{\Phi} = \mathbf{\Phi}' + \varphi, \;\; \mathbf{A} = \mathbf{A}' + \mathbf{a}\,. \tag{2.27}$$

We expect that these residual fields would only add negligible amount of energy $\epsilon_{\varphi,\mathbf{a}}$ to the energy for the multi-vortex ansatz above. The energy for the true solution would then be

$$E(\mathbf{\Phi},\mathbf{A}) = E(\mathbf{\Phi}',\mathbf{A}') + \epsilon_{\varphi,\mathbf{a}}\,. \tag{2.28}$$

By plugging in the ansatz 2.26 for two vortices into the equations of motion and assuming the asymptotic profiles 2.17 for the fields, it can be shown that the residual fields φ and $\mathbf{a}$, in the case where $\beta > 1$, behave approximately as $\mathcal{O}(\exp(-m_V d))$, where d is the separation between the two vortices. We can therefore expect that the leading order behavior for the residual energy (squaring the fields) would be as follows,

$$\epsilon_{\varphi,\mathbf{a}} \approx \mathcal{O}(\exp(-2m_V d))\,, \tag{2.29}$$

which can be ignored safely when vortices are well separated. We have used the ansatz above extensively in our numerical simulations for setting up initial field configurations.

For the case of two vortices, we can again use the asymptotic behavior of the fields to compute the interaction energy. Writing it as the sum of individual energies of the two vortices and interaction potential, that is,

$$E(\mathbf{\Phi}',\mathbf{A}') \approx E(\phi_1,\mathbf{A_1}) + E(\phi_2,\mathbf{A_2}) + E_{int}\,, \tag{2.30}$$

it can be shown that the leading order contribution to interaction energy behaves like

$$E_{int} \approx \mathcal{O}(\exp(-m_V d)) \,. \tag{2.31}$$

This result for the $\beta > 1$ case shows that the vector field dominates in this regime and vortices repel each other with an exponentially decaying force. For $\beta < 1$, however, the Higgs scalar dominates the interaction energy leading to an attractive force between the vortices. For a vortex-antivortex pair, both scalar and vector contributions to the interaction energy are negative, which means the force is always attractive between the pair. At critical value of the coupling, $\beta = 1$, scalar attraction exactly balances vector repulsion, leading to no net interaction between the vortices.

For global $U(1)$ strings, using the same approach as above, the interaction energy for well separated vortices is

$$E_{int}^{\pm} \approx \pm 4\pi\eta^2 \ln\left(\frac{R}{d}\right) \,, \tag{2.32}$$

where the upper sign is a vortex-vortex pair and the lower sign is for a vortex-antivortex pair, and R is a cutoff distance. Taking a derivative of this expression with respect to d gives us the force between a pair of vortices as follows,

$$F \approx \pm \frac{4\pi\eta^2}{d} \,. \tag{2.33}$$

This long range force is due to the massless Goldstone field.

Once the vortices are free to move, the dynamics turns out to be non-trivial even in the case of critical coupling. Multiple studies (Moriarty *et al.* (1988); Shellard and Ruback (1988); Matzner (1988)) have shown that vortex-vortex head-on scattering always occurs at 90° regardless of the initial conditions. $\beta = 1$ case is amenable to analytical studies for slowly moving vortices using moduli space methods as shown by (Ruback (1988)). The slow motion of N vortices in the configuration space can be

expected to be nearly identical to the static N-vortex solution/moduli space, M_N. At the critical coupling, energy of the N-vortex solutions has a global minimum at $2\pi N$. Near this minimum, potential energy gradients are very small, and therefore kinetic energy will dominate the motion. This also implies that vortices will move along geodesics in the moduli space M_N following metric induced by the kinetic terms in the Lagrangian. The induced metric is usually curved and leads to non-trivial scattering.

For a two vortex scattering process in $2D$, M_2 is basically a combination of two coordinates describing the overall motion of the vortices in the plane and another set of two coordinates describing the relative motion of the Higgs zeros (center of the vortices), that is, $M_2 \cong R^2 \times M_2^0$. The induced metric on M_2^0 describes the scattering of the two vortices. The symmetries of the theory, rotation and parity invariance, act as isometries on this space and lead to the following form (Ruback (1988); Vilenkin and Shellard (2000)) for the metric when the vortices are very close to each other,

$$ds^2 \approx d\rho^2 + 4\rho^2 d\psi^2 \,, \tag{2.34}$$

where ρ is half the separation distance and ψ is the orientation angle of the separation vector relative to some reference direction. The configuration of vortices remains the same if their positions are exchanged resulting in the identification $\psi \sim \psi + \pi$. The metric above has a smooth conical tip at $\rho = 0$. As a geodesic goes through through this tip, the two vortices have a head-on collision and the angle ψ changes by $\pi/2$, which explains the scattering at right angles.

Head-on collision of a vortex-antivortex pair leads to their annihilation and then formation of a new vortex-antivortex pair moving along the original axis of collision. Since the forces are short-ranged, the scattering angle for vortices goes to zero exponentially as the impact parameter is increased as demonstrated by Myers *et al.*

(1992).

Another important feature of string interactions is intercommutation or reconnection. When two strings intersect, it has been shown through multiple analytical and numerical analyses (Moriarty *et al.* (1988); Matzner (1988)) that they almost always exchange partners independent of the angle of incidence and may form interaction loops in the process. The only scenario in which this may not occur is when the strings are approaching each other at velocities very close to the speed of light. Very long strings can intercommute with themselves as well, producing loops as a result. Qualitatively, the process of intercommutation can be thought of as an extension of the right-angled scattering process for vortices in $2D$. As shown in Fig. 2.3, projections of a pair of strings moving towards each other onto two different planes can demonstrate these ideas. The projected vortex-antivortex pair in plane B would annihilate while the vortex-vortex pair in plane A would scatter off at right angles. This combination of right-angled scattering and annihilation leads to reconnection. Without this property of intercommutation, existence of cosmic strings in the early universe has been ruled out and they would not contribute to the process of galaxy formation.

Note that two kinks (sharp corners) are formed on each string after reconnection. This is because sections of the strings on the opposite sides of the intersection point point in opposite directions and have different velocities, resulting in very sharp variation of derivatives (of smooth functions) along the string.

Intercommutation is the main mechanism through which a string loses energy. If we are to observe strings formed in the early universe, the network of such strings must be in the scaling regime, that is, the energy density of strings in the universe should remain constant with time. If the energy density grew with time, which would happen when the strings only get elongated with the expansion of the universe, strings would

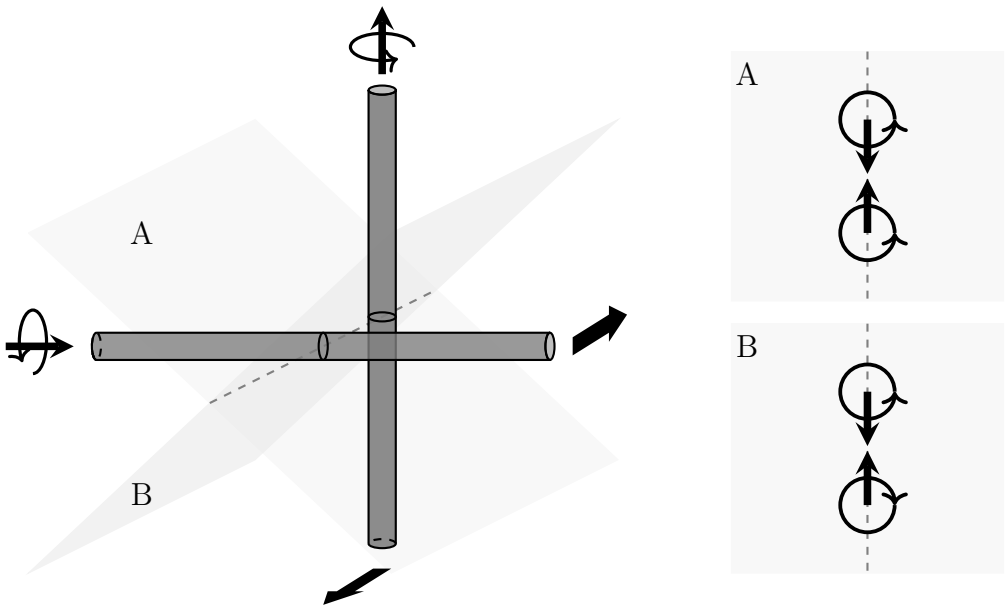

(a)

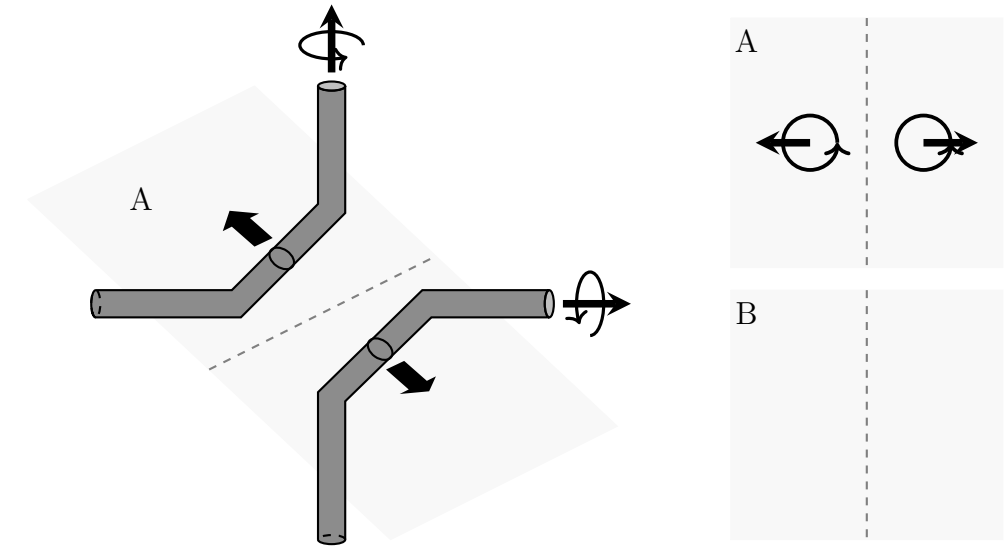

(b)

Figure 2.3: Strings (a) before and (b) after intercommutation. Initially, the two strings approach each other along the line of intersection (dashed) of the two orthogonal planes A and B. The projected vortices onto these planes are shown on the right. The vortex-vortex pair in the plane A scatter off at right angle while the vortex-antivortex pair in the plane B annihilate. The two strings end up exchanging partners with the resulting motion in directions orthogonal to the original direction of approach. Note that two kinks form on each string after intercommutation.

dominate the universe now, inconsistent with the current observations. On the other hand, if the network got diluted, the probability of detection would be negligible. Intercommutation constitutes the main mechanism for taking energy out of a dense network and achieving a scaling regime.

Every time a string intercommutes with itself, closed loops are formed. These loops will oscillate with a time period of half the loop length l. Large loops would most probably collide with other strings and intercommute, or they may break into smaller loops which would eventually radiate away through gravitional and particle radiation due to their relativistic motion. The scaling regime solution has been verified by many analytical and numerical analyses (Allen and Shellard (1990b); Copeland and Kibble (2010); Bennett and Bouchet (1988); Copeland *et al.* (1992)). In this regime, the characteristic length scale of the network becomes constant with respect to the horizon size resulting in a constant ratio of energy density in strings to the energy density of the universe, that is,

$$\frac{\rho_s}{\rho} \sim G\mu \,, \tag{2.35}$$

where G is Newton's constant. The dimensionless quantity $G\mu$ gives the strength of gravitational effects due to a string of mass per unit length μ.

Gravitational interactions offer the best chance for observing a cosmic string. Therefore, it is important to understand the gravitational effects of these defects. The gravitational field around a straight string turns out to be locally flat because tension counteracts the gravitation influence of the energy content in the string. Therefore, a test mass would not accelerate towards such a string. Globally, the metric is curved and is given as

$$ds^2 = dt^2 - dz^2 - d\rho^2 - (1 - 4G\mu)^2\rho^2 d\varphi^2 \,, \tag{2.36}$$

which can be rewritten in terms of a new azimuthal angle $\overline{\varphi} = (1 - 4G\mu)\varphi$ as

$$ds^2 = dt^2 - dz^2 - d\rho^2 - \rho^2 d\overline{\varphi}^2 \,. \tag{2.37}$$

This metric is essentially flat except that the angle $\overline{\varphi}$ varies from 0 to $2\pi - \delta$, where the deficit angle

$$\delta = 8\pi G\mu = 5.2 \left(\frac{G\mu}{10^{-6}}\right) \text{arcsec}\,, \tag{2.38}$$

is for strings formed at GUT scales.

This conical geometry leads to interesting gravitational lensing phenomena. Light from a source behind the string would get split into two at an angle of order δ, but since the spacetime is locally flat around the string, the sizes and brightness of the two images will remain the same as the original source.

Another consequence of this geometry is that the cosmic microwave background (CMB) gets affected by a string moving transversely at speed v. Radiation passing ahead of the string gets red-shifted while the radiation behind the string gets blue-shifted. This results in a discontinuity in the temperature of the CMB of the order $\delta T/T \sim G\mu v$. For fast moving strings, this discontinuity may be detectable.

As mentioned earlier, cosmic string loops themselves emit gravitational radiation and would have contributed significantly to the gravitational wave background that we detect now. Formation of cusps on the strings is a major source of this gravitational radiation. A cusp is a point at which a string moves at the speed of light for an instant emitting intense gravitational radiation in the direction of string's velocity. Given this intensity of emission from cusps, we may be able to detect gravitation radiation from even low tension strings with $G\mu \sim 10^{-10}$. Millisecond pulsars, with stability of their rotations comparable to that of atomic clocks, are easily disturbed by gravitational waves and therefore serve as excellent detectors for gravitational waves emitted by cosmic strings. The regularity of pulsar timing observed over a period of multiple

decades has constrained the energy density in gravitational wave background, which gives us the current upper bound on cosmic string tension (Blanco-Pillado *et al.* (2018b)):

$$G\mu < 1.5 \times 10^{-11} \tag{2.39}$$

In the case of a global $U(1)$ theory, the Goldstone field survives beyond the core and the energy per unit length diverges, that is,

$$\mu(r) \approx 2\pi\eta^2 \ln\left(\frac{r}{r_{core}}\right) , \tag{2.40}$$

where r_{core} is the thickness of the core. The deficit angle δ therefore increases with the distance from the core as

$$\delta(r) = 8\pi G\mu(r) , \tag{2.41}$$

which is in contrast with the case of gauge strings. Additionally, global strings would repel a test mass away from the core. The metric around a global string has also been argued to contain a singularity some distance away from the string core (Cohen and Kaplan (1988)), however, cosmic censorship hypothesis forbids naked singularities of this type.

2.2.2 Effective Actions for String Dynamics

If a string is of negligible thickness compared to its length, and curvature is small at any point compared to its thickness, we can simplify our models describing string dynamics. Massive transverse degrees of freedom can be integrated out leaving us with Higgs zeros as the only relevant degrees of freedom. Higgs zeros denoting the location $x^\mu(\sigma^a)$ of the string core would then sweep a worldsheet, where $\sigma^a = (\sigma, \tau)$ are the two worldsheet coordinates. The action for such a zero thickness string is the well known Nambu-Goto action (Vilenkin and Shellard (2000))

$$S = -\mu \int d^2\sigma \sqrt{-\det(g_{\mu\nu} x^\mu_{,a} x^\nu_{,b})} , \tag{2.42}$$

where μ is the string tension, $g_{\mu\nu}$ is the spacetime metric and $x^{\mu}_{,a} = \partial x^{\mu}/\partial\sigma^{a}$. The parameter τ can be conveniently chosen to be the time t itself, while σ can be chosen to represent the length along the string by satisfying the following gauge conditions,

$$\dot{\mathbf{x}}.\mathbf{x}' = 0\,, \;\; \dot{\mathbf{x}}^2 + \mathbf{x}'^2 = 1\,, \tag{2.43}$$

where $\mathbf{x}(\sigma, t)$ is the three-vector describing string motion, and $\dot{\mathbf{x}} = \partial\mathbf{x}/\partial t$, and $\mathbf{x}' = \partial\mathbf{x}/\partial\sigma$ are the velocity perpendicular to the string and the derivative along the string, respectively. Varying the action then gives the equation of motion,

$$\ddot{\mathbf{x}} - \mathbf{x}'' = 0\,. \tag{2.44}$$

This wave equation on the string has the following general solution,

$$\mathbf{x}(\sigma, t) = \frac{1}{2}\left[\mathbf{a}(\sigma - t) + \mathbf{b}(\sigma + t)\right]\,, \tag{2.45}$$

where $\mathbf{a}$ and $\mathbf{b}$ are the right and left moving modes, respectively. From the stress energy tensor, the total energy of such a string comes out to be simply $E = \mu\int d\sigma$.

For loops of total length L, the functions $\mathbf{a}$ and $\mathbf{b}$ are periodic in σ, that is,

$$\mathbf{a}(\sigma + L) = \mathbf{a}(\sigma)\,, \;\; \mathbf{b}(\sigma + L) = \mathbf{b}(\sigma)\,. \tag{2.46}$$

The gauge choice used above forces the magnitude of $\mathbf{a}$ and $\mathbf{b}$ to be 1. From the periodicity of these functions, wave equation tells us that that a loop will undergo periodic motion with time period $T = L/2$ (relativistic), since

$$\mathbf{x}(\sigma + L/2, t + L/2) = \mathbf{x}(\sigma, t)\,. \tag{2.47}$$

Now, specific points on a loop may move with the speed of light. These points are the previously mentioned cusps and kinks. On a cusp $\mathbf{x}' = 0$, which results in instantaneous luminal motion, $\dot{\mathbf{x}} = 1$. Cusps contribute significantly to the gravitational radiation and have very unique observational signatures. Kinks, on the other hand,

are sharp corners on a loop with discontinuous **a** and **b**. They are usually created upon intercommutation when $\dot{\mathbf{x}}(\sigma, \tau_{int})$ and $\mathbf{x}'(\sigma, \tau_{int})$ vary sharply as functions of the length parameter σ.

In the case of global strings, however, we have long range forces and the energy diverges logarithmically. The dynamics for such strings is much clearer when the massless Goldstone degree of freedom is described using an anti-symmetric tensor $B^{\mu\nu}$ through the following relation,

$$\eta \partial_\mu \alpha = \frac{1}{2} \epsilon_{\mu\nu\lambda\rho} \partial^\nu B^{\lambda\rho} \,. \tag{2.48}$$

The action with the above reformulation was first derived by Kalb and Ramond (1974); Vilenkin and Vachaspati (1987) and is given as

$$S = -\mu \int d^2\sigma \sqrt{-\det(g_{\mu\nu} x^\mu_{,a} x^\nu_{,b})} + \frac{1}{6} \int d^4x H_{\mu\nu\lambda} H^{\mu\nu\lambda} + 2\pi\eta \int d^2\sigma \epsilon^{ab} x^\mu_{,a} x^\nu_{,b} B^{\mu\nu} \,, \tag{2.49}$$

where $H^{\mu\nu\lambda} = \partial^\mu B^{\nu\lambda} + \partial^\lambda B^{\mu\nu} + \partial^\nu B^{\lambda\mu}$ is the field strength tensor for the antisymmetric field. The last term in the action represents the coupling of the string to the Goldstone field through the antisymmetric tensor $B_{\mu\nu}$.

The two actions described above have been used effectively to study phenomena at cosmological scales and in superconductors. For our investigations, however, we rely on full field theory simulations and do not significantly utilize these approximations.

2.3 $SU(2)$ Monopoles

Here we look at 't Hooft-Polyakov monopoles ('t Hooft (1974); Polyakov (1974)) in the $SU(2)$ model,

$$\mathcal{L} = \frac{1}{2} (D^\mu \phi)^a (D_\mu \phi)^a - \frac{1}{4} W^{a\mu\nu} W^a_{\mu\nu} - \frac{\lambda}{4} (\phi^a \phi^a - \eta^2)^2 \,, \tag{2.50}$$

where $a = 1, 2, 3$, the covariant derivative is defined as

$$(D_\mu \phi)^a = \partial_\mu \phi^a + e \epsilon^{abc} W^b_\mu \phi^c \,, \tag{2.51}$$

and the gauge field strength is given as

$$W^a_{\mu\nu} = \partial_\mu W^a_\nu - \partial_\nu W^a_\mu + e\epsilon^{abc} W^b_\mu W^c_\nu \,. \tag{2.52}$$

The equations of motion obtained by varying the action are

$$(D_\mu(D^\mu\phi))^a = -\lambda(\phi^b\phi^b - \eta^2)\phi^a \,, \text{and} \tag{2.53}$$

$$(D_\mu W^{\mu\nu})^a = e\epsilon^{abc}(D^\nu\phi)^b\phi^c \,. \tag{2.54}$$

We will use temporal gauge ($W^a_0 = 0$). By rescaling the fields and spatial coordinates appropriately, and setting the vacuum expectation value and coupling constants to one, that is, $\eta = e = 1$, it is easily seen that λ is the only parameter in the theory that controls the mass and size of the monopoles.

Varying the action with respect to the metric gives us the following expression for energy of a static configuration,

$$E = \int d^3x [\frac{1}{2}(D_i\phi)^a(D_i\phi)^a + \frac{1}{4}W^a_{ij}W^a_{ij} + \frac{\lambda}{4}(\phi^a\phi^a - 1^2)^2] \,. \tag{2.55}$$

To solve for static configurations, we have to minimize the above energy functional. Also, an essential condition for the existence of finite energy solutions is that the terms in the integrand vanish individually at spatial infinity. This requires

$$\phi^a\phi^a \to 1, \quad (D_i\phi)^a \to 0, \quad W^a_{ij} \to 0 \tag{2.56}$$

at spatial infinity.

The simplest ansatz for the field configuration with a non-trivial topology would have spherical symmetry. We choose the Higgs isovectors such that it always points along the radial position vector, that is, $\hat{\phi}^a = \hat{r}^a$, where $\hat{r}^a = r^a/|\vec{r}|$ and $\hat{\phi}^a = \phi^a/|\vec{\phi}|$. This means that we can write our Higgs fields as

$$\phi^a = h(r)\hat{r^a} \,. \tag{2.57}$$

The direction for gauge fields can be shown, by satisfying the condition that the covariant derivative of the Higgs fields vanishes at spatial infinity, to take the form below

$$W_i^a = \frac{(1-k(r))}{r}\epsilon^{aij}\hat{r}^j \,. \tag{2.58}$$

To solve for the profile functions $h(r)$ and $k(r)$, we plug these last expressions into the general equations of motions. This gives us two coupled ordinary differential equations as follows,

$$h''(r) + \frac{2}{r}h'(r) = \frac{2}{r^2}k(r)^2 h(r) - \lambda\left(h(r)^2 - 1\right)h(r)\,, \tag{2.59}$$

$$k''(r) = \frac{1}{r^2}(k(r)^2 - 1)k(r) + h(r)^2 k(r)\,. \tag{2.60}$$

These differential equations in one dimension are solved numerically with the Gauss-Newton method for different values of λ and with boundary conditions, $h(r) \to 1$ and $k(r) \to 0$ as $r \to \infty$, and $h(r) \to 0$ and $k(r) \to 1$ as $r \to 0$. Fig. 2.4 shows a plot of these profile functions for $\lambda = 1$. The mass of the monopole is shown in Table 2.1 for sample values of λ. We will use these solutions in our initial guess for the monopole-antimonopole field configuration.

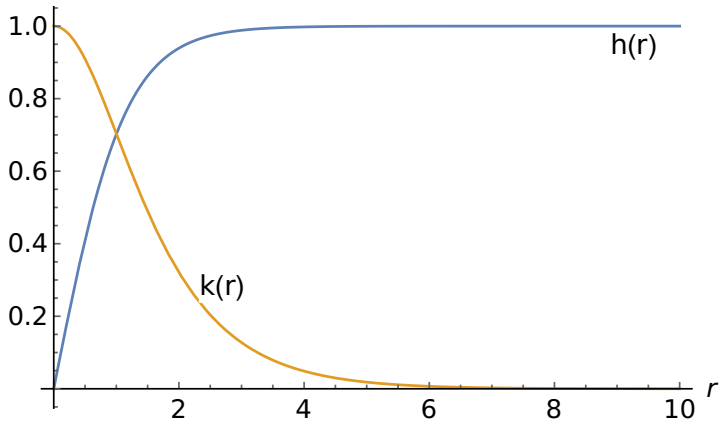

Figure 2.4: Numerically generated profile functions, $h(r)$ and $k(r)$, for $\lambda = 1$.

Table 2.1: Mass of the monopole as a function of λ.

λ	Mass in units of 4π
0.0	1.000
0.25	1.185
0.50	1.232
0.75	1.264
1.0	1.287

As we saw for the other defects, we can again define a conserved topological charge as follows,

$$n = \frac{1}{8\pi} \int_S d\hat{n}^i \epsilon_{ijk} \epsilon_{abc} \hat{\phi}^a \partial_j \hat{\phi}^b \partial_k \hat{\phi}^c \,, \tag{2.61}$$

where $\hat{n}$ is the outward unit normal to a closed surface S and $\hat{\phi}^a = \phi^a/|\vec{\phi}|$. The value of n is always an integer and tells us how many times the unit sphere in the internal space of the Higgs fields wraps around a sphere at infinity in real space.

In the spherically symmetrical solution above, it should be noted that the Higgs fields take values in the vacuum manifold at spatial infinities. A non-zero vacuum expectation value of ϕ^a spontaneously breaks the $SU(2)$ symmetry to a $U(1)$ subgroup and two of the three gauge fields acquire a mass, $m_V = e\eta$, while the third is the "photon". The scalar excitations also become massive with mass, $m_S = \sqrt{2\lambda}\eta$ (note that η and e are free variables again). Like in the case of kinks and vortices, the Compton wavelengths associated with these mass scales define the size of a magnetic monopole.

In order to compute the magnetic charge for these solitons, we need to first find an expression for magnetic flux that is coming out/in. In $SU(2)$ gauge theory, there is no clear notion of an electromagnetic field strength tensor. However, near vacuum, an unbroken $U(1)$ group lets us define one. For the spherically symmetric solution, if

the Higgs isovector is pointing in the $\hat{\phi}^a$ direction, vanishing covariant derivative far away from the soliton, $D_\mu \hat{\phi} = 0$, helps us define the form of the gauge field in that region. The electromagnetic field strength then points in the unbroken direction in the $\mathfrak{su}(2)$ algebra, that is, along the radial direction $\hat{\phi}^a$. The general solution for the gauge field is (akin to Helmholtz decomposition),

$$W_\mu = \hat{\phi}^a A_\mu + \frac{1}{e}\epsilon^{abc}\partial_\mu \hat{\phi}^b \hat{\phi}^c \,, \tag{2.62}$$

where A_μ is an arbitrary function. The gauge invariant electromagnetic field tensor for this field can then be computed from

$$\begin{aligned} F_{\mu\nu} &= W^a_{\mu\nu}\hat{\phi}^a = (\partial_\mu A_\nu - \partial_\nu A_\mu) + \frac{1}{e}\epsilon^{abc}\hat{\phi}^a (D_\mu \hat{\phi})^b (D_\nu \hat{\phi})^c \\ &= \partial_\mu A_\nu - \partial_\nu A_\mu + \frac{1}{e}\epsilon^{abc}\hat{\phi}^a \partial_\mu \hat{\phi}^b \partial_\nu \hat{\phi}^c, \quad \text{if } |\phi| = 1 \,. \end{aligned} \tag{2.63}$$

These expressions are identical to those proposed by 't Hooft (1974) in the region outside the monopole. The magnetic field follows from the usual expression,

$$B_i = -\frac{1}{2}\epsilon_{ijk}F_{jk} = -\frac{1}{2}\epsilon_{ijk}\left(\partial_j A_k - \partial_k A_j + \frac{1}{e}\epsilon^{abc}\hat{\phi}^a \partial_j \hat{\phi}^b \partial_k \hat{\phi}^c\right) . \tag{2.64}$$

Far away from the magnetic monopole, $A_\mu = 0$, and there is no electric field. The magnetic field in that case becomes,

$$B_i = -\frac{1}{2g}\epsilon_{ijk}\epsilon^{abc}\hat{\phi}^a \partial_j \hat{\phi}^b \partial_k \hat{\phi}^c = -\frac{1}{er^2}\hat{r}_i \,. \tag{2.65}$$

Integrating this magnetic flux over a spherical surface at infinity gives the magnetic charge for a magnetic monopole as follows,

$$g = \lim_{r\to\infty} \oint \mathbf{B}.\mathbf{dS} = -\frac{4\pi}{e} \,, \tag{2.66}$$

where we used the expression for topological charge n in the last equality and set it to one. In general, for a configuration of higher topological number, the magnetic charge

is quantized and is given as $g = -4\pi n/e$. Such monopole solutions are very difficult to find but can be constructed using the Nahm transforms and other sophisticated methods in the BPS limit.

In the BPS limit, scalar self-coupling constant $\lambda \to 0$. Like in the case of $U(1)$ gauge strings, the second order equations of motion simplify to a first order system. To see this, the energy functional in this limit becomes

$$E_{\lambda=0} = \int d^3x \left[\frac{1}{2}(D_i\phi)^a(D_i\phi)^a + \frac{1}{2}H_i^a H_i^a\right] , \tag{2.67}$$

where $H_i^a = -\frac{1}{2}\epsilon_{ijk}W_{jk}^a$. For a magnetic monopole type solution, the energy functional must be minimized. Using the techniques developed by Bogomolny (1976), and Prasad and Sommerfield (1975), we can write down the following inequality,

$$\int d^3x \left[\frac{1}{2}(H_i^a - D_i\phi^a)(H_i^a - D_i\phi^a)\right] \geq 0 \, , \tag{2.68}$$

since the integrand is positive definite. The equality holds when the Bogomolny equation $D_i\phi^a = H_i^a$ is satisfied. The inequality above can be rewritten as

$$E_{\lambda=0} \geq \int d^3x H_i^a D_i\phi^a \, . \tag{2.69}$$

The right hand side of this inequality turns out to be proportional to the magnetic charge, resulting in a lower bound on the energy of a BPS monopole given as

$$E_{\lambda=0} \geq \frac{4\pi\eta}{e} \, . \tag{2.70}$$

The equations of motion can be solved analytically for the minimum energy BPS solution with topological charge $|n| = 1$, which turns out to be

$$h(r) = \coth(m_V r) - \frac{1}{m_V r} \tag{2.71}$$

$$k(r) = \frac{m_V r}{\sinh(m_V r)} \, . \tag{2.72}$$

To construct solutions with higher topological numbers, Nahm (1978) found a way to transform the BPS monopole configurations into a completely different mathematical structure. The main idea is to map solutions of the Bogomolny equation in $\mathbb{R}^3$ to solutions of the Nahm equation,

$$\frac{dT_i(s)}{ds} = \frac{1}{2}\epsilon_{ijk}\left[T_j(s), T_k(s)\right] , \tag{2.73}$$

where $T_1(s)$, $T_2(s)$, and $T_3(s)$ are $n \times n$ matrices with $s \in [-1, 1]$, and n is the topological charge of the monopole configuration. The Nahm equation is, in general, not easy to solve, however, some non-trivial solutions are known. Once the Nahm equation has been solved, the inverse transform can be done analytically or numerically to get an n-monopole configuration.

Another technique that can be used to look for monopole solutions was demonstrated by Taubes (1982a,b). He used Morse theory to uncover saddle point solutions in $SU(2)$ gauge theory. Morse theory basically relates the topology of a smooth manifold to the stationary points of a smooth function on the same manifold. The classic example that demonstrates these ideas is that of a torus standing above a plane as shown in the Fig. 2.5.

Here we can define a simple function that assigns each point on the torus a height above the reference plane. This function has its maximum and minimum at P_3 and P_0, respectively. Topology of the torus, however, also gives this function two saddle points, P_2 and P_1. On compact manifolds, the study of non-contractible loops is a standard method for finding stationary points if the function has one minimum. In the case of torus, the height function has a minimum at P_0. If we consider the maximum height on each non-contractible through P_0, the infimum would be at P_1 and supremum at P_2, which are the saddle points. For non-compact manifolds, however, this approach may fail.

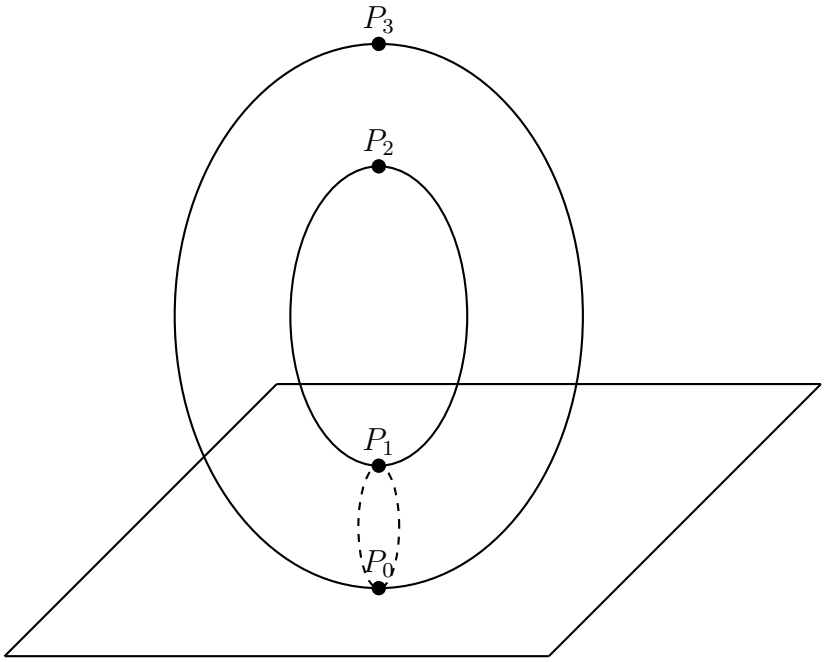

Figure 2.5: A torus with stationary points of a height function on it. Non-contractible loops through a global minimum P_0 help find the saddle points P_1 and P_2 on this torus.

We can apply these ideas to a field theories as well, where we study non-contractible loops on the configuration space of all finite energy static solutions, and look for the stationary points of the energy functional. It is assumed that there are unique minimum energy configuration with energy E_0 in these theories. As in the case of torus, it has been shown in multiple cases that there are non-contractible loops that go through the infimum of the maximum energy, E_1, and are saddle point solutions of the field equations.

Taubes (1982a,b) applied this method to prove the existence of a saddle point with topological charge of zero. This solution could be described as an unstable monopole-antimonopole bound state where Coulomb repulsion is balanced by the scalar attraction and any rotation of the monopole relative to the antimonopole leads to annihilation of the pair. Manton (1983) also used the same technique to uncover the saddle point solution in the electroweak theory.

2.3.1 Monopole Interactions and Dynamics

There is only one massless carrier for interactions between magnetic monopoles. The resulting magnetic Coulombic force has a long range and will therefore dominate interactions between well separated magnetic monopoles. Like electric charges, two magnetic monopoles will repel each other while a monopole attracts an antimonopole. Other forces due to the massive scalar and vectors decay exponentially with separation. In the BPS limit ($\lambda \to 0$), however, scalar field becomes massless and contributes a long range force to the interactions. This scalar attraction balances the Coulombic repulsion between the monopoles, resulting in zero net force between BPS monopoles. An interesting thing to note here is that unlike electromagnetism which is linear, the particles (monopoles) and the interactions between them are completely predicted by the $SU(2)$ gauge theory itself.

Many analytical and numerical investigations have provided insight into the multi-monopole dynamics. Like in the case of vortices, moduli space methods have been very fruitful in developing understanding of slow moving magnetic monopoles in the BPS limit. The moduli space M_N for static N-monopole solutions is a submanifold of the configuration space C_N and is endowed with a metric induced by the kinetic terms. Slow moving configurations would remain very close to M_N and therefore can be described well by geodesic motion along the induced metric. The M_N turns out to be a hyperKähler manifold of dimension $4N$. As we did for vortices, we can split M_N into a part that describes the overall motion of the monopoles and another part that describes relative motion of the Higgs zeros. This decomposition is expressed as follows,

$$M_N \simeq \mathbb{R}^3 \times \frac{S^1 \times M_N^0}{\mathbb{Z}_N}\,, \tag{2.74}$$

where the part describing Higgs zeros, M_N^0, can be isolated from the flat $\mathbb{R}^3 \times S^1$ part

(Manton (1982b)).

On a two monopole effective moduli space, M_2^0, the $SO(3)$ isometries (representing the symmetries of the physical theory) result in the following form for the metric (Atiyah and Hitchin (1985))

$$ds^2 = f^2(\rho)\, d\rho^2 + a^2(\rho)\, d\psi_1^2 + b^2(\rho)\, d\psi_2^2 + c^2(\rho)\, d\psi_3^2\,, \tag{2.75}$$

where the angles ψ_1, ψ_2, ψ_3 are given in terms of Euler angles and physically describe the relative orientation of the monopole pair, ρ is related to the separation between monopoles, functions $a(\rho)$, $b(\rho)$, $c(\rho)$ are determined analytically by solving three coupled differential equations resulting from the hyperKähler character of the metric, and $f(\rho)$ has been defined in multiple ways in the literature (Manton and Sutcliffe (2004)) in terms of $a(\rho)$, $b(\rho)$, $c(\rho)$.

Without delving into technical details of the calculations, we learn that the two monopoles at large ρ maintain their spherical shapes with separation distance given by ρ. However, when ρ takes its minimal value of $\pi/2$, the two monopoles combine to form a toroidal shape. Angular momentum about an axis joining the centers of the two well separated monopoles changes the relative phase and they acquire opposite electric charges (dyons). For the toroidal configuration, rotation about its central axis has no affect on the fields modulo gauge transformations. When the two monopoles are constrained to move in a plane and approach each other to collide head on, the resulting metric is the same as that for two vortices (Eq. (2.34)), that is,

$$ds^2 = d\rho^2 + 4\rho^2 d\psi^2\,. \tag{2.76}$$

As in the case of vortices, monopoles scatter off at right angles to their incoming direction. Another interesting geodesic was discovered by Bates and Montgomery (1988) and it describes bounded motion. This happens when ρ assumes a special

value such that $|a| = |c|$. This leads to a configuration that precesses in space about a fixed line.

Chapter 3

MONOPOLE-ANTIMONOPOLE INTERACTIONS

In this chapter, we discuss results from our papers on monopole interactions. (Saurabh and Vachaspati (2017, 2019a)). As discussed in the first chapter, dynamics involving both monopoles and antimonopoles has not received a lot of attention and therefore, to enhance our understanding of the particle physics processes involving magnetic monopoles, we took the first steps towards full field theory simulations involving these topological objects. Based on a qualitative understanding of the scalar and vector forces between a monopole and an antimonopole at separation d, Taubes sketched the interaction potential as

$$V(d,\gamma) = 4\pi \left(-\frac{1}{d} - \frac{2e^{-d}}{d}\cos\gamma - \frac{e^{-\sqrt{\lambda}d}}{d}(1-e^{-d}) \right) , \tag{3.1}$$

where the first term on the right hand side is the usual attractive Coulomb interaction, the second term is a correction term which represents short range interactions mediated by the two massive vector bosons $W^{\pm}$, γ is the relative twist angle, and the last term is due to scalar interactions. (Note: in Taubes' notation, the twist is called θ where $\theta = \pi - \gamma$.) This vector interaction is attractive for $\cos\gamma > 0$ and repulsive for $\cos\gamma < 0$, in which case the attractive Coulomb and repulsive forces can balance at some separation, leading to a saddle point solution. Any perturbation to this solution that untwists the pair will destabilize the solution, and the monopole and antimonopole will eventually radiate, as shown by Vachaspati (2016c).

We will see that the expression for $V(d,\gamma)$ in Eq. (3.1) provides a good qualitative picture but does not provide a good fit to the numerical data. This can be expected because the terms in Eq. (3.1) assume point-like monopoles. In reality, monopoles are

extended objects and a monopole-antimonopole can partially annihilate as they are brought closer together, *i.e.* when the cores of the monopole-antimonopole overlap there is a reduction in the volume occupied by the cores. Further, the reduction of energy depends on the extent of partial annihilation that, in turn, can depend on the amount of twist. Thus the actual potential can be more complicated than that given by Eq. (3.1).

A goal of our work was to rigorously determine $V(d, \gamma)$. Our numerical approach can be applied to *any* values of model parameters, and we were able to reconstruct all the fields for the monopole-antimonopole system. In particular, we calculated their interaction energy, the size, and energy, of the monopole-antimonopole bound state, for a range of couplings. For a special twist and separation we can recover the sphaleron that was also investigated numerically by Kleihaus and Kunz (2000) by solving the static equations of motion by first taking an axially symmetric ansatz for the fields. In contrast, we employed constrained relaxation over an entire three dimensional grid without assuming any symmetries, and we also studied monopole-antimonopole pairs away from the sphaleron.

3.1 Equations of Motion

We fully expand the equations of motion that we introduced in the last chapter and modify them a little for numerical stability as follows,

$$\partial_t^2 \phi^a = \nabla^2 \phi^a - g\epsilon^{abc}\partial_i \phi^b W_i^c - g\epsilon^{abc}(D_i\phi)^b W_i^c - \lambda(\phi^b\phi^b - \eta^2)\phi^a - g\epsilon^{abc}\phi^b \Gamma^c \,, \quad (3.2)$$

$$\partial_t W_{0i}^a = \nabla^2 W_i^a + g\epsilon^{abc} W_j^b \partial_j W_i^c - g\epsilon^{abc} W_j^b W_{ij}^c - D_i \Gamma^a - g\epsilon^{abc}\phi^b (D_i\phi)^c \,, \quad (3.3)$$

$$\partial_t \Gamma^a = \partial_i W_{0i}^a - g_p^2[\partial_i (W_{0i}^a) + g\epsilon^{abc} W_i^b W_{0i}^c + g\epsilon^{abc}\phi^b (D_t\phi)^c] \,, \quad (3.4)$$

where we are using temporal gauge ($W_0^a = 0$), $\Gamma^a = \partial_i W_i^a$ are introduced as new variables, and g_p^2 is a numerical parameter that we can choose to ensure numerical stability. By rescaling the fields and spatial coordinates appropriately, and setting

the vacuum expectation value and coupling constants to one, that is, $\eta = g = 1$, it is easily seen that λ is the only parameter in the theory that controls the mass and size of the monopoles.

3.2 Monopole-Antimonopole Configuration

We solved the equations of motion presented in the previous section in the static form numerically using a fixed point iteration scheme. This scheme relaxes an initial guess field configuration at each iteration step. As with all relaxation schemes, a good initial guess was important for our method to converge.

First, before constructing a gauge for a monopole-antimonopole pair, we needed to determine how anti-monopoles look like. To get an antimonopole, we can simply invert the $\hat{\phi}^a$ for the monopole (see Fig. 3.1b). This gives

$$\phi^a = -h(r)\hat{r^a} = \frac{h(r)}{r}(-x, -y, -z)\,. \tag{3.5}$$

However, this is not the only possibility. Any further local rotation of the directions of ϕ^a will also have the topology of an antimonopole. These local rotations are irrelevant if we consider an antimonopole in isolation and all such gauge rotated antimonopoles have the same energy. However, when we patch a monopole and an antimonopole together, there is an alignment issue, and the monopole-antimonopole pair may have different energies depending on their "relative twist". For example, in Fig. 3.2, we show Higgs vectors for the monopole described above and the antimonopole configuration of Eq. (3.5). This monopole-antimonopole configuration has twist equal to π. In Fig. 3.2, we also show the zero twist case, in which the antimonopole has only the third component of the Higgs inverted (see Fig. 3.1c), that is,

$$\phi^a = \frac{h(r)}{r}(+x, +y, -z)\,. \tag{3.6}$$

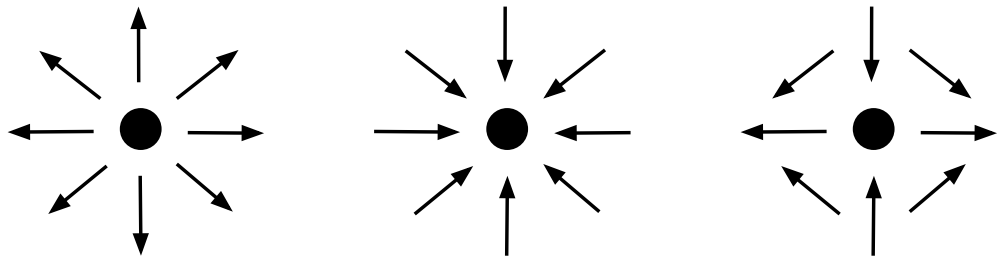

(a) $\vec{\phi} = h(r)(\hat{x} + \hat{y} + \hat{z})$ (b) $\vec{\phi} = -h(r)(\hat{x} + \hat{y} + \hat{z})$ (c) $\vec{\phi} = h(r)(\hat{x} + \hat{y} - \hat{z})$

Figure 3.1: Higgs isovectors about (a) monopole, (b) an antimonopole with all vectors inverted, and (c) an antimonopole with all vectors inverted in z direction only.

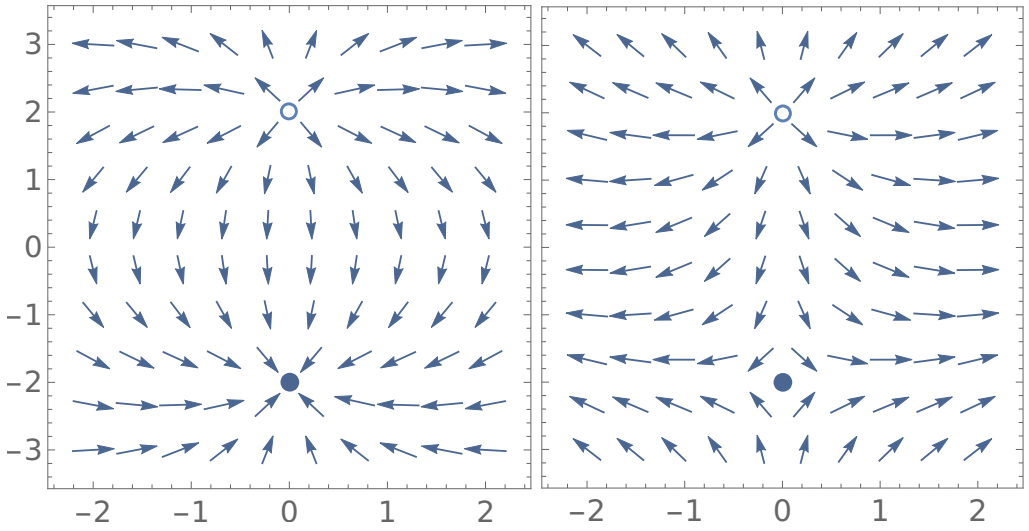

Figure 3.2: Higgs vectors in the $xz-$plane for twist $= \pi$ (left) and twist $= 0$ (right). The Higgs zeros are located at $(0, 2)$ and $(0, -2)$, shown as filled and unfilled circles.

Intermediate between the two cases of Eqs. (3.5) and (3.6), there is a continuous set of configurations that can be obtained by rotations of the scalar field directions along the z-axis. The general configuration of the twisted monopole-antimonopole

Higgs field can be written as

$$\hat{\phi}^1 = (\sin\theta\cos\bar{\theta}\cos\gamma - \sin\bar{\theta}\cos\theta)\cos(\varphi - \gamma/2) - \sin\theta\sin\gamma\sin(\varphi - \gamma/2)\,, \tag{3.7}$$

$$\hat{\phi}^2 = (\sin\theta\cos\bar{\theta}\cos\gamma - \sin\bar{\theta}\cos\theta)\cos(\varphi - \gamma/2) - \sin\theta\sin\gamma\cos(\varphi - \gamma/2)\,, \tag{3.8}$$

$$\hat{\phi}^3 = \cos\theta\cos\bar{\theta} + \sin\theta\sin\bar{\theta}\cos\gamma\,, \tag{3.9}$$

where, as shown in Fig. 3.3, θ and $\bar{\theta}$ are the angles measured from the the z-axis to the position vectors centered at the monopole and antimonopole, and φ is the azimuthal angle; γ is the relative twist angle and takes values from 0 to 2π. In Cartesian coordinates we can write these position vectors as

$$r_m = |\mathbf{x} - \mathbf{x}_m|,\; r_{\bar{m}} = |\mathbf{x} - \mathbf{x}_{\bar{m}}|\,, \tag{3.10}$$

where $\mathbf{x}_m = (0, 0, z_0)$ and $\mathbf{x}_{\bar{m}} = (0, 0, -z_0)$. Therefore, Eqns. (3.7)-(3.9) are expressed in Cartesian system as follows,

$$r_m r_{\bar{m}}\hat{\phi}^1 = (cx + sy)\left[(z + z_0)\cos\gamma - (z - z_0)\right] - (cy - sx)r_{\bar{m}}\sin\gamma\,, \tag{3.11}$$

$$r_m r_{\bar{m}}\hat{\phi}^2 = (cy - sx)\left[(z + z_0)\cos\gamma - (z - z_0)\right] + (cx + sy)r_{\bar{m}}\sin\gamma\,, \tag{3.12}$$

$$r_m r_{\bar{m}}\hat{\phi}^3 = (z - z_0)(z + z_0) + (x^2 + y^2)\cos\gamma\,, \tag{3.13}$$

where $c \equiv \cos\gamma$ and $s \equiv \sin\gamma$. With this ansatz, we can write our initial guess for the Higgs field configuration as

$$\phi^a = h(r_m)h(r_{\bar{m}})\hat{\phi}^a\,. \tag{3.14}$$

Our ansatz for the gauge fields follows from the requirement that the covariant derivatives of the Higgs isovector vanish, $D_\mu\hat{\phi} = 0$, at spatial infinity. This gives

$$W_\mu^a = -\epsilon^{abc}\hat{\phi}^b\partial_\mu\hat{\phi}^c\,. \tag{3.15}$$

We include profile functions to obtain our initial guess for the gauge fields

$$W_\mu^a = -(1 - k(r_m))(1 - k(r_{\bar{m}}))\epsilon^{abc}\hat{\phi}^b\partial_\mu\hat{\phi}^c\,. \tag{3.16}$$

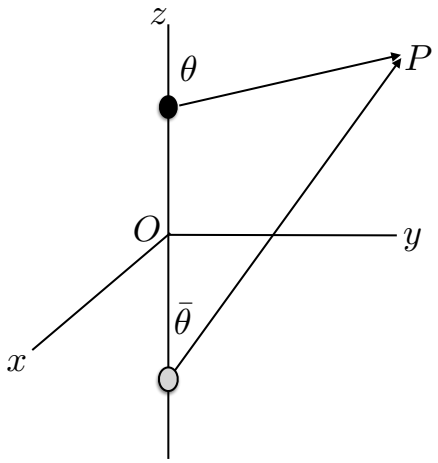

Figure 3.3: The physical configuration of the monopole-antimonopole pair.

This initial guess automatically satisfies the asymptotic conditions in Eq. (2.56) for finite energy configurations.

We can see that the twist has a gauge invariant meaning in two ways. First, the energy is gauge invariant and by explicit calculation we see that the energy of the configuration depends on the twist. Second, the twist can be expliclty defined in terms of the Chern-Simons number as demonstrated by Klinkhamer and Manton (1984). The bound state solution with twist of π is the sphaleron with Chern-Simons number of 1/2.

3.3 Twisted Dipole Gauge

We would like to minimize the energy in Eq. (2.55) but with the constraints that the monopole and antimonopole locations and their relative twist are held fixed. We have found a simple scheme to impose such constraints, in part by making use of the topology of the monopole and antimonopole. The key realization was that local gauge transformations can be made to freely choose the direction $\hat{\phi}^a$ at any spatial point. For example, the simplest choice would be to adopt the "unitary gauge" in which the

Higgs is spatially uniform. However, then the gauge fields are singular and this makes the unitary gauge unsuitable for numerical work. Instead we adopt the "twisted dipole" gauge which is that $\hat{\phi}^a$ is fixed by Eqs. (3.7), (3.8), and (3.9) throughout the numerical relaxation. This gauge choice automatically fixes the locations of the monopole and antimonopole due to the topology, and it also fixes the twist. The locations of the monopoles were chosen to lie within a cell of the lattice, not on a vertex. This avoids evaluation of the fields at the centers of the monopoles and the possibility of any fluctuations during field relaxation that can move the location of the monopoles.

Since we fixed the direction of Higgs field isovectors at each spatial point, only the magnitude of the Higgs field can vary and it is unnecessary to relax each of the components separately. Instead, we write $\phi^a = |\phi|\hat{\phi}^a$ and relax $|\phi|$ according to the equation

$$\nabla^2|\phi| = |\phi|\partial_i\hat{\phi}^a\partial_i\hat{\phi}^a + g^2|\phi|W_i^aW_i^a - g^2|\phi|W_i^aW_i^b\hat{\phi}^a\hat{\phi}^b - 2g|\phi|\epsilon^{abc}W_i^a\partial_i\hat{\phi}^b\hat{\phi}^c + \lambda(|\phi|^2-1)|\phi| \,. \tag{3.17}$$

Thus, we have 1 equation for $|\phi|$, 9 equations for W_i^a, and 3 equations for Γ^a. However, in the static case, and since we were working in temporal gauge, the equations for Γ^a are trivial. This leaves us with 10 non-trivial equations to solve.

3.4 Numerical Solution

To see how our numerical scheme works, we first set all the time derivatives to zero in the equations for $|\phi|$ and W_i^a and discretize the spatial derivatives. Our discretized equations at a given lattice point can be written in the following generic form,

$$\mathbf{E}[\{f_\beta\}] = 0 \,, \tag{3.18}$$

where $\{f_\beta\}$ denotes the set of fields, and $\mathbf{E}$ is the array of discretized equations obtained from Eqs. (3.2)-(3.4). Now, if we use second order spatial derivatives, the Laplacian term in these equations can be written as

$$\begin{aligned}\nabla^2 f(i,j,k) \to -\frac{6}{\delta^2} f(i,j,k) + \frac{1}{\delta^2}[f(i+1,j,k) \\ + f(i-1,j,k) + f(i,j+1,k) + f(i,j-1,k) \\ + f(i,j,k+1) + f(i,j,k-1)]\,,\end{aligned}$$

where f denotes any one of the fields and δ is the lattice spacing. Then we re-write Eq. (3.18) for the field f_α as

$$f_\alpha(i,j,k) = \frac{\delta^2}{6}\mathbf{E}_\alpha[\{f_\beta\}] + f_\alpha(i,j,k)\,. \tag{3.19}$$

So far this is exactly equivalent to Eq. (3.18), but now we take the left-hand side at the current (n^{th}) iteration step and the right-hand side at the previous iteration step

$$f_\alpha^{(n)}(i,j,k) = \frac{\delta^2}{6}\mathbf{E}_\alpha[\{f_\beta^{(n-1)}\}] + f_\alpha^{(n-1)}(i,j,k)\,. \tag{3.20}$$

In fact, once a field is updated at some point (i,j,k), that value is immediately used on the right-hand side for the next computation. In our numerical runs, we employed this approach but used sixth order derivatives for better accuracy. Then the numerical coefficient of the $\mathbf{E}_\alpha$ term is $6/49$ instead of $1/6$.

For most of our simulations, we chose a cubic lattice with 128^3 lattice points and lattice spacing $\delta = 0.2$ and Dirichlet boundary conditions. Since we had set $g = 1 = \eta$, the mass of the heavy gauge fields is $m_v = g\eta = 1$ and the scalar mass is $m_s = \sqrt{2\lambda}\eta = \sqrt{2\lambda}$. The monopole width is primarily set by the mass of the vector field and so the core of the monopole is resolved by $\sim 5^3$ lattice points in our simulations.

The monopole and antimonopole locations were fixed at $z = \pm(z_0 + \delta/2)$ respectively. With the offset by half a lattice spacing, we ensure that the zeros of the Higgs

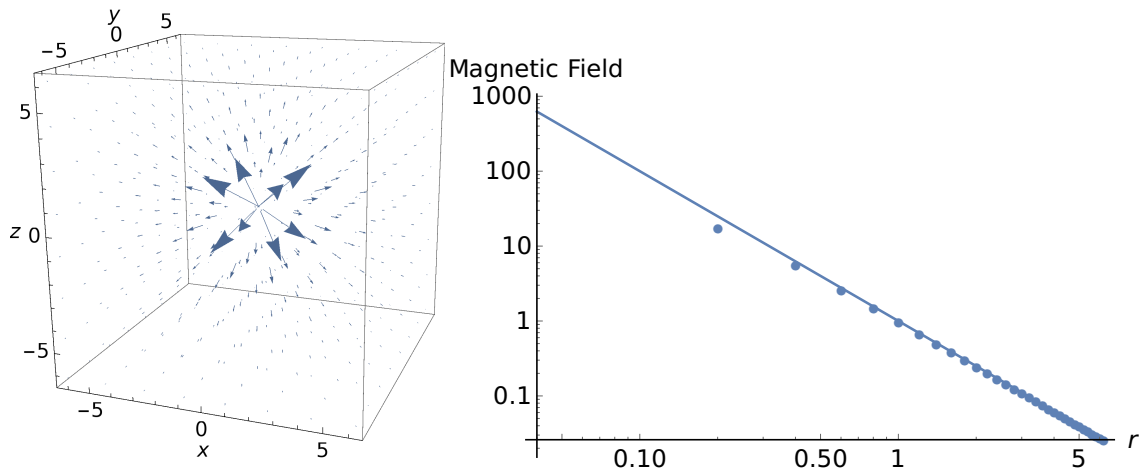

Figure 3.4: A 3D vector plot of the magnetic field of a single monopole. The log-log plot of the magnetic field strength of the monopole vs distance r for $\lambda = 4$. The dots represent the numerical solution and the solid line shows a $1/r^2$ fit.

field do not lie at a lattice point and there are no artificial numerical singularities due to $1/r$ factors when specifying initial conditions as in Eqs. (3.14) and (3.16).

We performed runs with different values of the coupling constant λ, twist γ, and monopole-antimonopole separation $d = 2z_0$. We ran our code for each set of parameters for 1000 iterations and then found the asymptotic value of energy by extrapolating the energy vs. iteration number power law dependence to infinite number of iterations.

We validated our numerical scheme through various means. First, we solve the equations for a single monopole with coupling parameter, $\lambda = 4$, and in the hedgehog gauge on a 64^3 lattice. The magnetic field from this solution was found to precisely fall as $\propto r^{-2}$ away from the location of Higgs zero as shown in the Fig. 3.4. Second, for each set of parameters λ and γ, the energy for the monopole-antimonopole asymptotes to twice the monopole mass at large separation. Third, we found that the energy has a saddle point at twist=π for all values of λ that we had considered. This is consistent with the general arguments by Taubes (1982a) and his analysis for the $\lambda = 0$ case.

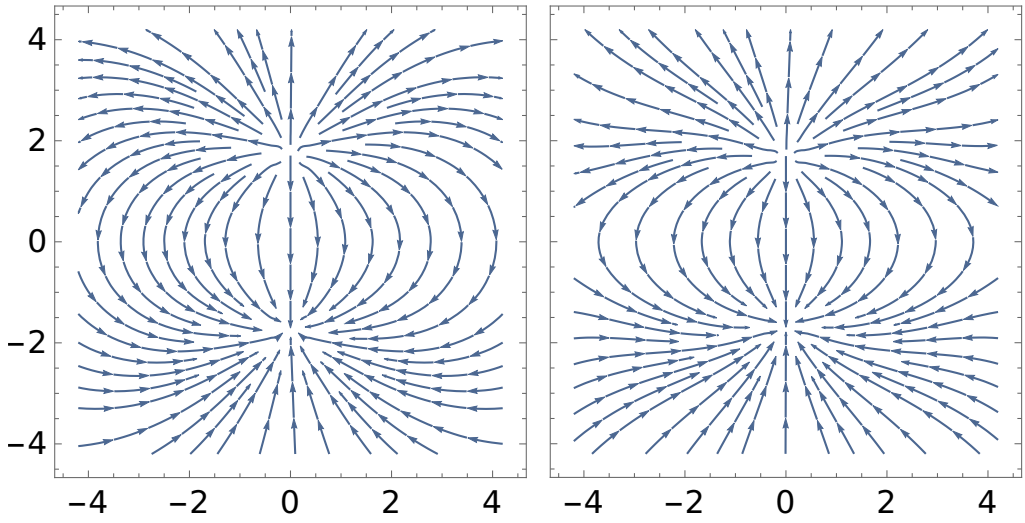

Figure 3.5: Magnetic field lines for $\lambda = 4$, $d = 3.4\,(z_0 = 1.7)$ in the xz-plane in the untwisted case (left) and the maximally twisted case (right).

3.5 Results and Conclusions

We start with results for the magnetic field lines for a monopole-antimonopole pair with and without twist. The results are shown in Fig. 3.5. For the untwisted case and for small separations, when the boundary effects are not significant, we have checked that the magnetic field strength falls off as r^{-3} within our lattice, just as we would expect for a magnetic dipole.

In Fig. 3.6 we show the relaxed energy of the monopole-antimonopole vs. separation for $\lambda = 1$ and for several different twist values. At large separation, the total energy goes to twice the monopole mass, as we expect since the Coulombic interaction dies off. At small separations, the interaction is attractive for small values of twist and repulsive for very large values of twist. The curve for $\gamma = \pi$ (maximum twist) has a minimum at $d \approx 3.4$. This is seen more clearly in Fig. 3.7 where we plot the relaxed energy vs. separation for $\gamma = \pi$ and for several different values of λ. A three-dimensional plot of energy vs. separation and twist would have a saddle point in which the minimum is along the direction of separation and a maximum along the

twist direction. This saddle-point solution which corresponds to a bound state of a monopole and antimonopole is called a "sphaleron" (Klinkhamer and Manton (1984)) and plays an important role in baryon number violating processes in particle physics.

The curves in Fig. 3.6 have qualitative features of $V(d,\gamma)$ in Eq. (3.1) but quantitative differences are apparent when we overlay the analytic expressions and the data as shown in Fig. 3.8. As discussed in the introduction, the differences arise since monopoles are not point particles and monopole-antimonopole can partially annihilate as the separation between them becomes smaller. This annihilation leads to vanishing total energy as the separation goes to zero in the untwisted case unlike the divergent energy predicted by Taubes' potential.

To quantify the energy reduction due to annihilation we write

$$\begin{aligned} E_{\rm data}(d,\gamma) &= A(d,\gamma) E_{\rm Taubes}(d,\gamma) \\ &= A(d,\gamma)\left[2m + V(d,\gamma)\right] , \end{aligned} \tag{3.21}$$

where $E_{\rm data}$ is the energy of the monopole-antimonopole with separation d and twist γ as computed numerically, m is the mass of a single monopole, $2m + V(d,\gamma)$ is the energy as determined using the Taubes formula in Eq. (3.1) valid for point-like monopoles, and $A(d,\gamma)$ is an energy-reduction factor arising due to the finite core size of the monopoles. At large separations $A(d,\gamma)$ goes to one because then the point-like approximation is valid.

We use Eq. (3.21) to determine A as

$$A(d,\gamma) = \frac{E_{\rm data}(d,\gamma)}{E_{\rm Taubes}(d,\gamma)} , \tag{3.22}$$

and we plot $A(d,\gamma)$ for several values of γ in Fig. 3.9. These plots quantify the partial annihilation of monopole and antimonopole due to their finite core sizes. As expected, $A \to 1$ at large separation because the point-like approximation gets better. At small

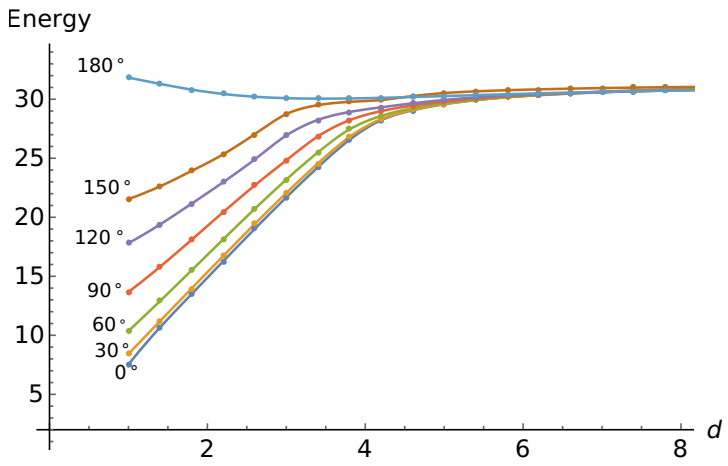

Figure 3.6: Total energy as a function of the monopole-antimonopole separation d for $\lambda = 1$ and twist varying from 0 to π.

separation, the computed energy is smaller than the energy predicted from the Taubes formula due to partial annihilation. From the curves for different γ values, we see that the annihilation is less effective as the twist increases. This too is expected because annihilation can only occur if the fields are aligned in suitable ways while the twist forces them to be misaligned (see Fig. 3.2). In our plot we see that the maximally twisted case has A that is $\sim 10\%$ greater than 1 at short distances. We think this is due to small numerical errors or small corrections to E_{Taubes} that have not been taken into account.

The qualitative behavior of $A(d, \gamma)$ can be written as

$$A(d, \gamma) \sim \tanh\left(\frac{d}{1 + \cos\gamma}\right) . \tag{3.23}$$

In Fig. 3.10 we show energy contours of the untwisted monopole-antimonopole pair and also the sphaleron solution. The total energy of the sphaleron, E_s, depends on the coupling constant λ as shown in Fig. 3.11. The monopole-antimonopole separation within the sphaleron solution, d_s, depends weakly on λ for large values of λ as can be seen in Fig. 3.12. Since some fields fall off very slowly as $\lambda \to 0$, our predicted total energy at such small values of coupling constant could be underestimates by at

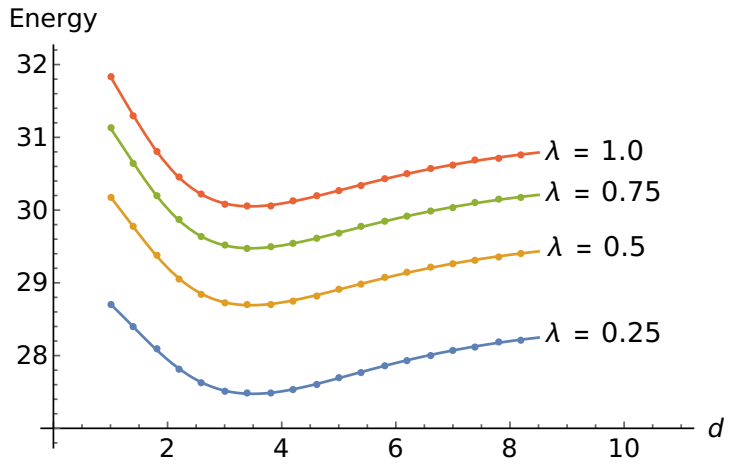

Figure 3.7: Total energy as a function of the monopole-antimonopole separation d for twist $\gamma = \pi$ and λ varying from 0.25 to 1.0. The sphaleron solution is at the minimum in every curve.

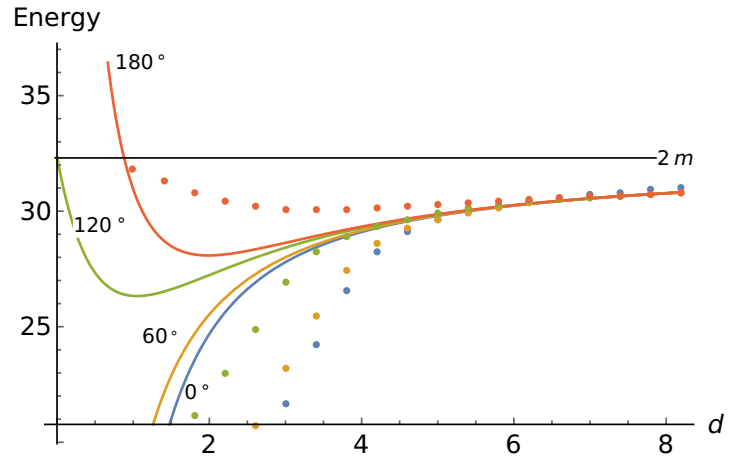

Figure 3.8: Comparison of the data for $\lambda = 1$ and the expression in Eq. (3.1) plus twice the monopole mass (solid curves), demonstrating that the expression is not a good fit to the data.

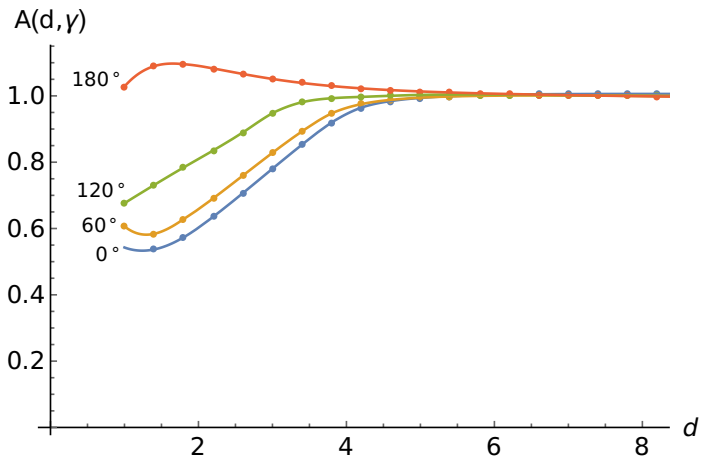

Figure 3.9: The "annihilation" function $A(d, \gamma)$ defined in Eq. (3.22) vs. d for some values of γ.

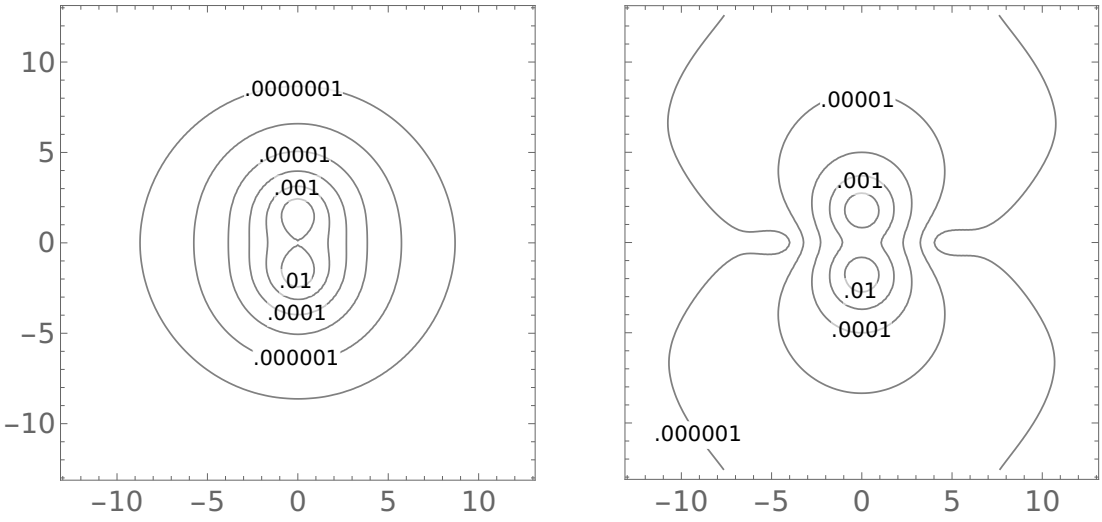

Figure 3.10: Energy density contours for $\lambda = 4$, $d = 3.4$ in the xz-plane in the untwisted case (left) and the maximally twisted case (right).

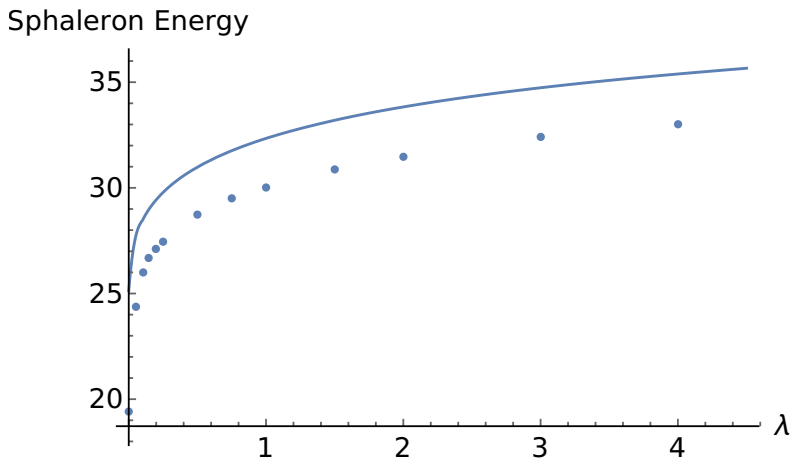

Figure 3.11: Sphaleron energy as a function of λ (dots). The solid curve shows twice the monopole mass vs. λ.

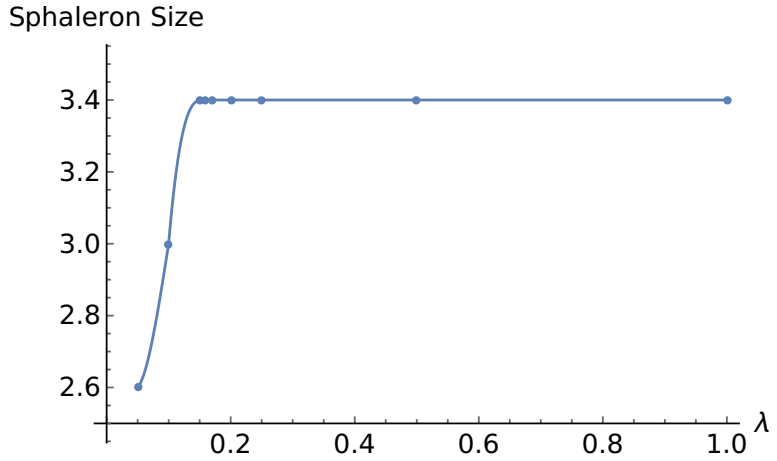

Figure 3.12: Monopole-antimonopole separation in the sphaleron, d_s, vs. λ.

most 20% (we predict this error by comparing the numerically obtained mass of BPS monopole with the theoretical value of 4π).

To conclude, we numerically constructed twisted monopole-antimonopole pairs and mapped out their interaction energy for a range of coupling constants, and explicitly confirmed the arguments made by Taubes (1982a) on the existence of a bound state solution of monopole and antimonopole, also called a sphaleron. In addition, we studied the dependence of the sphaleron energy and size on coupling constant.

Our results are significant also because they provide a method that can be used

to accurately set up initial configurations for dynamical studies such as monopole-antimonopole scattering. Currently, we are involved in another project with the aim to first setup initial conditions for a pair of monopole and antimononopole with angular momentum and then evolve the system to study the backreaction on the orbit due to radiation. The most challenging part in the initial setup of this problem is computing a gauge with periodic boundaries which we have not been able to do successfully yet. Given that monopole-antimonopole pairs have a twist degree of freedom, an interesting question that arises is what are the consequences of this twist on the electric side of the electromagnetic duality, that is, if there is an analogue of twist for bound states of electrically charged particles. Also, we can ask if there are observable signatures associated with annihilation of GUT monopole-antimonopole pairs like high energy cosmic rays (Bhattacharjee and Sigl (1995)). In the electroweak context, our method can be used to set up electroweak dumbbell configurations (Nambu (1977)).

3.6 Inspiralling Monopole-Antimonopole Pair

We are currently also numerically investigating the spectra of massive and massless radiation that emanates upon annihilation of a monopole-antimonopole pair. As the pair separation decreases, they would emit photons, Z bosons, W bosons, and eventually the GUT scale bosons (Bhattacharjee and Sigl (1995)). The main technical challenge in studying an inspiralling pair is that of adding angular momentum to the initial configuration while satisfying periodic boundary conditions. The first step in this process is that we boost the fields by a velocity v along the z axis, that is,

$$\phi^a(x,y,z) \to \widetilde{\phi}^a(t,x,y,z) = \phi^a(\gamma t - \gamma v z, x, y, \gamma z - \gamma v t)\,, \tag{3.24}$$

and using $W_0^a = 0$,

$$\{W_1^a, W_2^a, W_3^a\}(x,y,z) \to \{\widetilde{W}_0^a, \widetilde{W}_1^a, \widetilde{W}_2^a, \widetilde{W}_3^a\}(t,x,y,z) \tag{3.25}$$
$$= \{-\gamma v W_3^a, W_1^a, W_2^a, \gamma W_3^a\}(\gamma t - \gamma v z, x, y, \gamma z - \gamma v t)\,.$$

Since the fields are not in temporal gauge any more, a gauge transformation must be done in order to go back to temporal gauge which is much more suitable for numerical simulations. That is, we must solve for the gauge transformation matrix U as follows,

$$\widetilde{W}_0 \to \overline{W}_0 = U\widetilde{W}_0 U^{-1} + U\partial_0 U^{-1}\,, \tag{3.26}$$

where by setting $\overline{W}_0 = 0$ we get

$$\partial_0 U^{-1} = -\widetilde{W}_0 U^{-1}\,. \tag{3.27}$$

Using the identity $\partial_0(UU^{-1}) = 0$, we can rewrite the last equation as

$$\partial_0 U = U\widetilde{W}_0\,. \tag{3.28}$$

Plugging in the expression for $\widetilde{W}_0$ in eqn. 3.25 gives

$$\Rightarrow \partial_t U(t,x,y,z) = -\gamma v\, U(t,x,y,z)\, W_z(x,y,\gamma z - \gamma v t)\,. \tag{3.29}$$

We only require the matrix transformation U at the time $t = 0$, which means the integration of the last equation is trivial (integration interval is from $t = 0$ to $t = 0$), and gives the solution $U(0,x,y,z) = 1$. This immensely simplifies setting up the initial conditions in temporal gauge after boosting the fields.

Next step in the process is to find another transformation that would make the fields satisfy periodic boundary conditions on our simulation lattice. This step has been a big challenge and we have not fully achieved this goal yet. However, we plan to apply the same approach that we used in our recent study on global string loops (see Chapter 6).

Chapter 4

PRODUCTION OF STRINGS

Our second paper followed from a previous analysis on the creation of magnetic monopoles done by Vachaspati (2016a). We focussed primarily on the production of $U(1)$ gauge strings, where the class of initial conditions we use are motivated by the initial conditions that he proposed.

There are several aspects of the string creation problem that differ from the monopole creation problem. In the latter, once monopole-antimonopole pairs are created with enough energy, they fly apart and survive indefinitely. On the other hand, only closed loops of string can be created. These oscillate, radiate, collapse, and survive only for a finite amount of time. If some of the loops are produced with large angular momentum, they live for longer but eventually decay. A second difference is that the properties of the string network that is produced change with time because the strings interact with each other and intercommute to form smaller loops.

We had introduced the field theory and string solution in the second chapter. In the following sections, we describe our choice of initial conditions and the computational methods used in our analysis.

We will choose initial conditions for our simulations that have trivial winding and no strings. Then even after the particles have scattered and strings are produced, the topological winding around the whole simulation box must vanish. Thus only closed

loops can be produced in a scattering event.

4.1 Initial Conditions

We based the initial conditions for our simulations on those used for monopole-antimonopole production (Vachaspati (2016a)). We adopted the temporal gauge for all our simulations, that is $A_0 = 0$, and construct circularly polarized gauge wavepacket configurations (not solutions) that propagate along the $\pm z-$axis. Consider the ansatz below for a wavepacket propagating in the $-z$ direction,

$$\mathcal{A}_x = \partial_y f_1(\omega f_2 - \partial_z f_2)\cos(\omega(t+z-z_0)) \tag{4.1}$$

$$\mathcal{A}_y = \partial_x f_1(\omega f_2 + \partial_z f_2)\sin(\omega(t+z-z_0)) \tag{4.2}$$

$$\mathcal{A}_z = \partial_x\partial_y f_1 f_2[\cos(\omega(t+z-z_0)) - \sin(\omega(t+z-z_0))] \tag{4.3}$$

where $f_1 = f_1(x,y)$, $f_2 = f_2(t+z-z_0)$ will be specified below, and z_0 determines the initial ($t=0$) location of the wavepacket along the $z-$axis. Now the initial conditions for the gauge fields and their time derivatives are,

$$A_i(t=0,\mathbf{x}) = \mathcal{A}_i(t=0,\mathbf{x}), \tag{4.4}$$

$$\partial_t A_i(t=0,\mathbf{x}) = [\partial_t \mathcal{A}_i(t,\mathbf{x})]_{t=0} \tag{4.5}$$

This form for the gauge fields satisfies $\nabla\cdot\boldsymbol{A} = 0$ which will be useful later when we discuss Gauss constraints.

We also constructed a wavepacket traveling in the $+z$ direction in a similar manner. To do this, we write the formulae in terms of $f_3(t-(z+z_0))$:

$$\mathcal{A}'_x = \partial_y f_1(-\omega' f_3 - \partial_z f_3)\cos(\omega'(t-z-z_0) \tag{4.6}$$

$$\mathcal{A}'_y = -\partial_x f_1(\omega' f_3 - \partial_z f_3)\sin(\omega'(t-z-z_0)) \tag{4.7}$$

$$\mathcal{A}'_z = \partial_x\partial_y f_1 f_3(\cos(\omega'(t-z-z_0)) - \sin(\omega'(t-z-z_0)) \tag{4.8}$$

And these can be used to construct initial conditions for a wavepacket that propagates in the $+z$ direction as above.

We chose profile functions in a manner that localizes the gauge wavepacket in all directions;

$$f_1(x,y) = a\,\exp\left[-\frac{x^2+y^2}{2w^2}\right], \tag{4.9}$$

$$f_2(t+z-z_0) = \exp\left[-\frac{(t+z-z_0)^2}{2w^2}\right], \tag{4.10}$$

$$f_3(t-z-z_0)) = \exp\left[-\frac{(t-z-z_0)^2}{2w^2}\right], \tag{4.11}$$

where a is the amplitude and w is the width of the wavepacket.

The initial conditions for the scalar field are "trivial",

$$\phi(t=0,\mathbf{x}) = \eta, \quad [\partial_t\phi(t,\mathbf{x})]_{t=0} = 0\,. \tag{4.12}$$

The free parameters in the initial conditions are z_0, a, w, ω and ω'. For our simulations, we rescaled these parameters as follows:

$$z_0 = \frac{\bar{z}_0}{\eta},\; a = \frac{\bar{a}}{\eta},\; w = \frac{\bar{w}}{\eta},\; \omega = \bar{\omega}\eta,\; \omega' = \bar{\omega}'\eta\,. \tag{4.13}$$

The dimensionless parameters $\bar{z}_0$, $\bar{a}$, $\bar{w}$, $\bar{\omega}$, and $\bar{\omega}'$ above are varied in our code. In addition, the Abelian Higgs model has the parameters e, λ and η. However, by field and coordinate rescalings, there is only one model parameter given by the ratio of scalar and vector masses, $\beta = m_S^2/m_V^2 = 2\lambda/e^2$.

4.2 Computational Techniques

Following the numerical relativity based approach that Vachaspati (2016a) developed, we introduced a new dynamical variable $\Gamma = \partial_i A_i$. Then the field variables are:

ϕ, A_i and Γ, altogether 6 functions. The equations of motion for these variables are,

$$\partial_t^2 \phi_a = \nabla^2 \phi_a - e^2 A_i A_i \phi_a - 2e\epsilon_{ab}\partial_i \phi_b A_i - e\epsilon_{ab}\phi_b \Gamma \,, \\ - \lambda(\phi_b \phi_b - \eta^2)\phi_a \tag{4.14}$$

$$\partial_t F_{0i} = \nabla^2 A_i - \partial_i \Gamma + e(\epsilon_{ab}\phi_a \partial_i \phi_b + eA_i \phi_a \phi_a) \,, \tag{4.15}$$

$$\partial_t \Gamma = \partial_i F_{0i} - g_p^2 [\partial_i F_{0i} + e\epsilon_{ab}\phi_a \partial_t \phi_b] \,, \tag{4.16}$$

where $a = 1, 2$, ϵ_{ab} is the Levi-Civita tensor with $\epsilon_{12} = 1$, $F_{0i} = \partial_t A_i$ in the temporal gauge, and g_p^2 is a new parameter introduced for numerical stability. The idea is that the square bracket in Eq. (4.16) vanishes in the continuum because of the Gauss constraints $\nabla \cdot \mathbf{E} = \rho$ where ρ is the charge density. However, the square bracket may not vanish upon discretization. By writing the equations in the above form with the auxiliary function Γ, we obtained improved numerical stability as is also seen in Numerical Relativity (Baumgarte and Shapiro (2010)). The value of the parameter g_p^2 is chosen by numerical experimentation; we have set $g_p^2 = 0.75$ in our simulations. The initial conditions for the auxiliary function Γ follow from the choice of initial conditions for the gauge field,

$$\Gamma(t = 0, \mathbf{x}) = 0 \,. \tag{4.17}$$

For our analysis, we discretized these equations on a 256^3 lattice with lattice spacing $\Delta x = 0.05$ and time step size $\Delta t = \Delta x/4$. The difference equations were solved using the explicit Crank-Nicholson method with two iterations. To reduce computation times, we parallelized our numerical code. As a check of our evolution code, we found that the total energy inside the box is conserved to within 1% during the entire evolution period.

In addition to the evolution of equations, we developed a tracking code which detects strings and calculates the number of loops that are present in the simulation

domain at any given time. The program calculates the phase winding as defined in Eq. (2.19) on every plaquette of the lattice. A non-zero winding on a plaquette implies that a string passes through the plaquette and enters/exits the corresponding cells. The program then connects the strings and records the properties of the loops.

The string tracking algorithm is the same as used in earlier work (Vachaspati and Vilenkin (1984); Pogosian and Vachaspati (1998)) but with one subtlety. In calculating the winding as in Eq. (2.19), we have to find the discretized value of $d\theta$ along the links of the lattice. Generally one uses the "geodesic rule" and the phase difference between lattice sites i and $i+1$ is

$$d\theta \to \Delta\theta \equiv \theta_{i+1} - \theta_i + 2\pi k\,, \tag{4.18}$$

where $k = 0, \pm 1$ is chosen to minimize $|\Delta\theta|$. However, this rule ignores the case when $|\Delta\theta| = \pi$. The justification in earlier works has been that this possibility is of zero measure. In our case, however, this situation arises quite frequently. The reason can be seen from the equations of motion and the initial conditions. We start out with $\phi_1 = \eta$ and $\phi_2 = 0$ *i.e.* $\theta = 0$ throughout the lattice. The equations of motion are such that they tend to preserve $\phi_2 = 0$, and all the non-trivial dynamics is in the ϕ_1 variable, at least at early times. Now ϕ_1 can become negative. When ϕ_1 differs in sign at neighboring lattice sites, this gives a phase difference of exactly $\pm\pi$ and the geodesic rule is ambiguous. In evaluating the winding number, we chose $+\pi$ or $-\pi$ with equal probability.

4.3 Results

As we have discussed above, the problem contains 1 model parameter, namely β, and 5 initial condition parameters. We will fix some of these parameters and scan

over a range of a few parameters. We set

$$\bar{z_0} = 1.8, \quad \bar{w} = 0.6, \quad \bar{\omega}' = \bar{\omega}\,. \tag{4.19}$$

We have explored,

$$\beta \in [0.08, 8.0], \quad \bar{a} \in [0.6, 7.0], \quad \bar{\omega} \in [0.2, 8.0]\,. \tag{4.20}$$

We did not see any qualitative changes as we varied β (see below) and so for most of our runs we set $\beta = 1$, equivalently $e = 0.5$, $\lambda = 0.125$. We also chose $\eta = 1$ and this sets the length scale in the simulation.

From our initial runs, we found that energy is condensed into strings even from a single wavepacket, *i.e.* without scattering two gauge wavepackets. We will call this "prompt string production" and it is reminiscent of the discovery made by Hindmarsh and Rajantie (2000b) that strings may be formed due to purely gauge field fluctuations during a phase transition. In the next subsection, we will explore prompt string production and find that there are regions of parameter space where prompt production does not occur. We will then move on to explore this region of parameter space and find a sub-region where strings are produced when wavepackets collide.

4.3.1 Prompt String Production

For the single pulse case, after fixing the parameters of the theory, we managed to analytically find expression for total energy in the simulation domain for the wavepacket profiles shown in the previous section. It is as follows,

$$E_{\text{Single}} = \frac{\bar{a}^2 \pi^{\frac{3}{2}} \eta \left(9 + 10\bar{w}^2\bar{\omega}^2 + 4\bar{w}^4\bar{\omega}^4 + 2e^2(\bar{w}^2 + \bar{w}^4\bar{\omega}^2)\right)}{8\bar{w}^3}\,. \tag{4.21}$$

With this expression, we can trade one of the parameters for the total energy.

In Fig. 4.1 we show the prompt production of strings at various times during the evolution. In the first frame, there is energy density of the wavepacket but no

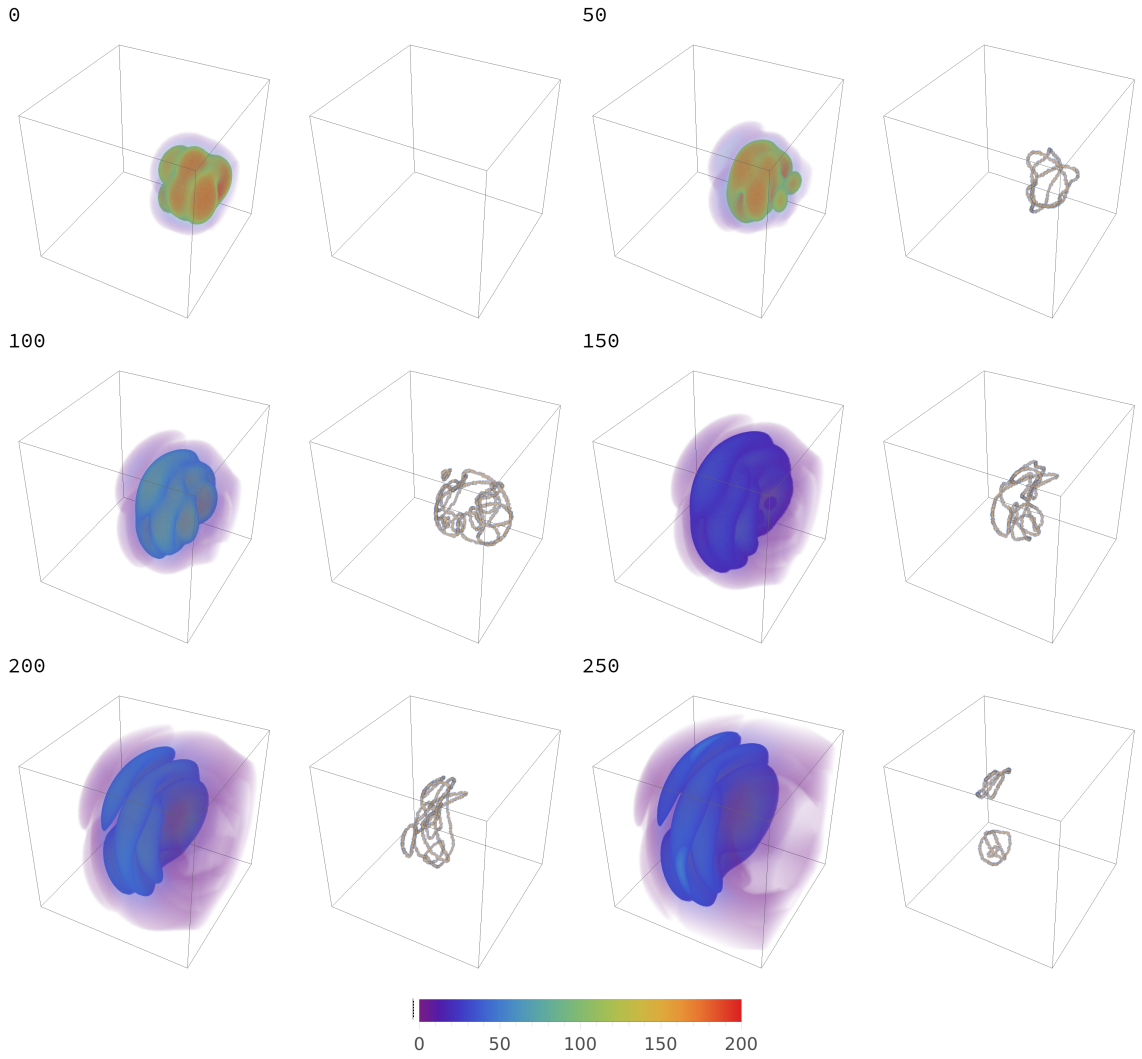

Figure 4.1: Total energy density (boxes on the left) and winding (boxes on the right) at different time steps for the case of one pulse for $\bar{a} = 6.215$, $\bar{\omega} = 2.0$, $\lambda = 0.125$, and $E_{\text{Single}} = 4000$. The 116^3 boxes shown here are smaller than the full lattice (256^3).

strings. Some time steps later, the scalar field has adjusted to the gauge wavepacket and strings, as detected by topological winding, are produced. As the system evolves further, the dense network of strings chops itself up and decays.

We examined prompt production for several different values of the model parameter λ (equivalently β since we fix $e = 0.5$). Fig. 4.2 shows how the length in strings – evaluated by counting the plaquettes that contain non-trivial topological winding

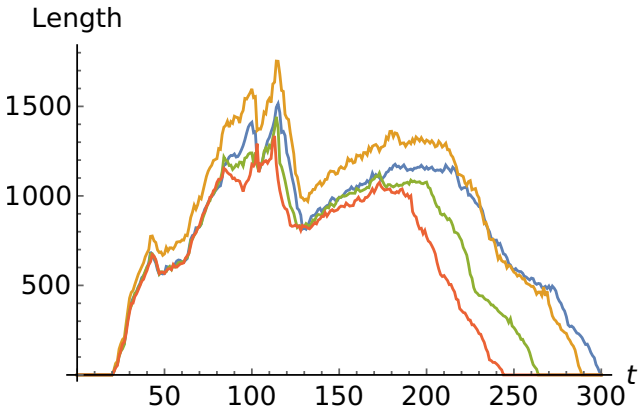

Figure 4.2: Total length of strings (in units of number of lattice points) as a function of time(-steps) for $\lambda = 0.01$ (blue), $\lambda = 0.125$ (orange), $\lambda = 0.50$ (green), and $\lambda = 1.0$ (red). All the other kinematic parameters are kept fixed with $\bar{a} = 6.215$ and $\bar{\omega} = 2.0$.

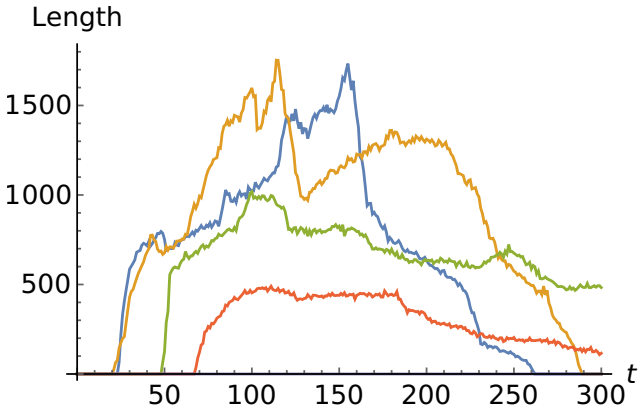

Figure 4.3: Total length of strings (in units of number of lattice points) as a function of time(-steps) for $\bar{\omega} = 0.1$ (blue), $\bar{\omega} = 2.0$ (orange), $\bar{\omega} = 4.0$ (green), $\bar{\omega} = 6.0$ (red), $\bar{\omega} = 8.0$ (no strings), and $\lambda = 0.125$. Total energy for all the runs is kept fixed at, $E_{\text{Single}} = 4000$, by adjusting $\bar{a}$ suitably according to Eq. (4.21).

– changes with time. The figure shows that the outcome is not very sensitive to the value of λ and hence we set $\lambda = 0.125$ ($\beta = 1$) in the runs described below.

In contrast, as seen in Fig. 4.3, the prompt production of strings depends sensitively on the parameter $\bar{\omega}$. The general trend is that less length is produced for larger $\bar{\omega}$ but the strings that are produced survive for a longer time. This can happen if larger $\bar{\omega}$ leads to larger loops or to loops with higher angular momentum.

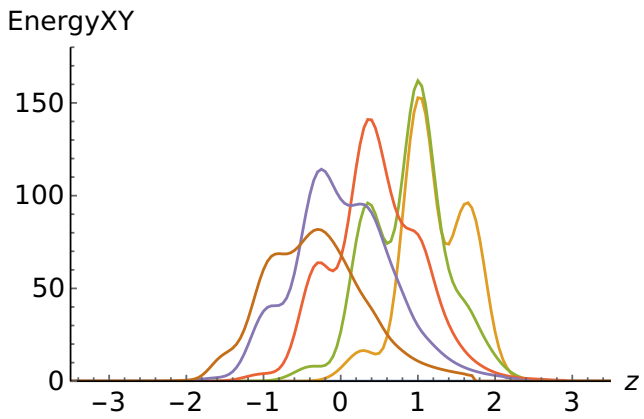

Figure 4.4: Energy in strings in $xy-$planes as a function of z at time steps $t = 0$ (no strings), $t = 50$ (orange, right-most curve), $t = 100$ (green), $t = 150$ (red), $t = 200$ (blue), and $t = 250$ (brown, left-most curve), during the simulation for $\bar{a} = 6.215$, $\bar{\omega} = 2.0$, $\lambda = 0.125$, and $E_{\text{Single}} = 4000$. Following prompt string production, the string network moves to the left and decays.

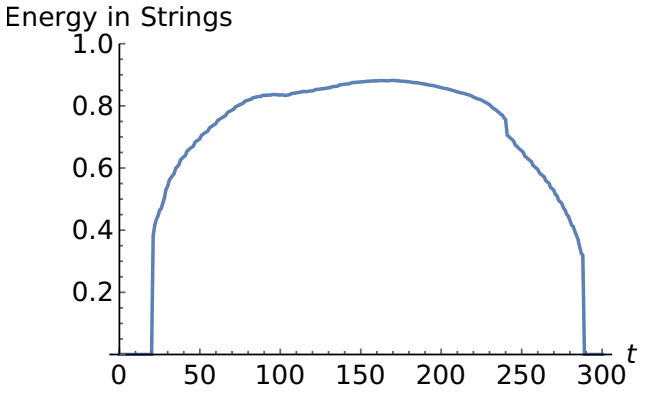

Figure 4.5: Energy in strings as a fraction of total energy versus time(-steps) for $\bar{a} = 6.215$, $\bar{\omega} = 2.0$, $\lambda = 0.125$, and $E_{\text{Single}} = 4000$.

In Fig. 4.4 we plot the energy density integrated over $\bar{x}$ and $\bar{y}$ coordinates, as a function of $\bar{z}$. Prompt string production occurs at the initial location of the wavepacket ($\bar{z}_0 = 1.8$ or 36 lattice spacings away from the center of the lattice). Then the string cluster moves towards the left and also decays.

We calculated the length of strings at any given time by counting the number of plaquettes with non-trivial winding. We also estimated the energy in the string network by adding up the field energies in all the cells within m_S^{-1} or m_V^{-1} (whichever

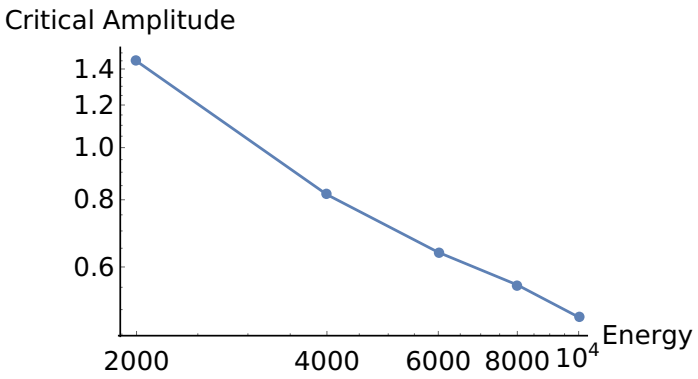

Figure 4.6: Critical amplitude $\bar{a}$ as we change total input energy, E_{Single}, for the single pulse case with $\lambda = 0.125$. Strings are only produced above the curve.

is larger) of the string network. However, the plot in Fig. 4.5 of the energy vs. time shows reasonable correspondence with the length versus time plot in Fig. 4.3 for $\bar{\omega} = 2.0$, indicating that the strings do not have significant kinetic energy at formation.

As expected, greater initial energy produces more strings. However, our analysis indicates some subtleties in the process of string production. From Eq. (4.21), it can be seen that, for fixed energy, amplitude becomes smaller as we increase the frequency and vice-versa. (The wavepacket width $\bar{w}$ is fixed in all our runs.) After experimenting with different values of amplitude and frequency at fixed energy, we noticed that there is a minimum/critical amplitude below which we do not produce any strings, as seen in Fig. 4.6). The parameter space under the critical curve, for which strings are not produced, gets smaller as the energy increases. In the opposite limit of small $\bar{\omega}$ (large amplitude), we see that the total length of strings is far greater (also seen in Fig. 4.3). The physical origin of this behavior is not clear. One expectation is that more strings are produced if there is higher energy density (for the same total energy). However, upon plotting the maximum energy density in our simulation box over the duration of the run with respect to frequency (for fixed total energy equal to 4000), we find noisy behavior with an overall increasing trend (see Fig. 4.7). This is counterintuitive,

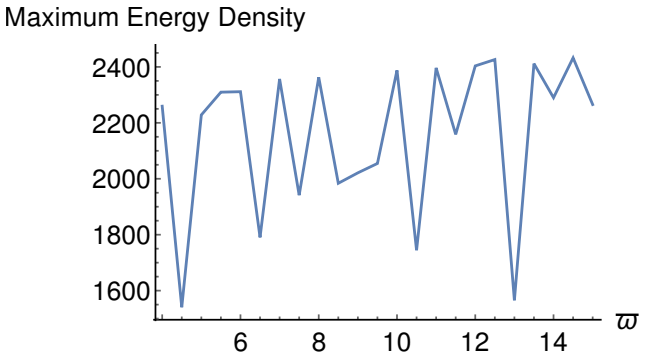

Figure 4.7: Maximum energy density as a function of frequency $\bar{\omega}$ in the initial wavepackets for $\lambda = 0.125$ and total energy of 4000 in the box. The critical frequency above which no strings are produced here is 7.5 (corresponding to $\bar{a} = 0.817$).

since no strings are produced above the critical value of $\bar{\omega} = 7.5$ (corresponding to the critical amplitude $\bar{a} = 0.817$ as seen in Fig. 4.6). This indicates that energy density alone may not determine string production and is reminiscent of the chaotic behavior seen in kink production in 1+1 dimensions (Dutta *et al.* (2008); Romanczukiewicz and Shnir (2010)).

4.3.2 Wavepacket Collisions

We now consider the case when two wavepackets collide. The parameters are chosen so that there is no prompt string production. However, strings are produced when the wavepackets collide. So now we have two wavepackets in the initial conditions that are headed towards a collision. The initial energy is

$$\begin{aligned} E_{\text{Double}} &= 2E_{\text{Single}} + \frac{\pi^{3/2}\bar{a}^2\eta}{4\bar{w}^7} e^{-\bar{z}_0^2/\bar{w}^2} \Big[-18\bar{w}^2\bar{z}_0^2 + 4\bar{z}_0^4 \\ &\quad + 2\bar{w}^8\bar{\omega}^2(e^2 + 2\bar{\omega}^2) + 2\bar{w}^6(e^2 + 5\bar{\omega}^2) \\ &\quad + \bar{w}^4(9 - 2e^2\bar{z}_0^2 - 8\bar{z}_0^2\bar{\omega}^2)\cos(2\bar{z}_0\bar{\omega}) \\ &\quad - 8\bar{w}^2\bar{z}_0\omega(2\bar{w}^2 - \bar{z}_0^2 + \bar{w}^4\bar{\omega}^2)\sin(2\bar{z}_0\bar{\omega}) \Big] . \end{aligned} \tag{4.22}$$

We again used Eq. (4.21) for fixing kinematic parameters. For the simulation, we

chose $\bar{a} = 0.578$ and $\bar{\omega} = 9.0$ for the individual wavepackets. With this choice prompt production of strings does not occur, that is, the parameters lie below the critical curve for the single pulse case shown in Fig. 4.6.

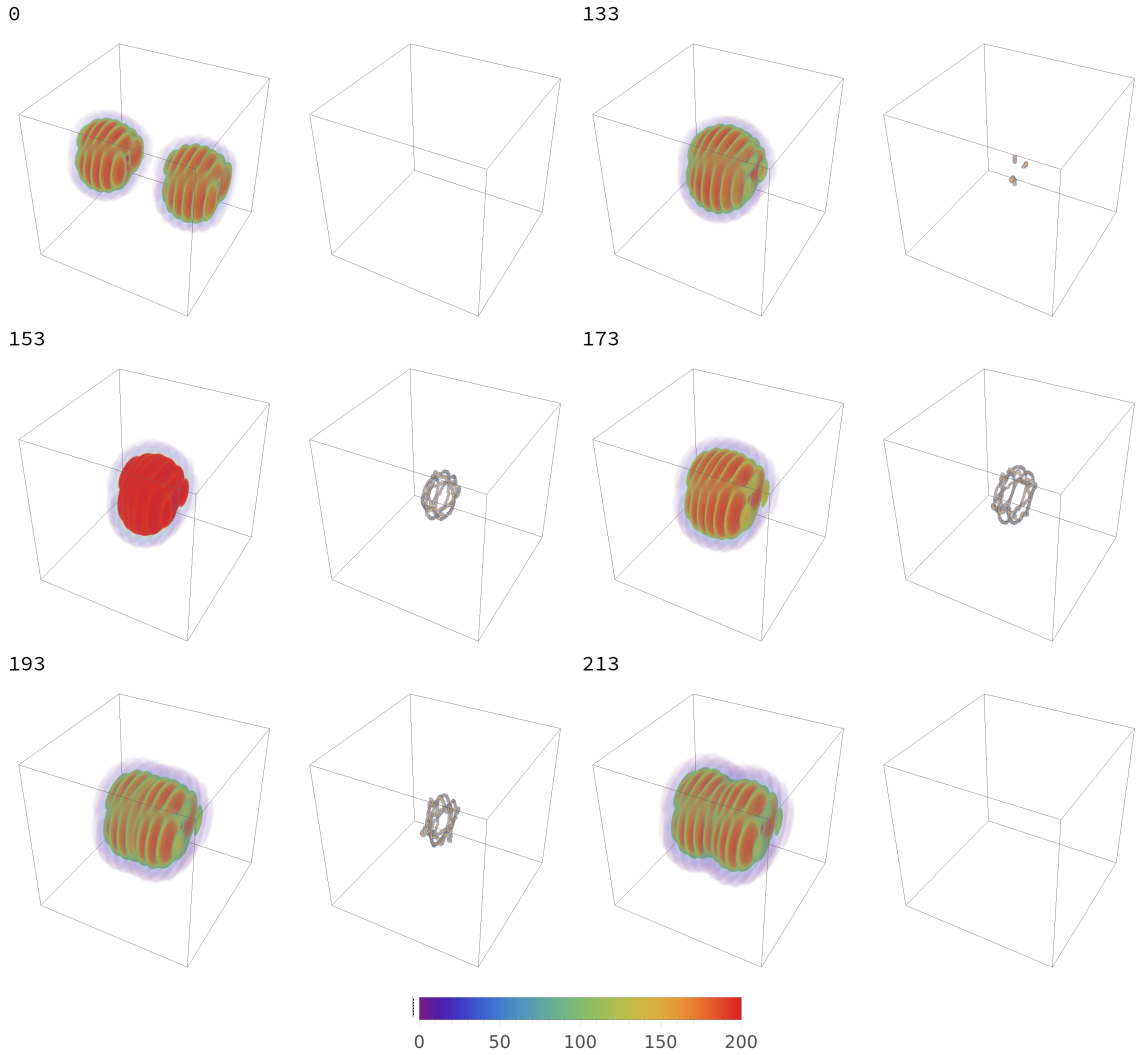

Figure 4.8: Total energy density (boxes on the left) and winding (boxes on the right) at different time steps for the case of two collinear pulses for $\bar{a} = 0.578$, $\bar{\omega} = 9.0$, $\lambda = 0.125$, and $E_{\text{Double}} \approx 8000$. The strings are first produced at time step 133 in our simulation, and therefore we have not shown plots for intermediate time steps. The 116^3 boxes shown here are smaller than the full lattice (256^3).

Fig. 4.8 shows the evolution of the wavepackets and string formation after collision. Very few short-lived strings are produced even though the total input energy is much

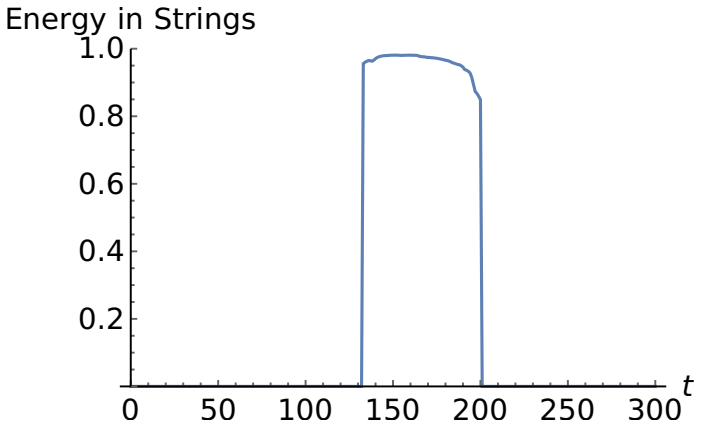

Figure 4.9: Energy in strings as a fraction of total energy versus time for $\bar{a} = 0.578$, $\bar{\omega} = 9.0$, $\lambda = 0.125$, and $E_{\text{Double}} \approx 8000$.

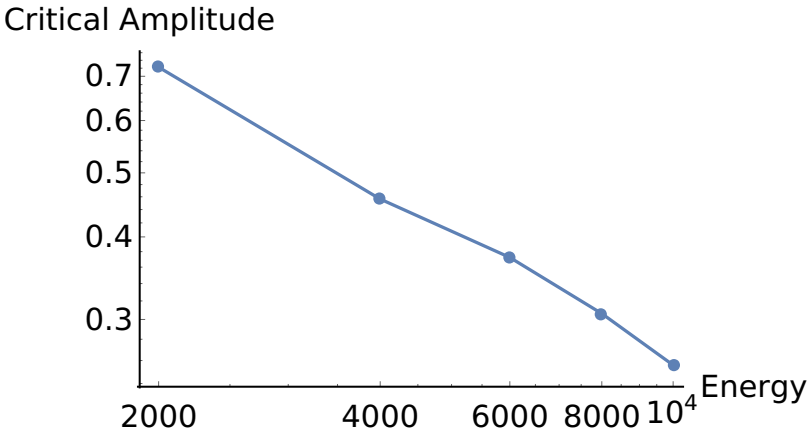

Figure 4.10: Critical amplitude $\bar{a}$ as we change total input energy, E_{Double}, for the case of colliding wavepackets for $\lambda = 0.125$. Strings are only produced above the curve.

higher (≈ 8000) compared to the single pulse run presented in the previous subsection. The fractional energy in strings as a function of time is shown in Fig. 4.9. By scanning over different amplitudes, $\bar{a}$, for the same total energy, we found the critical curve for string formation when wavepackets collide. The critical curve is plotted in Fig. 4.10.

4.4 Conclusions

We explored the formation of $U(1)$ gauge strings due to wavepackets of of gauge fields in two settings: (i) the prompt formation of strings from gauge fields, and (ii) the formation of strings when gauge wavepackets collide. We restricted our attention to a class of wavepackets with certain parameters, and found critical curves in parameter space that demarcate string formation regions. These critical curves show that it is easier to produce strings with higher energy wavepackets (see Fig. 4.6 and 4.10). However, we did not found a general pattern beyond this simple conclusion. The reason may lie in the chaotic behavior observed in previous studies of kink production in $1+1$ dimensions (Dutta *et al.* (2008); Romanczukiewicz and Shnir (2010)).

It is also interesting to contrast string production with magnetic monopole production. Unlike the case of magnetic monopoles, the string loops that are formed are short-lived as they collapse and produce radiation. The loops may live longer if we could find initial conditions that provide them with greater angular momentum but these too will not live indefinitely. On the other hand, once a magnetic monopole and antimonopole pair are produced with sufficient velocity, they will move apart and survive indefinitely. Furthermore, magnetic monopoles are localized objects and so the colliding wavpackets need not be very extended. For strings, the wavepackets have to extend over a region that is the size of the string loop that is to be produced, and only relatively small loops can be produced. In these respects it appears that magnetic monopoles are easier to produce than strings.

The flip side is that we know systems that contain gauge strings while the existence of magnetic monopoles is still speculative. Gauge strings are known to exist in superconductors and, in that setting, our gauge field wavepackets correspond to photon wavepackets. This suggests that by shining light on superconductors we could

produce strings within the superconductor. However, a realistic superconductor is described by a different set of equations that take into account the dependence of the model parameters on the temperature (Kennes and Millis (2017)). It will be interesting to adapt our analysis to study string production in superconductors.

Chapter 5

DECAY OF COSMIC STRING LOOPS

In one of our recent projects (Matsunami *et al.* (2019)), for the first time, we directly examined the decay of a cosmic string loop to particle radiation in the Abelian-Higgs model by simulating loop formation followed by evolution in full field theory. Previous studies of the particle radiation from cosmic strings included analytical estimates (Vachaspati *et al.* (1984)), some based on effective couplings of Nambu-Goto strings to other fields (Srednicki and Theisen (1987); Brandenberger (1987)), field theory simulations of standing waves, kinks, and cusps on long strings (Olum and Blanco-Pillado (1999, 2000)) and simulations of strings with small oscillations (Martins *et al.* (2004); Hindmarsh *et al.* (2017)). The focus on a single loop is to be contrasted with the very large field theory simulations of an entire network of strings in an expanding spacetime (Hindmarsh *et al.* (2009b, 2017)).

We found that string loops emit particle radiation mainly due to features on the strings known as kinks and cusps (Vilenkin and Shellard (2000)). Kinks are non-differentiable sharp corners on strings that move with the speed of light and cusps are points at which a string momentarily moves with the speed of light. Basically, curves along a string can be described using one parameter ζ, and tangents to these curves change discontinuously on kinks and cusps represent singular points on these curves. The half-life of a loop due to particle radiation is proportional to L^p, where L is the length of the loop and $p \approx 2$ for the loops we have considered. On the other hand, the loop half-life due to gravitational radiation is known to be proportional to L. Thus, there is a crossover from particle-decay to gravitational-decay roughly given by $L_* \sim w/G\mu$ where $w \sim \mu^{-1/2}$ is the width of the string. For $L < L_*$, loops decay

by particle emission, while for $L > L_*$ gravitational emission dominates. We discuss caveats and the implications of this result in more detail below, along with the values of p that might arise for loops other than those we have directly simulated.

5.1 Model

We again considered the Abelian-Higgs field theory with a complex scalar field, $\phi = \phi_1 + i\phi_2$, and a $U(1)$ gauge field, A_μ. We work in the temporal gauge, $A_0 = 0$, and the field equations of motion are

$$\partial_t^2 \phi_a = \nabla^2 \phi_a - e^2 A_i A_i \phi_a - 2e\epsilon_{ab}\partial_i \phi_b A_i - e\epsilon_{ab}\phi_b \Gamma - \lambda(\phi_b \phi_b - \eta^2)\phi_a \,, \tag{5.1}$$

$$\partial_t F_{0i} = \nabla^2 A_i - \partial_i \Gamma + e(\epsilon_{ab}\phi_a \partial_i \phi_b + eA_i \phi_a \phi_a) \,, \tag{5.2}$$

$$\partial_t \Gamma = \partial_i F_{0i} - g_p^2[\partial_i F_{0i} + e\epsilon_{ab}\phi_a \partial_t \phi_b] \,, \tag{5.3}$$

where $a = 1, 2$, ϵ_{ab} is the Levi-Civita tensor with $\epsilon_{12} = 1$, $F_{0i} = \partial_t A_i$ in the temporal gauge, λ and e are coupling constants, $\Gamma \equiv \partial_i A_i$, and g_p^2 is a parameter introduced for numerical stability (Vachaspati (2016b)). The solution for a topologically stable straight string along the $z-$axis is (Nielsen and Olesen (1973))

$$\phi = \eta f(r) e^{i\theta}, \quad A_i = v(r)\epsilon_{ij}\frac{x^j}{r^2} \quad (i, j = 1, 2) \,, \tag{5.4}$$

where $r = \sqrt{x^2 + y^2}$, $\theta = \tan^{-1}(y/x)$, and $f(r)$ and $v(r)$ are profile functions that vanish at the origin and asymptote to 1, respectively. The string energy per unit length (also its tension) is given by $\mu = \pi\eta^2 F(\beta)$ where $\beta \equiv 2\lambda/e^2$ and F is a numerically determined function such that $F(1) = 1$. We only considered $\beta = 1$ corresponding to the Bogomol'nyi-Prasad-Sommerfield (BPS) limit (Bogomolny (1976); Prasad and Sommerfield (1975)) where $\mu = \pi\eta^2$ and the scalar mass, $m_S = \sqrt{2\lambda}\eta$, equals the vector mass, $m_V = e\eta$.

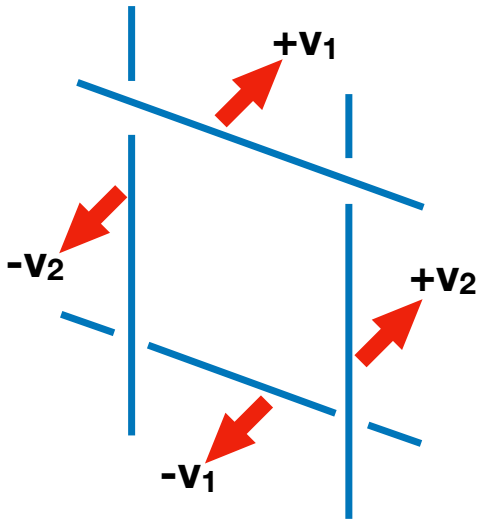

Figure 5.1: Schematic representation of the initial configuration. Four straight strings are set up with velocities as shown. The strings intersect and reconnect to produce a central loop and also a second "outer" loop because of the periodic boundary conditions. These loops then oscillate and shrink without interacting with each other. By choosing the spacing of the initial strings, we can produce loops of different sizes.

5.2 Initial Conditions and Numerical Method

Our aim was to produce a loop as might be produced in a cosmological setting and then to evolve it. For this purpose, we set up initial conditions with four straight strings that are moving with velocities $\pm\mathbf{v_1}$ and $\pm\mathbf{v_2}$ as shown schematically in Fig. 5.1. The four strings then collide to form a loop with a stationary center of mass and a non-zero angular momentum. The latter is essential to prevent the loop from simply collapsing to a double line. Preparing this initial configuration starts with taking the string solution of Eq. (5.4) oriented along a given direction, boosting it to a suitable velocity, and gauge transforming the boosted solution back in to the temporal gauge. Then the four string solutions have to be patched together in a simulation box with periodic boundaries. We describe all these steps in more detail next.

First, we numerically find a solution for a static, infinite, straight string by substituting the Nielsen-Olesen ansatz (Eq. (5.4)) into the equations of motion and solving for the profile functions $f(r)$ and $v(r)$ using the relaxation method. We then use cubic spline interpolation to obtain smooth functions $f(r)$ and $v(r)$ and their derivatives.

To build a cosmic string loop we consider a string-antistring pair along the z-direction and another along the x-direction in a simulation box with periodic boundary conditions (PBC). We then Lorentz boost the strings and antistrings so that they are moving towards each other as shown in the Fig. 5.1. Since the evolution equations (Eq. (5.3)) are in the temporal gauge, we must gauge transform the boosted string solutions to set the temporal component of the gauge field to zero. Namely, we find a gauge transform $U = e^{ie\xi}$ such that

$$A_0 = \bar{A}_0 + \frac{i}{e} U \partial_t U^* = \bar{A}_0 + \partial_t \xi = 0 \,, \tag{5.5}$$

$$A_i = \bar{A}_i + \frac{i}{e} U \partial_i U^* = \bar{A}_i + \partial_i \xi \,, \tag{5.6}$$

where A_μ is in the temporal gauge and $\bar{A}_\mu$ is the field after the Lorentz boost.

From Eq. (5.5), we have $\partial_t \xi = -\bar{A}_0$ and ξ can be evaluated as

$$\xi = \int_0^t d\tau \bar{A}_0 \,. \tag{5.7}$$

At initial time $t = 0$, this gives $\xi = 0$. Similarly $\partial_i \xi|_{t=0} = 0$. Hence, at the initial time, we have

$$A_0 = 0 \,, \tag{5.8}$$

$$A_i = \bar{A}_i + \partial_i \xi|_{t=0} = \bar{A}_i \,, \tag{5.9}$$

where all functions are evaluated at $t = 0$. Note that the initial value of the scalar field is unaffected by the gauge transformation since $\exp(ie\xi) = 1$ when $\xi = 0$.

To solve the equations of motion we also need $\partial_t A_\mu$ and $\partial_t \phi$ at the initial time. We have

$$\partial_t A_\mu|_{t=0} = \partial_t \bar{A}_\mu + \partial_t \partial_\mu \xi = \partial_t \bar{A}_\mu - \partial_\mu \bar{A}_0 \,, \tag{5.10}$$

$$\partial_t \phi|_{t=0} = \partial_t \bar{\phi} - ie\bar{A}_0 \bar{\phi} \,, \tag{5.11}$$

where all functions are evaluated at $t = 0$.

To combine the string and antistring solutions, we take the ansatz given by Vilenkin and Shellard (2000),

$$\phi_{s\bar{s}} = \frac{\phi_s \phi_{\bar{s}}}{\eta} = \frac{|\phi_s||\phi_{\bar{s}}|}{\eta} e^{i(\theta_s - \theta_{\bar{s}})} \,, \tag{5.12}$$

$$A_{s\bar{s}} = A_s - A_{\bar{s}} \,. \tag{5.13}$$

To be consistent with the PBC, the phase of $\phi_{s\bar{s}}$ must approach zero at the boundaries of the box. While in Eq. (5.13) the phase approaches zero asymptotically at infinity, it does not do so in a finite simulation box. Thus, we modified the ansatz to make the phase approach zero faster:

$$\phi_{s\bar{s},\mathrm{mod}} = \frac{|\phi_s||\phi_{\bar{s}}|}{\eta} e^{i(\theta_s - \theta_{\bar{s}})[1 - \tanh(\omega(\rho - \mathrm{L}/2))]/2} \,,$$

where ω, taken to be 0.5, is a parameter that determines how quickly the phase approaches to 0 at the boundaries, and L is the size of the box. Finally, the scalar and gauge fields of the two sets of a parallel string-antistring pair are given as

$$\phi = \frac{\phi_{s\bar{s},1} \phi_{s\bar{s},2}}{\eta} \,, \tag{5.14}$$

$$A = A_{s\bar{s},1} + A_{s\bar{s},2} \,, \tag{5.15}$$

where $\phi_{s\bar{s},1}, A_{s\bar{s},1}$ and $\phi_{s\bar{s},2}, A_{s\bar{s},2}$ are the scalar and gauge fields of the first and second string-antistring pairs, respectively.

Cosmological strings are expected to be mildly relativistic and so we chose $|\mathbf{v}_1| = 0.6$ and $|\mathbf{v}_2| = 0.33$. The directions were taken to be $(\hat{v}_1)_x = 0.4$, $(\hat{v}_1)_y = \sqrt{1 - 0.4^2} \approx$

0.92 for the two strings oriented along the z-axis and $(\hat{v}_2)_z = 0.4$, $(\hat{v}_2)_y \approx 0.92$ for those along the x-axis. The string velocities are approximately aligned along the y-axis, but not exactly, to avoid overly symmetrical loops that tend to pass through a double line configuration and collapse prematurely. We experimented with a wide range of initial velocities and our main conclusions are independent of the particular choices of these parameters.

Given the initial conditions for fields ϕ, A_μ, we evolved them using the discretized version of Eqs. (5.1)-(5.3) with $e = 1$, $\lambda = 1/2$, $\eta = 1$ and $g_p^2 = 0.75$. We used the explicit Crank-Nicholson algorithm with two iterations for the evolution (Teukolsky (2000)) and periodic boundary conditions. We tried different lattice spacings to study the effects of numerical resolution. The initial string spacing was set to a fixed fraction of the simulation box size so that smaller loops ran in a smaller box, with less computational cost.

Because of periodic boundary conditions, the reconnection of four strings produces two loops – the central loop in the middle of the box shown in Fig. 5.1, and an "outer" loop formed from the "fragments" in the corners of the box. The two loops then oscillate and decay without intersecting each other. We tracked the loop energy by summing the energy density in the "core" of the string. The energy density is given by

$$\mathcal{E} = \frac{1}{2}|D_0\phi|^2 + \frac{1}{2}|D_i\phi|^2 + \frac{1}{2}(\mathbf{E}^2 + \mathbf{B}^2) + \frac{\lambda}{4}(|\phi|^2 - \eta^2)^2 \,, \tag{5.16}$$

where $\mathbf{E}$ and $\mathbf{B}$ are the electric and magnetic field vectors, with their components defined as $E_i = F_{0i}$ and $B_i = -\frac{1}{2}\epsilon_{ijk}F_{jk}$. We define the string core to be the cells where the magnitude of the scalar field, $|\phi|$, is less than 0.9η.

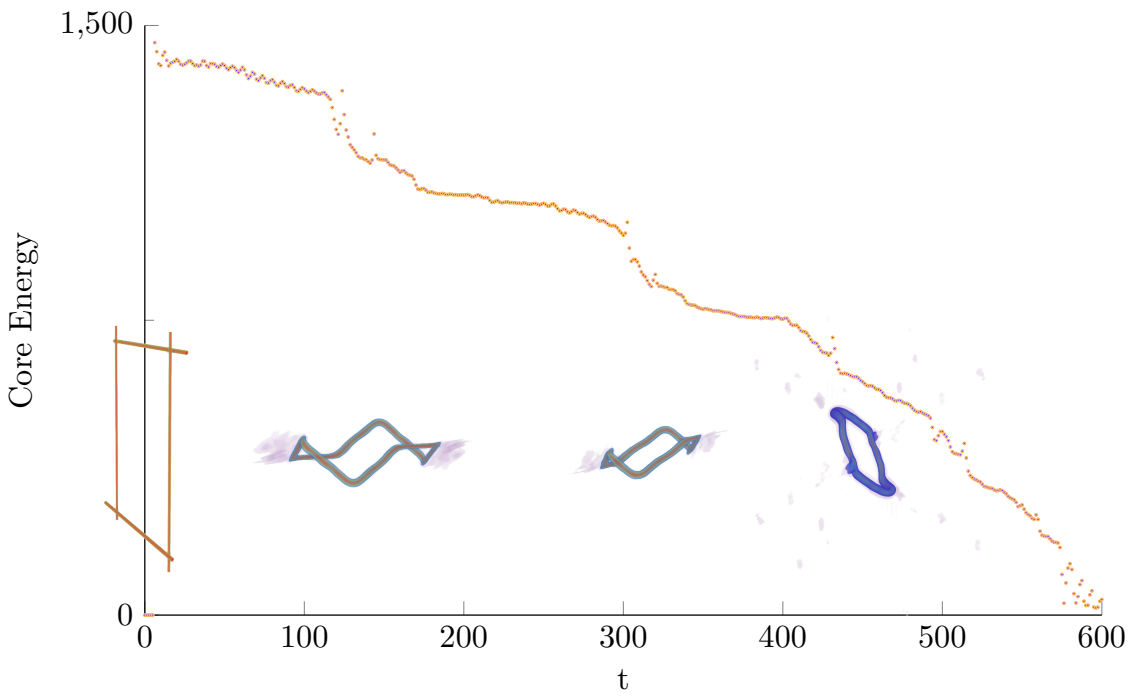

Figure 5.2: Energy of a loop with the initial size of 390 lattice spacings plotted vs time. Overlaid on the plot are snapshots of the loop as it goes through phases of rapid radiation discharge due to smoothening of kinks. The animation showing the evolution of this loop can be found at (Gauge String Movie (2019)).

5.3 Results and Conclusions

In Fig. 5.2 we plotted the loop energy vs time for a simulation on a 600^3 lattice with $\Delta x = 0.25$, where the initial size of the loop is 390 lattice spacings. (The animation of the loop evolution can be found at (Gauge String Movie (2019)).) The plot suggests episodic radiation, with the overlaid snapshots showing the representative "events" leading to drops in the loop energy. Straight strings do not radiate as they correspond to a boosted string solution. The kinks on the loop, formed at the intercommutation of the straight strings, also propagate with minimal energy loss. We found that noticeable radiation is produced when kinks collide. Also, as the kinks smooth out, there are episodes of large radiation which may be due to the formation of weak cusps.

Lattice size	Inner loop	Outer loop
400^3	140	260
600^3	210	390
800^3	280	520
1200^3	420	780

Table 5.1: Loop sizes in lattice units for each of the runs.

Particle radiation from cusps was studied by Olum and Blanco-Pillado (1999) where they found that the energy emission from a cusp leads to the formation of kinks and to weak cusps in subsequent loop oscillations. This pattern of episodic radiation from kink collisions and weak cusps, with relatively minor energy loss in between these events, is common to all loop simulations we have performed.

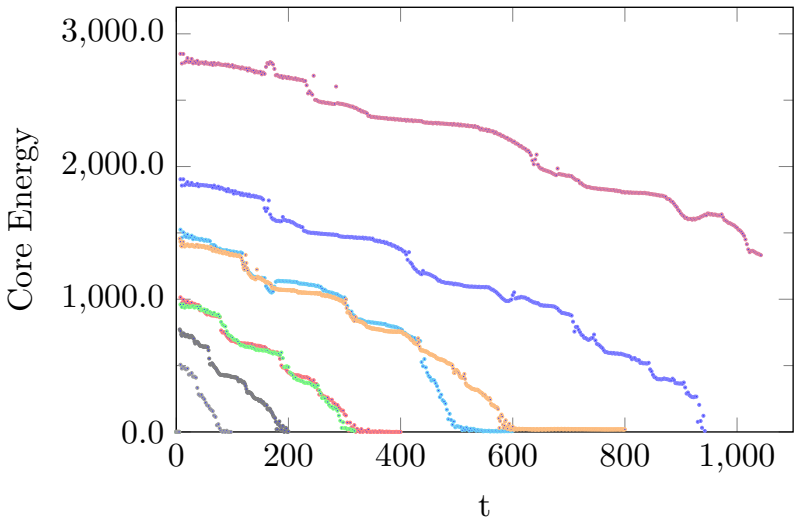

Figure 5.3: Loop energy vs. time for 8 different loops in 4 separate runs at $\Delta x = 0.25$ resolution.

To obtain a quantitative measure of the scaling of the loop half-life with its size, we ran simulations for 4 different box sizes yielding 8 loops given in Table 5.1. (Two loops from different runs are almost the same length and provide a check on our

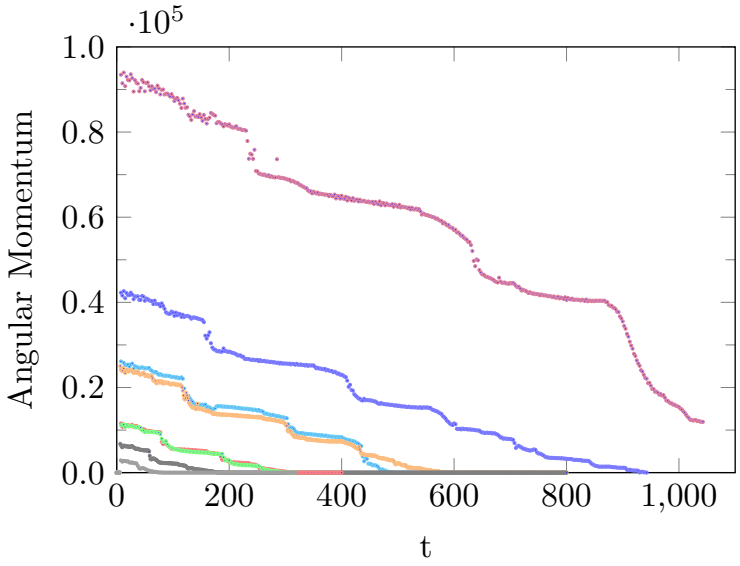

Figure 5.4: Loop angular momentum vs. time for 8 different loops in 4 separate runs at $\Delta x = 0.25$ resolution.

simulation.) Fig. 5.3 shows the loop energy versus time for the 8 loops. As the loops evolve, they also shed their angular momentum, defined as

$$L_i \equiv \epsilon_{ijk} \int_{\text{string core}} d^3x \, x_j [-\frac{1}{2}((D_0\phi)(D_k\phi)^* + (D_0\phi)^*(D_k\phi)) + \epsilon_{klm} E_l B_m] \, . \tag{5.17}$$

In Fig. 5.4 we plot $|\mathbf{L}|$ vs time and also see episodic decay.

We ran our simulations for a few different values of the lattice spacing, Δx, and found that the results are sensitive to the resolution. For example, as shown in Fig. 5.5, the total energy in the simulation box over the entire run is conserved only at $\sim 33\%$ level when $\Delta x = 0.50$. For $\eta = 1$, $e = 1$, $\lambda = 1/2$, the string width is ~ 1. Therefore, with $\Delta x = 0.5$ we only have a few lattice points within the width of the string. Using $\Delta x = 0.25$ improves the conservation to $\sim 5\%$ level and agrees well with the much more computationally expensive run with $\Delta x = 0.125$. The choice of Δx makes an important difference in the lifetime of the loop, as is clear from the right panel of Fig. 5.5. Loops live longer in simulations with better resolution. From the animations, we saw that the shorter loops live for about one oscillation period

while the larger loops survive for several oscillation periods. (There is ambiguity in defining an oscillation period since the length of the loop and hence its oscillation period is changing relatively rapidly during the simulation.)

The longest loop we were able to simulate had energy $\sim 3\times 10^3$, which corresponds to length $L \sim 10^3 w$ where w is the width of the string. In cosmology we are interested in loops of length comparable to the cosmic horizon, which is orders of magnitude larger than the thickness of the string, perhaps by a factor $\sim 10^{60}$. So we needed to extrapolate our results to larger lengths. For this purpose we calculate the half-life, τ, *i.e.* the time it takes the loop to lose half its initial energy. In Fig. 5.6, we plot τ/τ_0, where $\tau_0 = 41.5/\eta$ is the half-life of the smallest loop in our simulations, versus the initial energy normalized by that of the smallest loop (denoted $E_0 = 506\eta$). We find a power law fit,

$$\tau = \tau_0 \left(\frac{E}{E_0}\right)^p = \frac{1.6\times 10^{-3}}{\eta}(\eta L)^p, \quad p \approx 2 \tag{5.18}$$

where we have reinserted dimensional factors of η.

The L^2 scaling in Eq. (5.18) can be understood as following from radiation being due to episodes involving a fixed number of features (kinks and weak cusps) on the loop, with the power emitted in a given episode (a kink collision or a weak cusp) being independent of L. (Note that the size of the steps seen in Fig. 5.3 is similar for different loops). If ν denotes the number of episodes per period and each episode radiates energy ϵ on average, the energy lost per unit time is

$$\dot{E} \sim -\frac{\nu\epsilon}{L} \sim -\frac{\mu\nu\epsilon}{E}. \tag{5.19}$$

Integration of this equation gives a lifetime

$$\tau \sim \frac{E^2}{\mu\nu\epsilon} \sim \frac{\mu L^2}{\nu\epsilon} \tag{5.20}$$

in agreement with the L^2 scaling in Eq. (5.18).

The particle radiation rate in Eq. (5.19) is to be contrasted with $\dot{E} \sim \nu G\mu^2$ expected due to gravitational wave radiation from ν radiation episodes involving kinks and cusps (Vachaspati and Vilenkin (1985); Garfinkle and Vachaspati (1987); Binetruy *et al.* (2009)). Note that the rate of energy loss to gravitational radiation is not suppressed by a factor of L as is the case for particle radiation in Eq. (5.19). This is because, for example, a cusp on a loop that is twice as large is also twice as large, and the gravitational energy emitted by a single cusp is proportional to L. Then the lifetime of the loop due to gravitational radiation is

$$\tau_g \sim \frac{L}{\nu G\mu}\,. \tag{5.21}$$

Comparing this to Eq. (5.20) allowed us to derive a criterion for when the gravitational radiation is more important than particle radiation, namely, when

$$\tau_g < \tau \quad \Rightarrow \quad L \gtrsim \frac{\epsilon}{G\mu^2} \sim \frac{w}{G\mu}\,, \tag{5.22}$$

where w is the string thickness and we estimate $\epsilon \sim \sqrt{\mu}$, *i.e.* the particle energy emitted in an episode is comparable to the energy scale of the string, and $l_P \sim 10^{-33}$ cm is the Planck length. Note that ν has canceled out in Eq. (5.22). Therefore, even if there are more episodes on larger loops, gravitational radiation still dominates over particle radiation if Eq. (5.22) is satisfied.

With $L \sim 10^{27}$ cm we find that gravitational radiation is less important than particle radiation if $G\mu \lesssim 10^{-40}$, corresponding to $\eta \sim 100$ MeV or the QCD scale. Hence particle radiation could be the main decay mechanism for strings formed below the QCD scale but the dynamics of strings formed at such low energies is expected to be dominated by friction with the ambient medium (Vilenkin and Shellard (2000)).

Alternately, for strings close to the current bound on the string tension, $G\mu \approx 10^{-11}$, Eq. (5.22) implies that particle radiation will only be important for loops that

are very small, $L < 10^{-17}$ cm. Most of the radiation from such a network of strings will be in gravitational waves.

We would like to point out some caveats to the above discussion. The first caveat is that the long strings in our initial conditions are straight and smooth. If these strings started out with structure (perhaps as shallow kinks) on them, as has been suggested by Hindmarsh *et al.* (2009b), the number of radiative episodes would be larger, and both the particle and gravitational radiation would be larger. This would not change the relative importance of particle and gravitational radiation but it would mean that the loop decays faster. A second caveat is that our loops only contain kinks and no cusps. It is known from the computations Olum and Blanco-Pillado (1999) did that the radiation loss from a cusp is proportional to $\sqrt{L}$ and this does not agree with our model where each episode emits radiation that is independent of L. However, once the cusp radiates, it forms two kinks that then propagate, radiate and smooth out to some extent. In the next oscillation, the cusp is weaker and the energy radiated will not be proportional to $\sqrt{L}$, instead it will be proportional to some power of L smaller than $1/2$. Thus with cusps we expect that the effective value of p will satisfy $1 < p < 3/2$, and Eq. (5.22) will get modified. Even then there will be a critical loop length such that gravitational emission dominates over particle radiation for larger loops. A third caveat is that since our initial strings were straight, there was no radiation while the kinks propagate on the straight segments. If, however, the segments are curved, there will be some radiation even from a propagating kink. This radiation would not be episodic but it would be suppressed by the curvature of the segment, expected to be suppressed by the loop size divided by the cosmic horizon scale.

To summarize, we studied the formation and evolution of cosmic string loops in field theory and estimated their lifetimes. We found that the lifetime of the loops is very sensitive to the resolution used in their numerical evolution. With insufficient

resolution, the loops collapse within one oscillation period. At higher resolution, the loops survive for a few oscillation periods and we observe that their lifetime grows as L^2. We can explain this growth in terms of episodic particle radiation. When compared to gravitational energy losses, we find that gravitational radiation dominates for loops that are larger than a critical length (see Eq. (5.22)).

To make further progress in the understanding of the decay of cosmic string loops, we plan to study the scaling of decay modes for loops of different shapes and larger number of kinks. This would further confirm the results we have obtained above. In the next chapter, we will explore the dynamics of global cosmic string loops. Global string loops do not face Higgs screening by the gauge fields and therefore have significantly different interactions compared to local strings. Global strings interact through long range forces, and since gauge field doesn't compensate for variations in the scalar field, the energy density is logarithmically divergent. Another reason to study global strings is that various axion models contain a broken $U(1)$ symmetry and therefore contain vortex solutions (Battye and Shellard (1999); Fleury and Moore (2016); Gorghetto *et al.* (2018)). This means during Peccei-Quinn phase transitions, a network of axion strings could have formed. Therefore, it is important to study the radiation spectrum of axion strings.

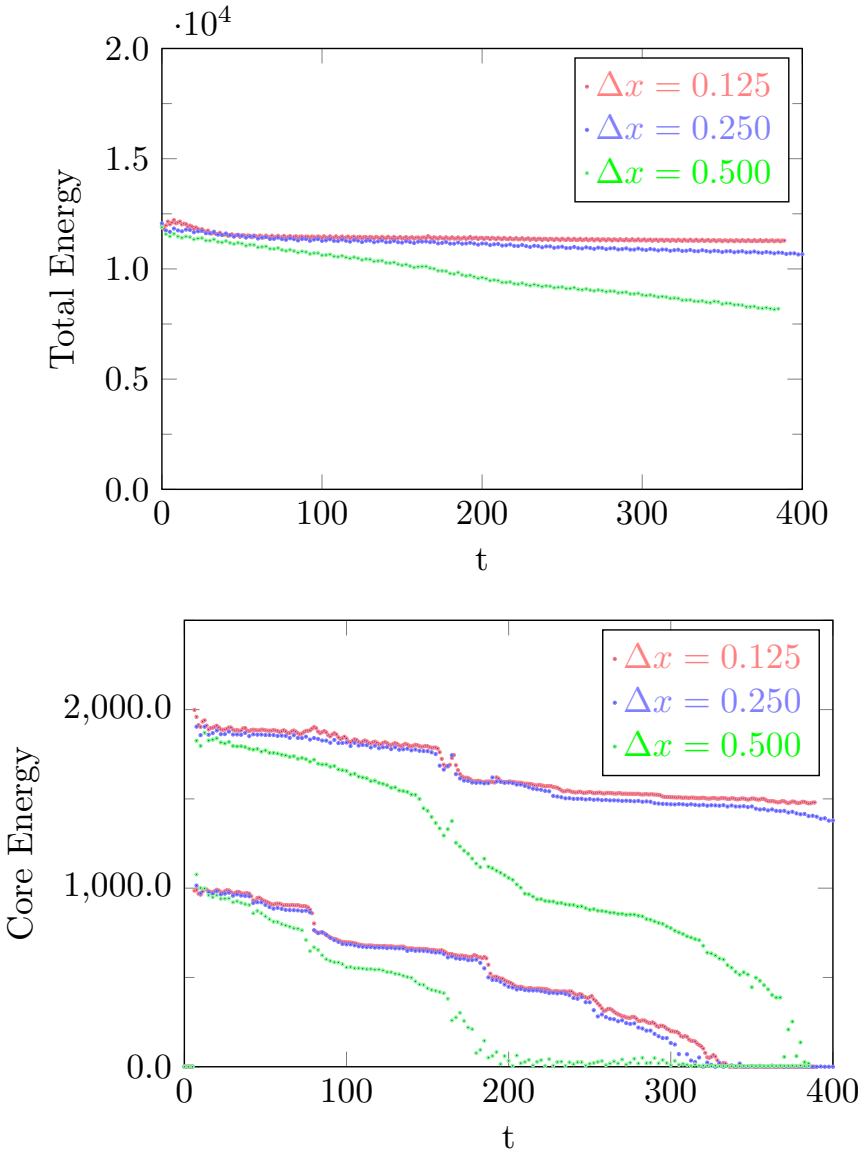

Figure 5.5: Comparison of runs with different lattice resolution $\Delta x = 0.125, 0.25, 0.5$ on lattices of sizes 800, 400, and 200, respectively, corresponding to a fixed physical lattice length of 100. The left panel shows the total energy in our simulation box and the right panel shows the evolution of the energy in the two loops in the box. The plots show convergence at higher resolution and that $\Delta x = 0.25$ offers a good compromise between accuracy and speed.

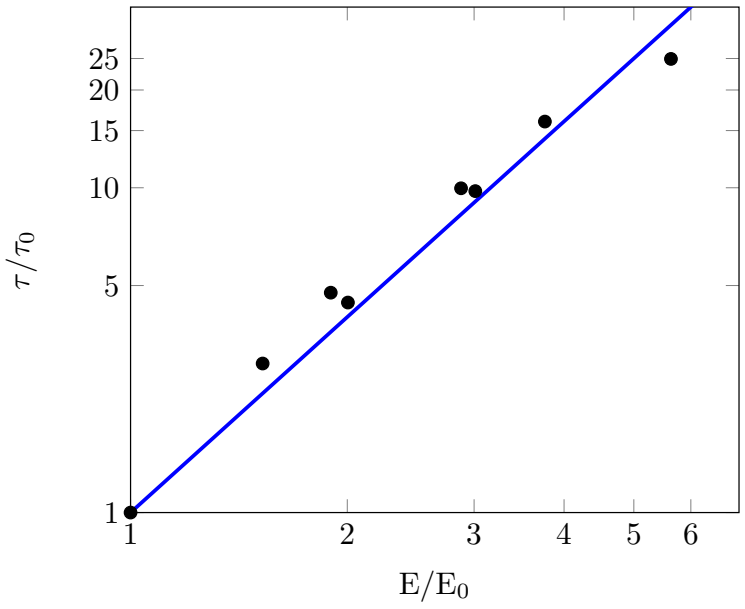

Figure 5.6: Plot of the loop half-life versus initial energy (proportional to the initial length) in the loop. They are normalized by the initial half-life of the smallest loop, τ_0, and its energy, E_0. The straight line fit shows that $\tau \propto L^2$ where L is the initial length of the loop.

Chapter 6

DECAY OF COSMIC GLOBAL STRING LOOPS

The emission of Goldstone radiation from global string loops has been investigated in the Nambu-Goto limit in which the string core has negligible thickness (Vilenkin and Vachaspati (1987)). The calculation is enabled by replacing the scalar field for the Goldstone degree of freedom by a two form gauge field, leading to the Kalb-Ramond description of the string (Kalb and Ramond (1974)). The radiation has also been studied by numerically evolving the field theory configuration of a string loop (Hagmann and Sikivie (1991); Hagmann *et al.* (2001)). Both methods have their limitations. The Kalb-Ramond approach assumes that there is only Goldstone boson radiation and no massive scalar radiation. Also, the backreaction of Goldstone boson radiation on the string dynamics has not yet been taken into account. The numerical field theory method involves a full description of the problem but is limited in dynamic range. Hence the results must be extrapolated to long loops such as would arise in cosmology.

Here we adapt our numerical field theory study of local cosmic string loops (Matsunami *et al.* (2019)) to the case of global strings (Saurabh *et al.* (2020)). The key features of our work that distinguish it from the earlier field theory loop simulations (Hagmann and Sikivie (1991); Hagmann *et al.* (2001)) are that (i) we consider loops that are formed from the collision of long straight strings, much as they might form in cosmology, and (ii) we consider relatively long loops, several hundred times the width of the string core. The first feature helps to set up the initial conditions, as the straight string solution is known and we only need to patch together the solutions. The second feature helps with the extrapolation to cosmological scales.

Our results are summarized as follows. Global string loops emit both massless Goldstone radiation and massive particles (denoted by χ) and decay in a time proportional to the size of the loop L. Initially our loops have length $4L$ and invariant length (energy divided by string tension) of 5L due to a Lorentz boost factor of 1.25. We find that the energy distribution of massive particles is peaked at very low wavenumbers and they are non-relativistic at production. Eventually the massive particles will decay into Goldstone bosons but their decay leaves a sharp feature in the spectrum of Goldstone bosons. The energy spectrum of radiated Goldstone bosons takes the form,

$$\frac{d\mathcal{E}_k}{dk} = \eta^2 L \frac{a}{k}, \quad (2L)^{-1} \leq k \lesssim m_\chi \,, \tag{6.1}$$

where, η is the vacuum expectation value of the scalar field, k is the magnitude of the wavevector, and $a \approx 4.8$ is a coefficient that we determine numerically. Although the spectrum is peaked at the smallest wavevector, the integrated energy at larger momenta is greater for large loops because this contribution grows as $\ln(m_\chi L)$.

In Sec. 6.1 we describe the field theory, some basic features of cosmic strings, and our scheme for producing a global string loop. We then turn to our numerical implementation on a lattice with periodic boundary conditions (PBC) in Sec. 6.2, where we also describe the results of our simulations, contrasting global string evolution with that of gauge strings. In Sec. 6.3 we turn to the radiation produced by the loops and evaluate the fraction of energy in massless to massive radiation. The spectrum of radiation is discussed in Sec. 6.4. Here we analyze the spectral features of both massive and massless radiation from global strings, and find a good fit to the form of the spectrum in Eq. (6.1) for the Goldstone radiation. We conclude in Sec. 6.5, where we also place our results in the context of earlier work. The implementation of periodic boundary conditions requires care as the Goldstone boson cloud around

the string loop decays relatively slowly and reaches the boundaries of the lattice. We describe our implementation in Appendix A.

6.1 Model

We consider the global $U(1)$ field theory with a complex scalar field, $\phi = \phi_1 + i\phi_2$, for which the field equations of motion are

$$\partial_t^2 \phi_a = \nabla^2 \phi_a - \lambda(\phi_b \phi_b - \eta^2)\phi_a \,, \tag{6.2}$$

where $a = 1, 2$, λ is a coupling constants. By suitable rescalings of the fields and the coordinates, we can set $\lambda = 1/2$ and $\eta = 1$ and then the (classical) model has no free parameters.

The solution for a straight global string along the $z-$axis is

$$\phi = \eta f(r) e^{i\varphi} \,, \tag{6.3}$$

where $r = \sqrt{x^2 + y^2}$, $\varphi = \tan^{-1}(y/x)$, and $f(r)$ is a string profile functions that vanishes at the origin and asymptotes to 1 as

$$f(r) \to 1 - \mathcal{O}\left(\frac{1}{r^2}\right) . \tag{6.4}$$

The energy density in the scalar field is given by

$$\mathcal{E} = \frac{1}{2}|\partial_t \phi|^2 + \frac{1}{2}|\nabla \phi|^2 + \frac{\lambda}{4}(|\phi|^2 - \eta^2)^2 \,, \tag{6.5}$$

which, if we write $\phi \equiv \rho \exp(i\alpha)$, can also be expressed as

$$\mathcal{E} \equiv \mathcal{E}_\rho + \mathcal{E}_\alpha \,, \tag{6.6}$$

where the energy density in massive modes (ρ) is defined as

$$\mathcal{E}_\rho = \frac{1}{2}(\partial_t \rho)^2 + \frac{1}{2}(\nabla \rho)^2 + \frac{\lambda}{4}(\rho^2 - \eta^2)^2 \,, \tag{6.7}$$

and that in Goldstone modes (α) as

$$\mathcal{E}_\alpha = \frac{\rho^2}{2}\left[(\partial_t\alpha)^2 + (\nabla\alpha)^2\right] . \tag{6.8}$$

The string energy per unit length (also its tension) is found by integrating the energy density of the solution in Eq. (6.3) in the $z = 0$ plane. The integration of $\mathcal{E}_\rho$ is finite but the integral of $\mathcal{E}_\alpha$ diverges logarithmically with distance. With a long range cutoff at $r = \Lambda$ the energy per unit length is

$$\mu \approx \pi\eta^2 \ln(\Lambda\eta) . \tag{6.9}$$

We now create a loop for our simulations following the scheme developed in the previous chapter Matsunami *et al.* (2019). Our initial conditions consist of four straight strings boosted with velocities $\pm\mathbf{v_1}$ and $\pm\mathbf{v_2}$ as shown schematically in Fig. 5.1. The four string solutions are patched together using the "product ansatz". If Φ_a ($a = 1, \ldots, 4$) denotes the solution for the individual strings, the field is taken to be

$$\phi(t = 0, \mathbf{x}) = \frac{1}{\eta^3}\prod_{a=1}^{4}\Phi_a , \tag{6.10}$$

and the time derivatives at the initial time are

$$\dot{\phi}(t = 0, \mathbf{x}) = \phi(t = 0, \mathbf{x})\sum_{b=1}^{4}\frac{\dot{\Phi}_b}{\Phi_b} , \tag{6.11}$$

with $\dot{\Phi}_b$ obtained from the boosted solution for a single string.

While this scheme can be used to construct a loop in an infinite spatial volume, our simulations are on a finite lattice and employ periodic boundary conditions. These numerical limitations necessitate some modifications of the initial conditions that are described in Appendix A.

6.2 Simulation and Results

Once the four strings collide, they reconnect to form two loops – two because of periodic boundary conditions. If the string velocities are small and not oriented suitably, the resulting loops will have insufficient angular momentum and will collapse quickly. We choose velocity magnitudes that are mildly relativistic, $|\mathbf{v}_1| = 0.6 = |\mathbf{v}_2|$, as expected in a cosmological setting. The directions are taken to be $(\hat{v}_1)_x = 0.4$, $(\hat{v}_1)_y = \sqrt{1 - 0.4^2} \approx 0.92$ for the two strings oriented along the z-axis and $(\hat{v}_2)_z = 0.4$, $(\hat{v}_2)_y \approx 0.92$ for the strings along the x-axis.

Next we use the explicit Crank-Nicholson algorithm with two iterations for the numerical evolution (Teukolsky (2000)) with periodic boundary conditions, keeping track of the energy densities in the core of the string and the Goldstone mode (see Eqs. (6.7) and (6.8)) and the total energy and angular momentum. The core of the string is defined as the region where $|\phi|/\eta < 0.9$. We take the initial string separation in Fig. 5.1 to be half the size of our lattice for all our runs. The simulation then produces two loops due to the periodic boundary conditions but both loops are the same size.

We have run our simulations for a few different values of the lattice spacing, Δx, and found that the results are sensitive to the resolution. For example, the total energy in the simulation box over the entire run is conserved only at $\sim 20\%$ level when $\Delta x = 0.50$ for longer runs (required for large lattices). We have set $\eta = 1$, $e = 1$, $\lambda = 1/2$ and so the string width is ~ 1. Therefore with $\Delta x = 0.5$ we only have a few lattice points within the width of the string. The run with $\Delta x = 0.25$ gives better conservation, to $\sim 5\%$ level over the entire run and agrees quite well with the much more computationally expensive run with $\Delta x = 0.125$.

In Fig. 6.1, we plot the loop energy vs time for several loop sizes with $\Delta x = 0.25$.

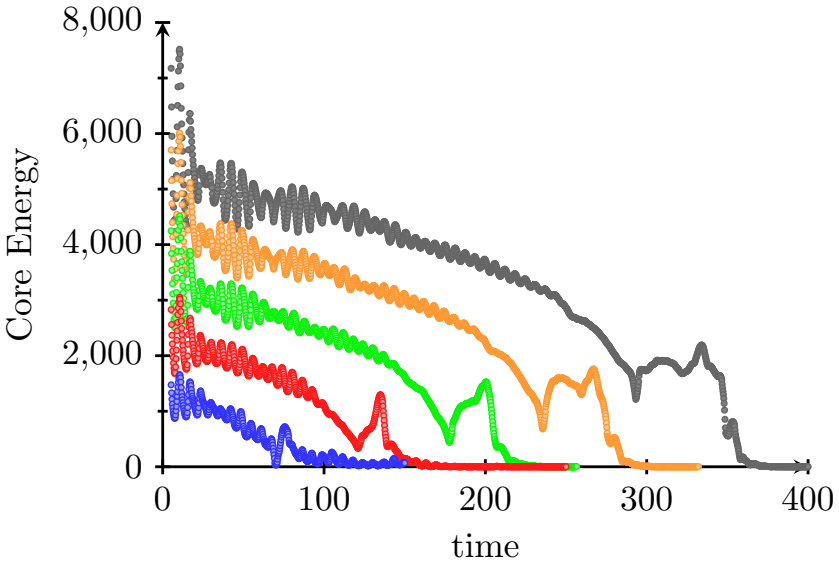

Figure 6.1: The loop energy as a function of time for the outer loop for different values of loop sizes $L = 50, 100, 150, 200, 250$ (lowest to the highest curve). A similar plot is obtained for the inner loops.

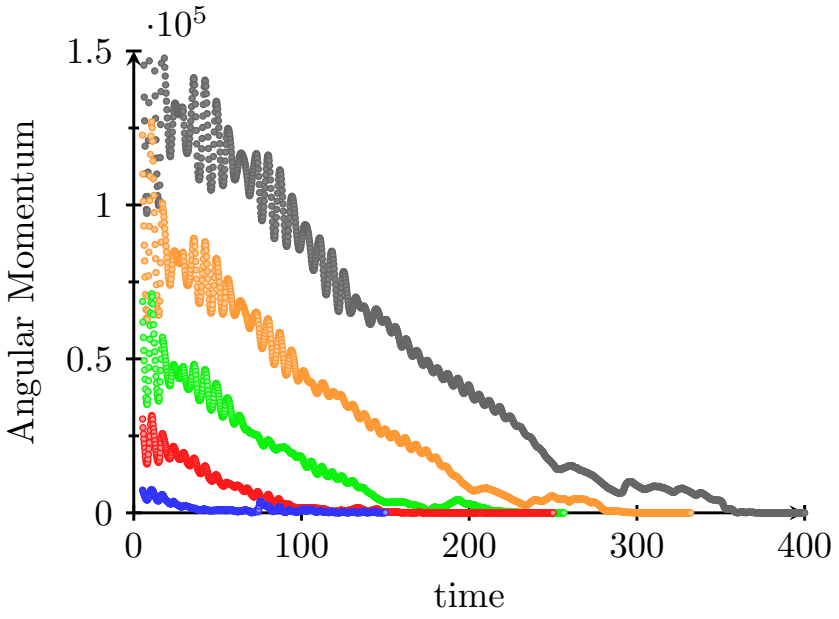

Figure 6.2: The loop angular momentum as a function of time for the outer loop for different values of loop sizes $L = 50, 100, 150, 200, 250$ (lowest to the highest curve).

We take the string core to be the lattice cells where $|\phi| < 0.9\eta$, with the sum of energies in all such cells giving the energy of the loop. Unlike in the case of gauge strings (Matsunami *et al.* (2019)), the decay of global string loops is not episodic and the energy gradually dissipates.

As the loops evolve, they also shed their angular momentum, defined as

$$L_i \equiv -\frac{1}{2}\epsilon_{ijk}\int_{\text{string core}} d^3x\, x_j \left(\partial_t\phi\partial_k\phi^* + \partial_t\phi^*\partial_k\phi\right) , \tag{6.12}$$

where x_j is measured from the center of energy of the loop. In Fig. 6.2 we plot $|\mathbf{L}|$ versus time and also see gradual decay.

6.3 Massive Versus Massless Radiation

The global string loop emits massive and massless Goldstone radiation. The massive radiation corresponds to excitations of the field ρ and its energy density is given in Eq. (6.7); the massless radiation corresponds to excitations of α with energy density given in Eq. (6.8). Note that ρ and α interact, which is evident in Eq. (6.8). However, at late times, we can write $\rho = \eta + \chi$, $\theta = \alpha$, where χ is a small excitation above the true vacuum and expand the energy density functions to lowest order in χ,

$$\mathcal{E}_\rho = \frac{1}{2}\left[(\partial_t\chi)^2 + (\nabla\chi)^2 + m_\chi^2\chi^2\right] + \ldots \equiv \mathcal{E}_\chi + \ldots , \tag{6.13}$$

$$\mathcal{E}_\alpha = \frac{\eta^2}{2}\left[(\partial_t\alpha)^2 + (\nabla\alpha)^2\right] + \ldots \equiv \mathcal{E}_\theta + \ldots , \tag{6.14}$$

where $m_\chi = \sqrt{2\lambda}\eta$. By integrating these expressions we obtain the total energy in the two components,

$$E_a = \int d^3x \mathcal{E}_a \, , \tag{6.15}$$

where $a = \rho$, α. At early times, E_ρ and E_α will differ from E_χ and E_θ, respectively, but they will coincide at late times, when $\rho \approx \eta$.

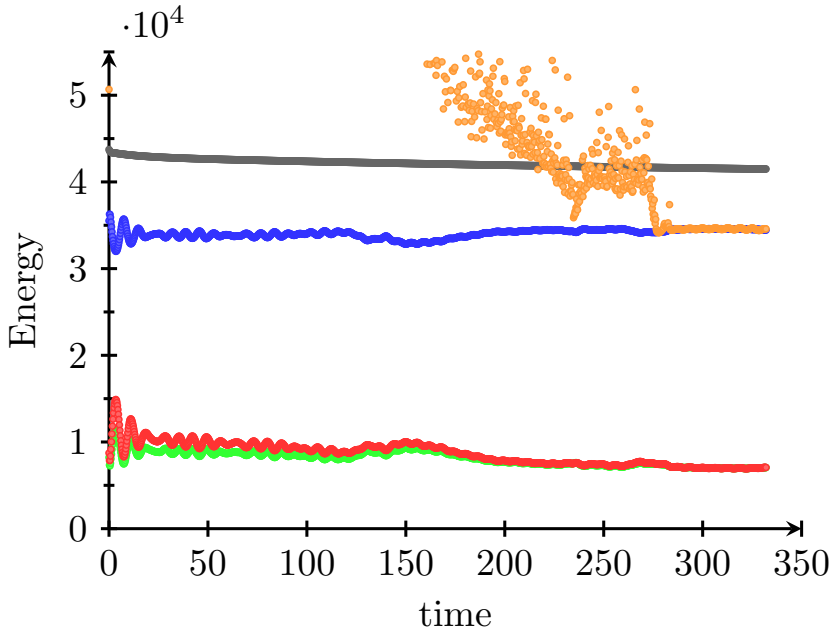

Figure 6.3: Energy in massive and massless components and total energy (TE) for $L = 200$. Lower curves are for massive radiation calculated as ρ (green) and χ (red). Middle curve is for Goldstone radiation calculated for θ (blue) and α (orange). Top curve (black) is the total energy.

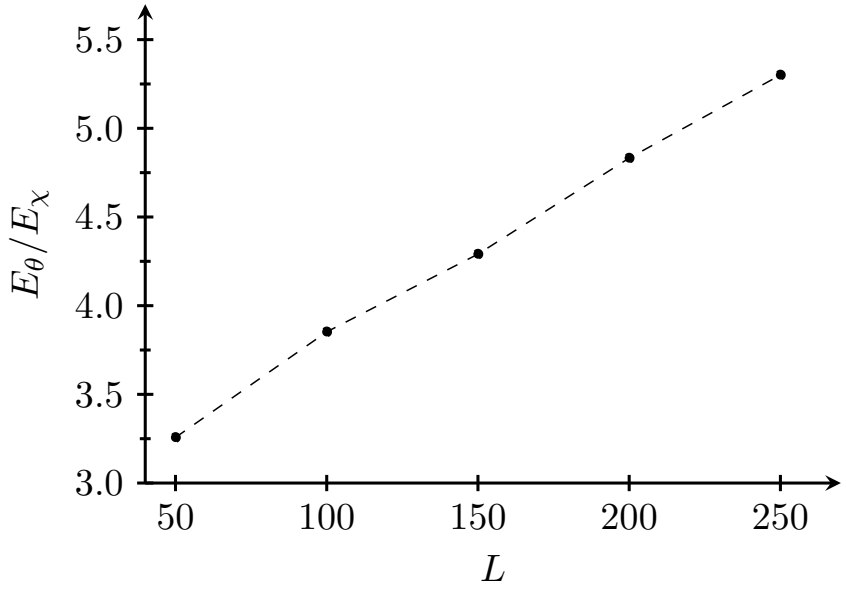

Figure 6.4: Plot for the ratio of energy in the Goldstone mode to energy in the massive mode at the decay time as a function of loop size.

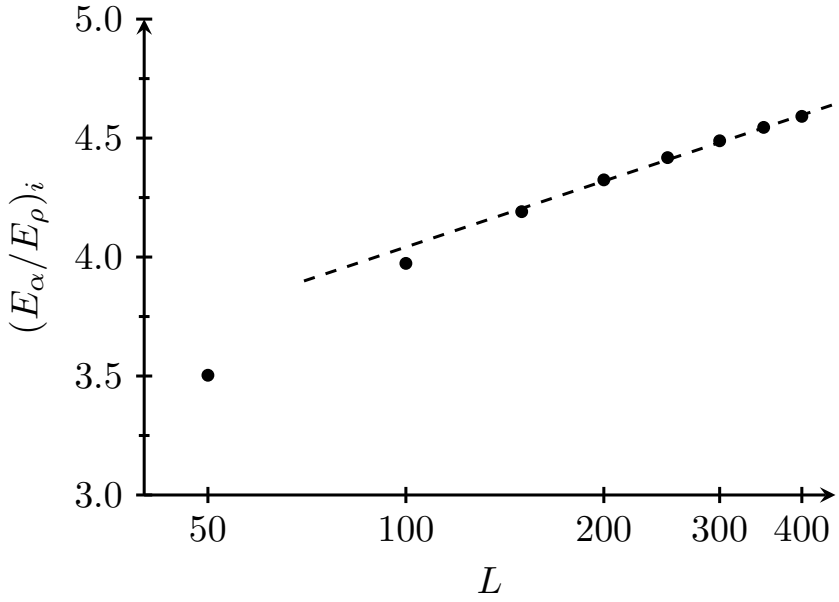

Figure 6.5: Log-linear plot for the ratio of initial energy in the Goldstone mode to initial energy in the massive mode as a function of loop size.

In Fig. 6.3 we plot the total energy in each of the components ρ, χ, α, and θ versus time in the run with lattice size 1600^3. We see that the Goldstone mode has significantly more initial energy compared to the massive mode and the ratio of the energies in ρ and θ remains approximately constant throughout the evolution. The energies in χ and θ agree with those in ρ and α once the loop has decayed as is expected. This pattern is repeated in all our simulations with different loop sizes, however, the ratio E_θ/E_χ increases with loop size. as seen in Fig. 6.4. This shows that massive radiation become less important for larger loops. To obtain the length dependence of the ratio, we need to find a fit to the plot in Fig. 6.4. Unfortunately we could not find an unambiguous fit to the data – a linear dependence, power law dependence and logarithmic dependence, all seem to fit the data equally well. Yet, based on Fig. 6.3 there is an alternate way to estimate the length dependence of the ratio. This method uses the observation that the energies in χ and θ are

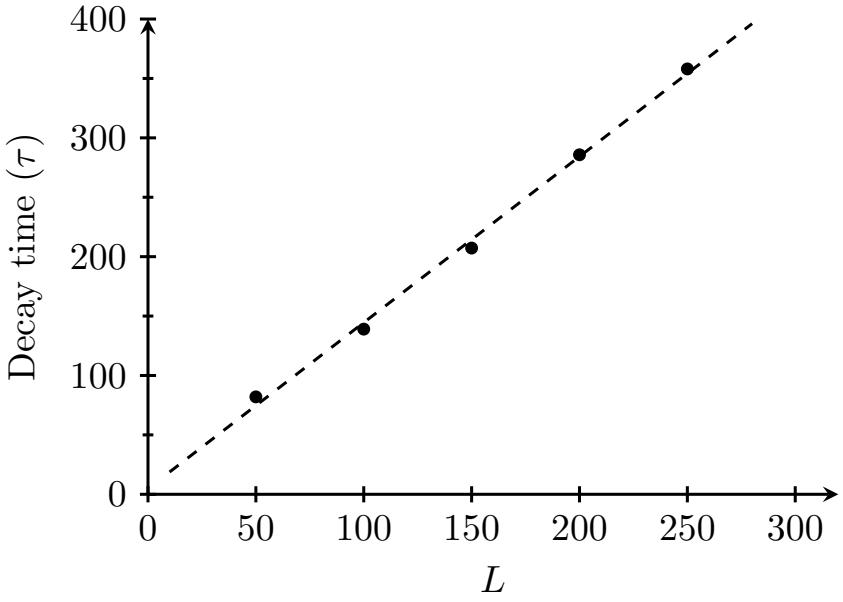

Figure 6.6: The loop decay time as a function of the loop size. The best fit line is $\tau = 1.39L + 4.75$.

approximately conserved during the collapse time. (Eventually χ particles will decay into Goldstone bosons.) So to obtain the ratio we simply need to estimate these energies at the initial time, which we can do using the initial conditions described in Sec. 6.1. Since no evolution is necessary to get the initial energies, we can go to much larger lattices. The initial ratios versus L are shown in Fig. 6.5 on a log-linear plot, showing that the ratio grows as $\ln(m_\chi L)$. The logarithm can also be understood by noting that the energy of the Goldstone cloud around a single global string diverges logarithmically with distance from the string (see Eq. (6.9)). For a loop, the loop size provides a cutoff on the divergence but it means that the Goldstone cloud has energy proportional to $\ln(m_\chi L)$. In our simulations, we have modified the string ansatz slightly to account for the periodic boundary conditions as described in Appendix A, so we have calculated the energy numerically as shown in Fig. 6.5.

We use Fig. 6.3 to define the loop lifetime τ: the θ and α curves coincide once the

strings have decayed and $\rho \approx \eta$ is a good approximation. The loop lifetime τ versus loop length is shown in Fig. 6.6 and is well-described by a linear relation $\tau \approx 1.4L$.

In Fig. 6.7 we show a snapshot of the potential energy density at an intermediate time in the evolution. Unlike the gauge string, the global string is "fluffy", which may be understood as due to the soft power law profile function in Eq. (6.4) as opposed to the hard exponential profile functions in the gauge case. Deformations of the core correspond to excitations of the massive degree of freedom. In the animations we see that the kinks get rounded out but they also produce bulges in the string core as seen in Fig. 6.7. The transfer of energy from kink collisions to core oscillations is an intermediate step in the process of the eventual decay of the entire loop energy into Goldstone modes that is not accounted for by the Kalb-Ramond approximation. It remains to be determined if the core oscillations play a significant role for cosmological size loops.

The bulges in Fig. 6.7 suggest the existence of a bound state on a global string and we can confirm this explicitly. Consider a perturbation of a straight global string oriented along the z axis,

$$\phi(t, r, \theta, z) = (f(r) + e^{-i\omega t} g(r)) e^{i\theta} \,, \tag{6.16}$$

where we have set $\eta = 1$ for convenience. (To obtain bound states that propagate along the string, we would replace ωt by $\omega t - kz$.) The string profile function satisfies

$$-f'' - \frac{f'}{r} + \left[\frac{1}{r^2} + \frac{1}{2}(f^2 - 1)\right] f = 0 \,, \tag{6.17}$$

with $f(0) = 0$ and $f(\infty) = 1$. Upon linearization, the perturbation $g(r)$ satisfies the Schrodinger-type equation

$$-g'' - \frac{g'}{r} + \left[\frac{1}{r^2} + \frac{3}{2}(f^2 - 1)\right] g = \Omega g \,, \tag{6.18}$$

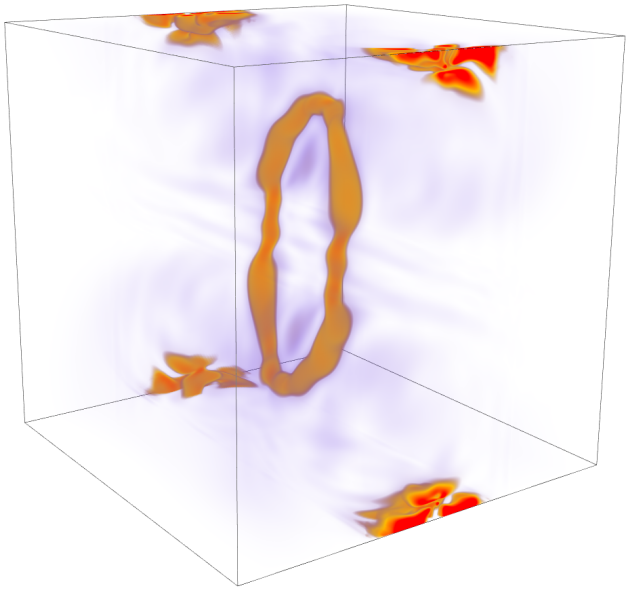

Figure 6.7: A snapshot of the potential energy density for a loop with $L = 50$ at an intermediate time showing a "fluffy" deformable core and massive radiation. The full animation can be seen at the webpage (Global String Movie (2020)).

where $\Omega \equiv \omega^2 - 1$ and $g(0) = 0 = g(\infty)$. A non-trivial bound state solution, *i.e.* with $\Omega < 0$, of this equation corresponds to a bound state deformation of the global string profile. That a bound state should exist can be seen by comparing Eqs. 6.17 and 6.18. The potential term in square brackets in the Schrodinger equation Eq. (6.18) is deeper than the corresponding term appearing in Eq. (6.17) by the extra term $2(f^2-1)/2 < 0$. We know that $f(\infty) = 1$, so the extra term in the potential in Eq. (6.18) will have the effect of decreasing g as compared to f and can make it vanish asymptotically for the correct eigenvalue Ω. We have confirmed this by solving Eqs. (6.17) & (6.18) and determine the lowest energy eigenvalue to be $\Omega \approx -0.19$, thus explicitly showing the existence of massive bound states on the global string.

6.4 Energy Spectrum

We begin by decomposing the fields χ and $\theta = \alpha$ into Fourier modes,

$$\chi = \int \frac{d^3k}{(2\pi)^3} \left[\chi_{\mathbf{k}}(t)e^{-i\mathbf{k}\cdot\mathbf{x}} + \chi^*_{\mathbf{k}}(t)e^{+i\mathbf{k}\cdot\mathbf{x}}\right] , \tag{6.19}$$

$$\theta = \int \frac{d^3k}{(2\pi)^3} \left[\theta_{\mathbf{k}}(t)e^{-i\mathbf{k}\cdot\mathbf{x}} + \theta^*_{\mathbf{k}}(t)e^{+i\mathbf{k}\cdot\mathbf{x}}\right] . \tag{6.20}$$

The energy densities in a Fourier mode labeled by $\mathbf{k}$ are given by

$$\mathcal{E}_{\chi\mathbf{k}} = \frac{1}{2}\left[|\partial_t\chi_{\mathbf{k}}|^2 + (k^2 + m_\chi^2)|\chi_{\mathbf{k}}|^2\right] , \tag{6.21}$$

$$\mathcal{E}_{\theta\mathbf{k}} = \frac{\eta^2}{2}[(\partial_t\theta_{\mathbf{k}})^2 + k^2|\theta_{\mathbf{k}}|^2] . \tag{6.22}$$

In general, the spectra will depend on all three components of the wavevector $\mathbf{k}$. However, if we sum over a large number of loops, with different shapes, sizes and orientations, we can expect an isotropic spectrum. To extract an isotropic spectrum from our simulation we bin the spectral components according to their $k = |\mathbf{k}|$ value and sum over all modes with $|\mathbf{k}|$ in the interval $\mathcal{R}(k) = (k - \Delta k, k)$, where $\Delta k = 2\pi/(2L)$ ($2L$ is the lattice size in our simulations):

$$\mathcal{E}_{\chi k} = \frac{(\Delta k)^3}{(2\pi)^3} \sum_{|\mathbf{k}|\in\mathcal{R}(k)} \mathcal{E}_{\chi\mathbf{k}} , \quad \mathcal{E}_{\theta k} = \frac{(\Delta k)^3}{(2\pi)^3} \sum_{|\mathbf{k}|\in\mathcal{R}(k)} \mathcal{E}_{\theta\mathbf{k}} . \tag{6.23}$$

Note that the sum is over vectors $\mathbf{k}$ with the same magnitude. Hence, it includes the $4\pi k^2$ factor that arises from the phase space volume factor and to obtain the total energy one only needs to sum over all the modes,

$$E_\chi = \sum_k \mathcal{E}_{\chi k} , \quad E_\theta = \sum_k \mathcal{E}_{\theta k} . \tag{6.24}$$

We plot $\mathcal{E}_{\chi k}$ versus k on a log-log scale in Fig. 6.8. The energy in the higher k modes does not depend on the size of the loop but the energy in the lowest few modes grows with the size of the loop. It is worth noting that the spectrum gets cut off at

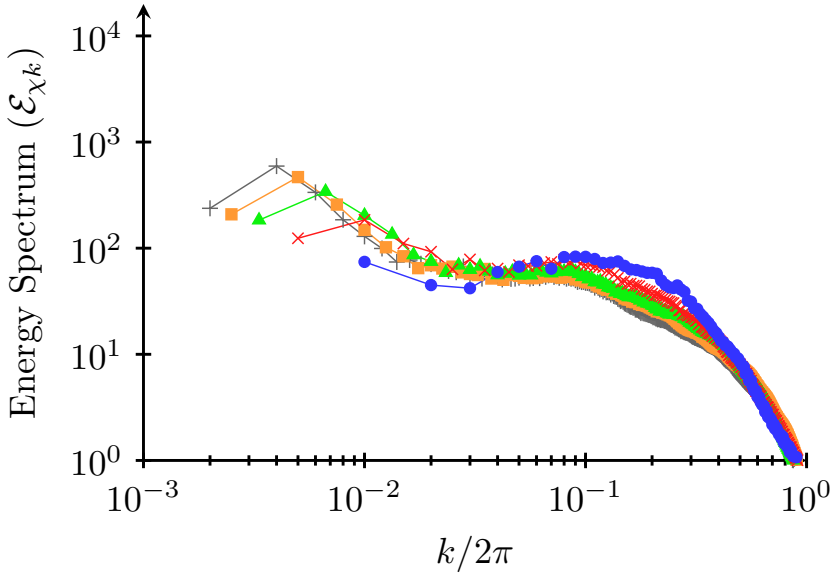

Figure 6.8: A log-log plot of the energy spectrum of massive radiation after the loops in the simulation have collapsed for the runs with initial loop size 50 (blue circles), 100 (red crosses), 150 (green triangles), 200 (orange squares), and 250 (black pluses).

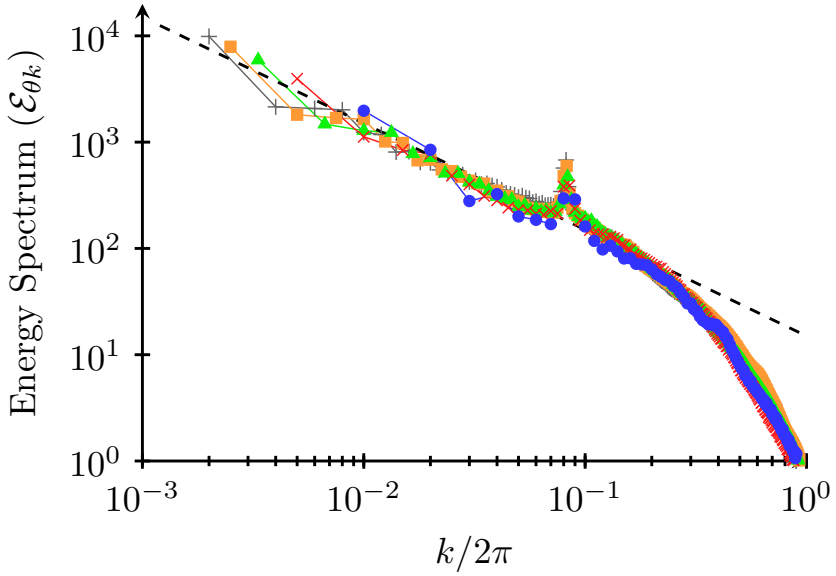

Figure 6.9: A log-log plot of the energy spectrum of Goldstone radiation when the initial loop size is 50 (blue circles), 100 (red crosses), 150 (green triangles), 200 (orange squares), and 250 (black pluses). The overlaid black dashed line is given by $15/k$ and is a good fit out to $k \approx 0.08 \times 2\pi \approx 0.5$. The peak at $k \approx 0.5$ corresponds to energy $\approx m_\chi/2$.

$k \approx 0.1 \times 2\pi \approx 0.6$ which corresponds to a momentum less than $m_\chi = 1$. Hence the massive particles emitted by the string are non-relativistic especially for long loops.

The spectrum for Goldstone radiation is shown in the log-log plot of Fig. 6.9. We see that the spectrum decays as $15/k$ until a cutoff wavenumber $k_c \approx 0.5$, after which there is essentially negligible energy contribution. To obtain the continuum version of the energy spectrum as given in Eq. (6.1), we divide both sides of Eq. (6.23) by $\Delta k = \pi/L$. Then,

$$\frac{d\mathcal{E}_{\theta k}}{dk} = \frac{L}{\pi}\frac{15\eta^2}{k} \approx 4.8\frac{\eta^2 L}{k}, \quad (2L)^{-1} \leq k \lesssim m_\chi \,. \tag{6.25}$$

One additional feature we see in the spectrum of Goldstone radiation is the peak at $k \approx 0.08 \times 2\pi$ in Fig. 6.9 for all the loops we have simulated. The location of the peak, at $k \approx 0.5 = m_\chi/2$, reveals the origin of this feature. It is caused by the massive particles that decay into Goldstone bosons due to the interaction $\chi(\partial_\mu\theta)^2$. Since a radiated χ is non-relativistic, it would decay into two Goldstone bosons, each with energy of about $m_\chi/2$.

6.5 Conclusions

In this paper we have focused on cosmic global string loops, their dynamics and decay. We numerically evolved loops of global string with length up to 1000 times the width of the string core. By extrapolating our results, we can meaningfully discuss cosmologically relevant loops whose size can be comparable to the cosmic horizon and many orders of magnitude larger than the core thickness.

Our results show that global string loops decay very quickly with lifetime $\sim L$ by radiating Goldstone bosons (θ) and massive particles (χ). Most of the energy is radiated in Goldstone bosons and the emission of χ is suppressed by $1/\ln(m_\chi L)$, which in a cosmological setting would be $\sim 0.01 - 0.1$. The emitted χ particles are

non-relativistic and they eventually decay into Goldstone bosons, producing a sharp peak in the Goldstone boson energy spectrum at $m_\chi/2$. In cosmology, the decay takes place continually during the evolution of the global string network and the sharp peak at $m_\chi/2$ gets smeared out due to cosmological redshifting of the energy. Even if the global string network were to decay at a specific epoch, as in the axion scenario, a sharp feature in the light particle (axion) spectrum that is produced due to heavy particle decay is not expected to survive. Such particles would be relativistic and their energy density would dilute like radiation instead of matter. The energy density of ultrarelativistic axions would be suppressed by the factor $z_{\rm QCD} \sim 10^{12}$ as compared to non-relativistic axions.

We have also extracted the energy spectrum for the Goldstone boson radiation from global string loops in our simulations. We obtain a $1/k$ spectrum, confirming that the results obtained by Hagmann and Sikivie (1991); Hagmann *et al.* (2001) hold even for loops formed by processes expected in a cosmological setting. The peak in our simulations, at $k \approx m_\chi/2$, is a new feature, though one that should have been expected in hindsight. The suppressed strength of the peak (1-10%) is due to the logarithmic divergence associated with the Goldstone component of global strings.

To summarize, we have obtained a remarkably simple picture for the decay of cosmic global string loops. Initially the loop consists of a massive field and a Goldstone field. The loop quickly collapses, releasing radiation of massive field and Goldstone bosons, with the Goldstone radiation retaining its original $1/k$ spectrum. The radiated total energies correspond to the initial energies in these components, except that the massive particles decay into Goldstone bosons. As the massive particles are non-relativistic they produce a line signature in the spectrum of Goldstone bosons at $k \approx m_\chi/2$ on top of the $1/k$ continuum. We have tested the sensitivity of our results to the initial velocity and the field profile and find that the results are qualitatively

unchanged as seen in Appendix A.2.

In contrast, studies of loop decay (Vilenkin and Vachaspati (1987); Battye and Shellard (1994b)) using the Kalb-Ramond description assume that there is negligible massive radiation and that radiation backreaction can be ignored. Then it is found that all the massless radiation is in the first few radiation harmonics. This is at odds with our results obtained by evolving the full field theory for loops that have length about 1000 times the width of the string. It is clear that radiation backreaction is very important for us, and we see a conversion of the kink collision energy into core oscillations that enhances massive radiation. Even if backreaction is included in the Kalb-Ramond approach, it does not allow for core oscillations and cannot account for the massive radiation. The caveat in the simple picture we have suggested is if our loops are large enough that the results can be extrapolated to vastly larger loops of cosmological interest.

Chapter 7

FINAL REMARKS

In previous chapters, I presented results from our publications (Saurabh and Vachaspati (2017, 2019a,b); Matsunami *et al.* (2019); Saurabh *et al.* (2020)). In these articles, we explored interactions of topological defects like magnetic monopoles and vortices/strings, which may have been produced in the early universe during phase transitions. Understanding these interactions is essential for predicting the observational signatures produced by these objects. For our investigations, we developed serial and parallel implementations of codes that solve relaxation and time evolution problems in $U(1)$ and $SU(2)$ gauge theories. These fortran programs used a parallelized implicit Crank-Nicolson method for evolution problems and our unique version of the fully parallelized Gauss-Seidel method for solving static equations of motion (relaxation). Also, for counting the number of loops produced in our simulations presented in Chapter 4, we developed an elegant program to track the strings using the winding number on each square plaquette of the lattice. We heavily used the high performance computing resources provided by Arizona State University (Agave) and The University of Texas at Austin (Stampede 2) to run these programs.

Using the relaxation code for finding monopole-antimonopole pair solutions, we looked for evidence verifying the existence of a sphaleron (unstable bound state) in the $SU(2)$ gauge theory. We computed the energy of a pair as a function of separation d and twist degree of freedom γ, which is related to the relative orientation of the monopole with respect to the antimonopole. For different values of the self-coupling for the scalar field, we found minima in the energy versus separation curves. These minima correspond to the bound state solution that we were looking for. A similar

analysis can be used to verify the existence of a sphaleron in the electroweak theory. Monopoles also play an important role in baryon number violating processes, which become highly likely at high temperatures, and their annihilation may contribute to the spectrum of high energy cosmic rays, making our investigations pertinent for understanding these phenomena.

All of our other studies involved time evolution of specific initial conditions in field theories with $U(1)$ gauge and global symmetries, devised for analyzing string loops in cosmological and condensed matter physics. In the early universe, networks of gauge and global strings may have been produced. Gauge strings have very high energy density in their cores and therefore couple strongly to gravitation. They naturally emit particle radiation as well. Our investigation of cosmic string loops showed that gravitational radiation is the dominant mode of energy loss for cosmological strings with the current upper bound on tension at $G\mu \approx 10^{-11}$ fixed by pulsar timing data. Experiments like LIGO are looking for gravitational wave signatures produced by such strings.

The mystery of cosmic dark matter has motivated a new particle, called the "axion", and axion models also contain a different variety of strings that are called "global cosmic strings". The dynamics of global cosmic strings is important for calculating the abundance of axion dark matter in today's universe. We again studied evolution of string loops and computed the spectra of radiation emitted. The massive particles radiated by the loops are mostly non-relativistic and eventually decay into Goldstone bosons (axions). Therefore, Goldstone bosons carry most of the energy lost by global strings and may contribute to the axion energy density in the universe after the QCD phase transition at which the axion acquires mass. Above the length scales associated with the mass of the scalar particles, we found a $1/k$ spectrum for the Goldstone radiation, which is different from what was predicted earlier using the zero-width

approximation for the strings.

All the loop decay studies we have done until now involved rectangular loops with four kinks/anti-kinks (the corners). The string networks in our universe are more complicated and may consist of string loops with more kinks/anti-kinks (that is, polygons of more than four sides). Therefore, we are also interested in the construction of initial conditions that would produce such loops, and then studying their evolution to solidify the results we presented in this dissertation.

In superconductors, which can be described using the Abelian Higgs model under certain conditions with bosonic Cooper pairs playing the role of the massive scalar particle, vortices are readily produced. We demonstrated that if we can produce wavepackets of these massive bosons inside the superconductor by some method of excitation like shining light onto it, vortex loops are produced. We used our string tracking code to verify this and count the number of loops produced. However, this loop production process appears to be excluded in certain regions of parameter space and hints at chaos like phenomena.

Abbasi, R. *et al.*, "Search for relativistic magnetic monopoles with icecube", Phys. Rev. D **87**, 022001, URL https://link.aps.org/doi/10.1103/PhysRevD.87.022001 (2013).

Abbott, B. *et al.*, "Constraints on cosmic strings using data from the first Advanced LIGO observing run", Phys. Rev. **D97**, 10, 102002 (2018).

Abrikosov, A., "The magnetic properties of superconducting alloys", Journal of Physics and Chemistry of Solids **2**, 3, 199 – 208, URL http://www.sciencedirect.com/science/article/pii/0022369757900835 (1957).

Acharya et al., B., "Search for magnetic monopoles with the moedal prototype trapping detector in 8 tev proton-proton collisions at the lhc", Journal of High Energy Physics **2016**, 8, 67, URL http://dx.doi.org/10.1007/JHEP08(2016)067 (2016).

Adrián-Martínez, S. *et al.*, "Search for relativistic magnetic monopoles with the {ANTARES} neutrino telescope", Astroparticle Physics **35**, 10, 634 – 640, URL http://www.sciencedirect.com/science/article/pii/S0927650512000461 (2012).

Albrecht, A. and N. Turok, "Evolution of cosmic strings", Phys. Rev. Lett. **54**, 1868–1871, URL https://link.aps.org/doi/10.1103/PhysRevLett.54.1868 (1985).

Allen, B. and E. P. S. Shellard, "Cosmic-string evolution: A numerical simulation", Phys. Rev. Lett. **64**, 119–122, URL https://link.aps.org/doi/10.1103/PhysRevLett.64.119 (1990a).

Allen, B. and E. P. S. Shellard, "Cosmic-string evolution: A numerical simulation", Phys. Rev. Lett. **64**, 119–122, URL https://link.aps.org/doi/10.1103/PhysRevLett.64.119 (1990b).

Atiyah, M. and N. Hitchin, "Low energy scattering of non-abelian monopoles", Physics Letters A **107**, 1, 21 – 25, URL http://www.sciencedirect.com/science/article/pii/0375960185902385 (1985).

Bates, L. and R. Montgomery, "Closed geodesics on the space of stable two-monopoles", Comm. Math. Phys. **118**, 4, 635–640, URL https://projecteuclid.org:443/euclid.cmp/1104162168 (1988).

Battye, R. A. and E. P. S. Shellard, "Axion string constraints", Phys. Rev. Lett. **73**, 2954–2957, [Erratum: Phys. Rev. Lett.76,2203(1996)] (1994a).

Battye, R. A. and E. P. S. Shellard, "Global string radiation", Nucl. Phys. **B423**, 260–304 (1994b).

Battye, R. A. and E. P. S. Shellard, "Axion string cosmology and its controversies", in "Beyond the desert: Accelerator, non-accelerator and space approaches into the next millennium. Proceedings, 2nd International Conference on particle physics beyond the standard model, Ringberg Castle, Tegernsee, Germany, June 6-12, 1999", pp. 565–572 (1999).

Baumgarte, T. W. and S. L. Shapiro, *Numerical Relativity: Solving Einstein's Equations on the Computer* (Cambridge University Press, New York, NY, USA, 2010).

Bennett, D. P. and F. m. c. R. Bouchet, "Evidence for a scaling solution in cosmic-string evolution", Phys. Rev. Lett. **60**, 257–260, URL `https://link.aps.org/doi/10.1103/PhysRevLett.60.257` (1988).

Bennett, D. P. and F. m. c. R. Bouchet, "High-resolution simulations of cosmic-string evolution. i. network evolution", Phys. Rev. D **41**, 2408–2433, URL `https://link.aps.org/doi/10.1103/PhysRevD.41.2408` (1990).

Bevis, N., M. Hindmarsh, M. Kunz and J. Urrestilla, "CMB power spectrum contribution from cosmic strings using field-evolution simulations of the Abelian Higgs model", Phys. Rev. **D75**, 065015 (2007).

Bhattacharjee, P. and G. Sigl, "Monopole annihilation and highest energy cosmic rays", Phys. Rev. **D51**, 4079–4091 (1995).

Binetruy, P., A. Bohe, T. Hertog and D. A. Steer, "Gravitational Wave Bursts from Cosmic Superstrings with Y-junctions", Phys. Rev. **D80**, 123510 (2009).

Blanco-Pillado, J. J., K. D. Olum and B. Shlaer, "Large parallel cosmic string simulations: New results on loop production", Phys. Rev. **D83**, 083514 (2011).

Blanco-Pillado, J. J., K. D. Olum and X. Siemens, "New limits on cosmic strings from gravitational wave observation", Phys. Lett. **B778**, 392–396 (2018a).

Blanco-Pillado, J. J., K. D. Olum and X. Siemens, "New limits on cosmic strings from gravitational wave observation", Physics Letters B **778**, 392 – 396, URL `http://www.sciencedirect.com/science/article/pii/S0370269318300583` (2018b).

Bogomolny, E. B., "Stability of Classical Solutions", Sov. J. Nucl. Phys. **24**, 449, [Yad. Fiz.24,861(1976)] (1976).

Brandenberger, R. H., "On the Decay of Cosmic String Loops", Nucl. Phys. **B293**, 812–828 (1987).

Cohen, A. G. and D. B. Kaplan, "The exact metric about global cosmic strings", Physics Letters B **215**, 1, 67 – 72, URL `http://www.sciencedirect.com/science/article/pii/0370269388910726` (1988).

Copeland, E., T. W. B. Kibble and D. Austin, "Scaling solutions in cosmic-string networks", Phys. Rev. D **45**, R1000–R1004, URL `https://link.aps.org/doi/10.1103/PhysRevD.45.R1000` (1992).

Copeland, E. J. and T. W. B. Kibble, "Cosmic Strings and Superstrings", Proc. Roy. Soc. Lond. **A466**, 623–657 (2010).

Copeland, E. J., L. Pogosian and T. Vachaspati, "Seeking String Theory in the Cosmos", Class. Quant. Grav. **28**, 204009 (2011).

Davis, R. L., "Goldstone bosons in string models of galaxy formation", Phys. Rev. D **32**, 3172–3177, URL `https://link.aps.org/doi/10.1103/PhysRevD.32.3172` (1985).

Davis, R. L., "Cosmic Axions from Cosmic Strings", Phys. Lett. **B180**, 225–230 (1986).

Davis, R. L. and E. P. S. Shellard, "DO AXIONS NEED INFLATION?", Nucl. Phys. **B324**, 167–186 (1989).

Dutta, S., D. A. Steer and T. Vachaspati, "Creating Kinks from Particles", Phys. Rev. Lett. **101**, 121601 (2008).

Fleury, L. and G. D. Moore, "Axion dark matter: strings and their cores", JCAP **1601**, 004 (2016).

Garfinkle, D. and T. Vachaspati, "Radiation from kinky, cuspless cosmic loops", Phys. Rev. D **36**, 2229–2241, URL `https://link.aps.org/doi/10.1103/PhysRevD.36.2229` (1987).

Gauge String Movie, URL `https://ayushsaurabh.home.blog` (2019).

Global String Movie, URL `https://ayushsaurabh.home.blog/2020/01/02/decay-of-cosmic-global-string-loops/` (2020).

Gorghetto, M., E. Hardy and G. Villadoro, "Axions from Strings: the Attractive Solution", JHEP **07**, 151 (2018).

Groisser, D., "SU(2) yang-mills-higgs theory on $\mathbb{R}^3$", Harvard University Ph.D. thesis. (1983).

Hagmann, C., S. Chang and P. Sikivie, "Axion radiation from strings", Phys. Rev. **D63**, 125018 (2001).

Hagmann, C. and P. Sikivie, "Computer simulations of the motion and decay of global strings", Nucl. Phys. **B363**, 247–280 (1991).

Harari, D. and P. Sikivie, "On the Evolution of Global Strings in the Early Universe", Phys. Lett. **B195**, 361–365 (1987).

Hindmarsh, M., J. Lizarraga, J. Urrestilla, D. Daverio and M. Kunz, "Scaling from gauge and scalar radiation in Abelian Higgs string networks", Phys. Rev. **D96**, 2, 023525 (2017).

Hindmarsh, M., J. Lizarraga, J. Urrestilla, D. Daverio and M. Kunz, "Type I Abelian Higgs strings: evolution and Cosmic Microwave Background constraints", Phys. Rev. **D99**, 8, 083522 (2019).

Hindmarsh, M. and A. Rajantie, "Defect formation and local gauge invariance", Phys. Rev. Lett. **85**, 4660–4663, URL https://link.aps.org/doi/10.1103/PhysRevLett.85.4660 (2000a).

Hindmarsh, M. and A. Rajantie, "Defect formation and local gauge invariance", Phys. Rev. Lett. **85**, 4660–4663 (2000b).

Hindmarsh, M., C. Ringeval and T. Suyama, "The CMB temperature bispectrum induced by cosmic strings", Phys. Rev. **D80**, 083501 (2009a).

Hindmarsh, M., S. Stuckey and N. Bevis, "Abelian Higgs Cosmic Strings: Small Scale Structure and Loops", Phys. Rev. **D79**, 123504 (2009b).

Hiramatsu, T., M. Kawasaki, T. Sekiguchi, M. Yamaguchi and J. Yokoyama, "Improved estimation of radiated axions from cosmological axionic strings", Phys. Rev. **D83**, 123531 (2011).

Kalb, M. and P. Ramond, "Classical direct interstring action", Phys. Rev. **D9**, 2273–2284 (1974).

Kennes, D. M. and A. J. Millis, "Electromagnetic response during quench dynamics to the superconducting state: Time-dependent ginzburg-landau analysis", Phys. Rev. B **96**, 064507, URL https://link.aps.org/doi/10.1103/PhysRevB.96.064507 (2017).

Kibble, T. W. B., "Topology of cosmic domains and strings", Journal of Physics A: Mathematical and General **9**, 8, 1387–1398, URL https://doi.org/10.1088%2F0305-4470%2F9%2F8%2F029 (1976).

Klaer, V. B. and G. D. Moore, "The dark-matter axion mass", JCAP **1711**, 11, 049 (2017).

Klaer, V. B. and G. D. Moore, "Global cosmic string networks as a function of tension", (2019).

Kleihaus, B. and J. Kunz, "A Monopole - anti-monopole solution of the SU(2) Yang-Mills-Higgs model", Phys. Rev. **D61**, 025003 (2000).

Klinkhamer, F. R. and N. S. Manton, "A saddle-point solution in the weinberg-salam theory", Phys. Rev. D **30**, 2212–2220, URL https://link.aps.org/doi/10.1103/PhysRevD.30.2212 (1984).

Lasky, P. D. *et al.*, "Gravitational-wave cosmology across 29 decades in frequency", Phys. Rev. **X6**, 1, 011035 (2016).

Lizarraga, J., J. Urrestilla, D. Daverio, M. Hindmarsh and M. Kunz, "New CMB constraints for Abelian Higgs cosmic strings", JCAP **1610**, 10, 042 (2016).

Lopez-Eiguren, A., J. Lizarraga, M. Hindmarsh and J. Urrestilla, "Cosmic Microwave Background constraints for global strings and global monopoles", JCAP **1707**, 026 (2017).

Lorenz, L., C. Ringeval and M. Sakellariadou, "Cosmic string loop distribution on all length scales and at any redshift", JCAP **1010**, 003 (2010).

Manton, N., "A remark on the scattering of bps monopoles", Physics Letters B **110**, 1, 54 – 56, URL http://www.sciencedirect.com/science/article/pii/0370269382909509 (1982a).

Manton, N., "A remark on the scattering of bps monopoles", Physics Letters B **110**, 1, 54 – 56, URL http://www.sciencedirect.com/science/article/pii/0370269382909509 (1982b).

Manton, N. and P. Sutcliffe, *Topological Solitons*, Cambridge Monographs on Mathematical Physics (Cambridge University Press, 2004), URL https://books.google.com/books?id=e2tPhFdSUf8C.

Manton, N. S., "Topology in the weinberg-salam theory", Phys. Rev. D **28**, 2019–2026, URL https://link.aps.org/doi/10.1103/PhysRevD.28.2019 (1983).

Martins, C. J. A. P., J. N. Moore and E. P. S. Shellard, "A Unified model for vortex string network evolution", Phys. Rev. Lett. **92**, 251601 (2004).

Matsunami, D., L. Pogosian, A. Saurabh and T. Vachaspati, "Decay of Cosmic String Loops Due to Particle Radiation", Phys. Rev. Lett. **122**, 20, 201301 (2019).

Matzner, R. A., "Interaction of u(1) cosmic strings: Numerical intercommutation", Computers in Physics **2**, 5, 51–64, URL https://aip.scitation.org/doi/abs/10.1063/1.168306 (1988).

Moriarty, K., E. Myers and C. Rebbi, "Dynamical interactions of cosmic strings and flux vortices in superconductors", Physics Letters B **207**, 4, 411 – 418, URL http://www.sciencedirect.com/science/article/pii/0370269388906740 (1988).

Myers, E., C. Rebbi and R. Strilka, "Study of the interaction and scattering of vortices in the abelian higgs (or ginzburg-landau) model", Phys. Rev. D **45**, 1355–1364, URL https://link.aps.org/doi/10.1103/PhysRevD.45.1355 (1992).

Nahm, W., "The interaction energy of 't hooft monopoles in the prasad-sommerfield limit", Physics Letters B **79**, 4, 426 – 428, URL http://www.sciencedirect.com/science/article/pii/0370269378903982 (1978).

Nambu, Y., "String-like configurations in the weinberg-salam theory", Nuclear Physics B **130**, 3, 505 – 515, URL http://www.sciencedirect.com/science/article/pii/0550321377902528 (1977).

Nielsen, H. B. and P. Olesen, "Vortex Line Models for Dual Strings", Nucl. Phys. **B61**, 45–61, [,302(1973)] (1973).

Olum, K. D. and J. J. Blanco-Pillado, "Field theory simulation of Abelian Higgs cosmic string cusps", Phys. Rev. **D60**, 023503 (1999).

Olum, K. D. and J. J. Blanco-Pillado, "Radiation from cosmic string standing waves", Phys. Rev. Lett. **84**, 4288–4291 (2000).

Pogosian, L. and T. Vachaspati, "Relaxing the geodesic rule in defect formation algorithms", Physics Letters B **423**, 1, 45 – 48, URL http://www.sciencedirect.com/science/article/pii/S0370269398001099 (1998).

Polyakov, A. M., "Particle Spectrum in the Quantum Field Theory", JETP Lett. **20**, 194–195, [Pisma Zh. Eksp. Teor. Fiz.20,430(1974)] (1974).

Prasad, M. K. and C. M. Sommerfield, "An Exact Classical Solution for the 't Hooft Monopole and the Julia-Zee Dyon", Phys. Rev. Lett. **35**, 760–762 (1975).

Preskill, J. P., "Cosmological production of superheavy magnetic monopoles", Phys. Rev. Lett. **43**, 1365–1368, URL http://link.aps.org/doi/10.1103/PhysRevLett.43.1365 (1979).

Romanczukiewicz, T. and Ya. Shnir, "Oscillon resonances and creation of kinks in particle collisions", Phys. Rev. Lett. **105**, 081601 (2010).

Ruback, P., "Vortex string motion in the abelian higgs model", Nuclear Physics B **296**, 3, 669 – 678, URL http://www.sciencedirect.com/science/article/pii/0550321388900387 (1988).

Saurabh, A. and T. Vachaspati, "Monopole-antimonopole Interaction Potential", Phys. Rev. **D96**, 10, 103536 (2017).

Saurabh, A. and T. Vachaspati, "Monopole-antimonopole: interaction, scattering and creation", in "Topological avatars of new physics London, United Kingdom, March 4-5, 2019", (2019a).

Saurabh, A. and T. Vachaspati, "String Production in the Abelian Higgs Vacuum", Phys. Rev. **D99**, 10, 103509 (2019b).

Saurabh, A., T. Vachaspati and L. Pogosian, "Decay of cosmic global string loops", Phys. Rev. D **101**, 083522, URL https://link.aps.org/doi/10.1103/PhysRevD.101.083522 (2020).

Shellard, E. and P. Ruback, "Vortex scattering in two dimensions", Physics Letters B **209**, 2, 262 – 270, URL http://www.sciencedirect.com/science/article/pii/0370269388909446 (1988).

Srednicki, M. and S. Theisen, "Nongravitational Decay of Cosmic Strings", Phys. Lett. **B189**, 397 (1987).

Taubes, C. H., "The existence of a non-minimal solution to the su (2) yang-mills-higgs equations on $\mathbb{R}^3$: Part i", Communications in Mathematical Physics **86**, 2, 257–298, URL http://dx.doi.org/10.1007/BF01206014 (1982a).

Taubes, C. H., "The existence of a non-minimal solution to the su(2) yang-mills-higgs equations on $\mathbb{R}^3$: Part ii", Communications in Mathematical Physics **86**, 3, 299–320, URL http://dx.doi.org/10.1007/BF01212170 (1982b).

Teukolsky, S. A., "On the stability of the iterated Crank-Nicholson method in numerical relativity", Phys. Rev. **D61**, 087501 (2000).

't Hooft, G., "Magnetic monopoles in unified gauge theories", Nuclear Physics B **79**, 2, 276 – 284, URL http://www.sciencedirect.com/science/article/pii/0550321374904866 (1974).

Tinkham, M., *Introduction to Superconductivity* (Dover Publications, 2004), 2 edn., URL http://www.worldcat.org/isbn/0486435032.

Vachaspati, T., "Creation of magnetic monopoles in classical scattering", Phys. Rev. Lett. **117**, 181601, URL https://link.aps.org/doi/10.1103/PhysRevLett.117.181601 (2016a).

Vachaspati, T., "Creation of Magnetic Monopoles in Classical Scattering", Phys. Rev. Lett. **117**, 18, 181601 (2016b).

Vachaspati, T., "Monopole-antimonopole scattering", Phys. Rev. D **93**, 045008, URL http://link.aps.org/doi/10.1103/PhysRevD.93.045008 (2016c).

Vachaspati, T., A. E. Everett and A. Vilenkin, "Radiation From Vacuum Strings and Domain Walls", Phys. Rev. **D30**, 2046 (1984).

Vachaspati, T. and A. Vilenkin, "Formation and evolution of cosmic strings", Phys. Rev. D **30**, 2036–2045, URL https://link.aps.org/doi/10.1103/PhysRevD.30.2036 (1984).

Vachaspati, T. and A. Vilenkin, "Gravitational radiation from cosmic strings", Phys. Rev. D **31**, 3052–3058, URL https://link.aps.org/doi/10.1103/PhysRevD.31.3052 (1985).

Vilenkin, A. and A. E. Everett, "Cosmic strings and domain walls in models with goldstone and pseudo-goldstone bosons", Phys. Rev. Lett. **48**, 1867–1870, URL https://link.aps.org/doi/10.1103/PhysRevLett.48.1867 (1982).

Vilenkin, A. and E. P. S. Shellard, *Cosmic Strings and Other Topological Defects* (Cambridge University Press, 2000), URL http://www.cambridge.org/mw/academic/subjects/physics/theoretical-physics-and-mathematical-physics/cosmic-strings-and-other-topological-defects?format=PB.

Vilenkin, A. and T. Vachaspati, "Radiation of Goldstone Bosons From Cosmic Strings", Phys. Rev. **D35**, 1138 (1987).

Yamaguchi, M., M. Kawasaki and J. Yokoyama, "Evolution of axionic strings and spectrum of axions radiated from them", Phys. Rev. Lett. **82**, 4578–4581 (1999).

Zeldovich, Y. B., "Cosmological fluctuations produced near a singularity", Monthly Notices of the Royal Astronomical Society **192**, 4, 663–667, URL https://doi.org/10.1093/mnras/192.4.663 (1980).

Zurek, W., "Cosmological Experiments in Superfluid Helium?", Nature **317**, 505–508 (1985).

Zurek, W., "Cosmological experiments in condensed matter systems", Physics Reports **276**, 4, 177 – 221, URL http://www.sciencedirect.com/science/article/pii/S0370157396000099 (1996).

APPENDIX A

INITIAL CONDITIONS FOR GLOBAL STRING SIMULATIONS

A.1 Implementing Periodic Boundary Conditions

The ansatz in Equations (6.10) and (6.11) does not satisfy periodic boundary conditions and requires further adjustments. This is done in several steps that we now outline. The basic idea is to first ensure that a parallel string-antistring pair satisfies periodic boundary conditions and then to patch together the vertical and horizontal pairs by using the product ansatz.

We set the phase of the field and time derivatives of the field to zero at the boundaries of the planes orthogonal to each string-antistring pair. For example, for the pair along z direction, we have the field

$$\begin{aligned}\phi_{s\bar{s},z} &= \frac{\phi_{s,z}\phi_{\bar{s},z}}{\eta} = \frac{|\phi_{s,z}||\phi_{\bar{s},z}|}{\eta} e^{i(\theta_{s,z}-\theta_{\bar{s},z})} \\ &= \phi_{s\bar{s},z1} + i\phi_{s\bar{s},z2}\,.\end{aligned} \tag{A.1}$$

We now multiply the imaginary part of the field above with the function

$$f_z = (1-\frac{x^2}{L^2})(1-\frac{y^2}{L^2})\,, \tag{A.2}$$

where $2L$ is the size of the numerical domain. This forces the phase of the field to vanish at the boundaries but also alters the magnitude of the field. We then normalize the field so that the magnitude is reset to its original value on the boundaries,

$$\phi^{(1)}_{s\bar{s},z1} = \sqrt{\frac{\phi^2_{s\bar{s},z1}+\phi^2_{s\bar{s},z2}}{\phi^2_{s\bar{s},z1}+\phi^2_{s\bar{s},z2}\ f_z^2}}\ \phi_{s\bar{s},z1}\,, \tag{A.3}$$

$$\phi^{(1)}_{s\bar{s},z2} = \sqrt{\frac{\phi^2_{s\bar{s},z1}+\phi^2_{s\bar{s},z2}}{\phi^2_{s\bar{s},z1}+\phi^2_{s\bar{s},z2}\ f_z^2}}\ \phi_{s\bar{s},z2}\ f_z\,. \tag{A.4}$$

$$\tag{A.5}$$

Note that the locations of the strings do not change by the above manipulations because the zeros of the field are unaffected.

The time derivatives can now be set to zero at the boundaries by simply multiplying the derivatives with the function f_z, that is,

$$\dot{\phi}^{(1)}_{s\bar{s},z} = \partial_t \phi^{(1)}_{s\bar{s},z} f_z\,. \tag{A.6}$$

At this stage the field denoted by $\phi^{(1)}_{s\bar{s},z}$ has zero phase on the boundaries but its magnitude still varies and does not satisfy periodic boundary conditions. In a cosmological setting the field magnitude will be η (=1) far from the strings. Hence we force the magnitude to be η on the boundaries of the lattice. To achieve this, we successively divide the field $\phi^{(1)}_{s\bar{s},z}$ by functions that interpolate between boundary values along orthogonal directions. The first interpolating functions is defined as

$$I_{zx} = \frac{|\phi^{(1)}_{s\bar{s},z}|_{x=L} - |\phi^{(1)}_{s\bar{s},z}|_{x=-L}}{2L}(x+L) + |\phi^{(1)}_{s\bar{s},z}|_{x=-L}\,, \tag{A.7}$$

which gives us a new field periodic in the x direction,

$$\phi^{(2)}_{s\bar{s},z} = \frac{\phi^{(1)}_{s\bar{s},z}}{I_{zx}} \,. \tag{A.8}$$

Then we divide by a corresponding interpolation function in the y direction,

$$I_{zy} = \frac{|\phi^{(2)}_{s\bar{s},z}|_{y=L} - |\phi^{(2)}_{s\bar{s},z}|_{y=-L}}{2L}(y+L) + |\phi^{(2)}_{s\bar{s},z}|_{y=-L} \,, \tag{A.9}$$

to get a field that satisfies periodic boundary conditions in both x and y directions,

$$\phi^{P}_{s\bar{s},z} = \frac{\phi^{(2)}_{s\bar{s},z}}{I_{zy}} \,. \tag{A.10}$$

The steps above ensure that the complex scalar field and its time derivatives are periodic along each direction for both string-antistring pairs. As a final step, we construct the field and its time derivative using the product ansatz as follows,

$$\phi = \frac{\phi^{P}_{s\bar{s},z}\phi^{P}_{s\bar{s},x}}{\eta} \,, \tag{A.11}$$

$$\dot{\phi} = \frac{\dot{\phi}^{P}_{s\bar{s},z}\phi^{P}_{s\bar{s},x} + \phi^{P}_{s\bar{s},z}\dot{\phi}^{P}_{s\bar{s},x}}{\eta} \,. \tag{A.12}$$

Now ϕ and $\dot{\phi}$ satisfy periodic boundary conditions and can be used as initial conditions in our simulations.

A.2 Universality Tests

Here we describe the results when we change the way we prepare the initial conditions.

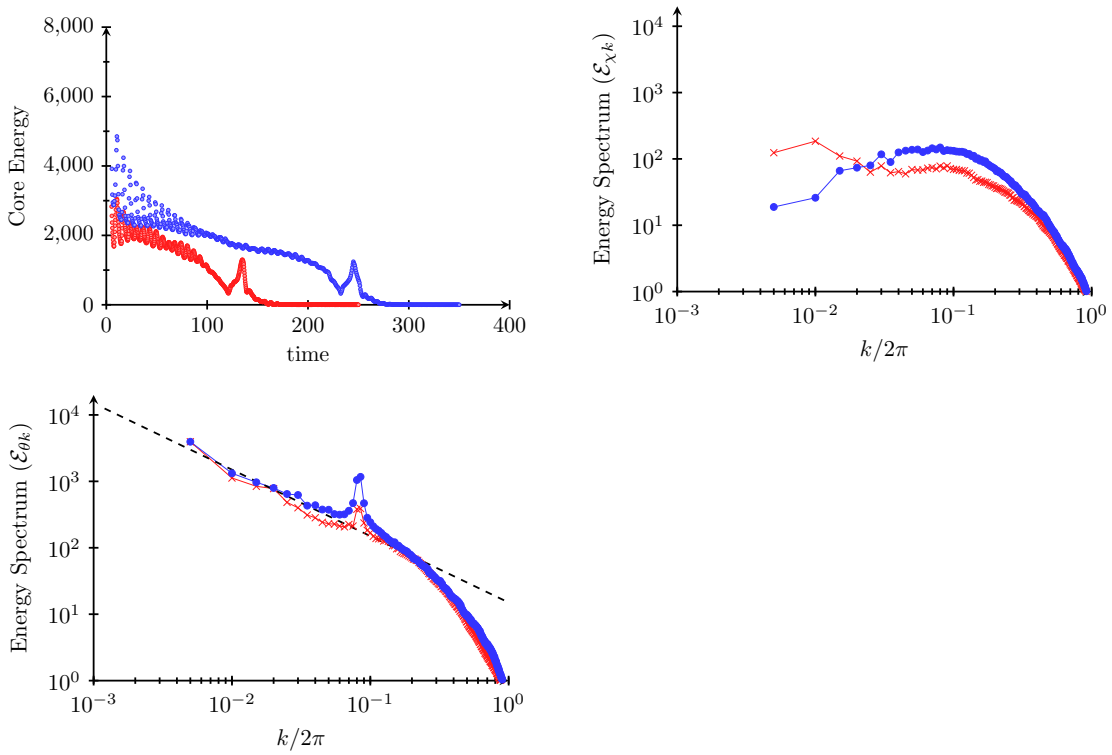

Figure A.1: Plots comparing core energy and spectra for loops of size 100 with initial strings moving at velocities $v = 0.6$ (red) and $v = 0.8$ (blue).

First we change the initial velocity of the straight strings from 0.6 to 0.8. The results for the energy decay and the spectrum with initial velocity are shown in Figs. A.1. Some of the numerical values change as expected, but the qualitative features are unchanged.

To test the sensitivity of our results to how we prepare the initial conditions, we have run the simulation with the function f_z in Eq. (A.2) replaced by f_z^2, since f_z^2 also has the property that it vanishes on the boundaries and is 1 at the origin. The results for the energy decay and the spectrum are shown in Figs. A.2. As before, the qualitative features are same in both cases with slight differences in the numerical values.

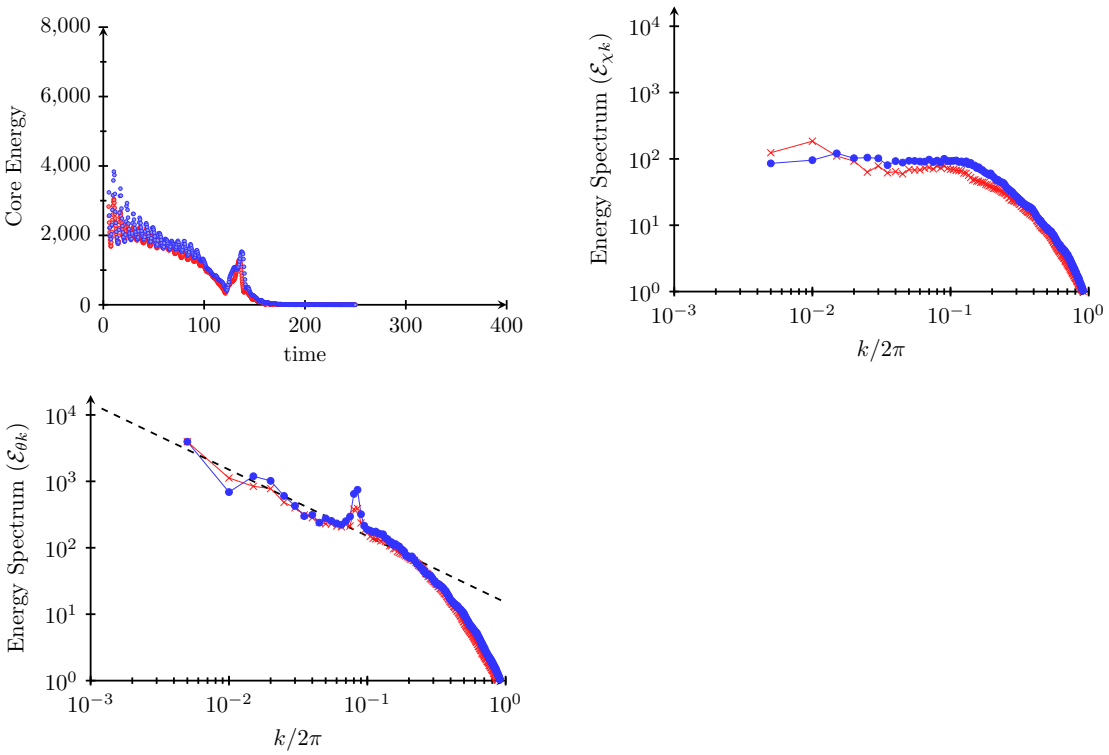

Figure A.2: Plots comparing core energy and spectra for loops of size 100 with functions f_z (red) and f_z^2 (blue) used to fix periodic boundary conditions.

APPENDIX B

CONVENTIONS

In this appendix, I present the conventions used throughout this dissertation.

1. I set the reduced Planck's constant $\hbar = 1$, the speed of light $c = 1$, and Boltzmann's constant $k_B = 1$ in all our calculations. This results in all physical quantities being expressed in mass dimensions:

$$[Mass] = [Energy] = [Momentum] = [Temperature] = [Frequency]\,,$$

$$[Time] = [Length] = [Mass^{-1}]\,.$$

2. Greek letter indices $\mu, \nu, \ldots$ run over spacetime labels from 0 to d-1, where d is the dimensionality of the spacetime,

$$x^\mu = \{t, x, y, z\}\,, \tag{B.1}$$

$$\partial_\mu = \{\partial_t, \partial_x, \partial_y, \partial_z\}\,. \tag{B.2}$$

3. I use the mostly minuses metric signature, that is, $(+, -, -, -)$.

4. Einstein summation convention is used, that is,

$$x^2 = x_\mu x^\mu = g_{\mu\nu} x^\mu x^\nu = t^2 - x^2 - y^2 - z^2\,. \tag{B.3}$$